Ben Gurion University of the Negev
Faculty of Natural Sciences

Department of Physics

Subject: Magnetic simulations for trapping and cooling neutral atoms

Thesis submitted in partial fulfillment of the requirements for the degree of Master of Science in the Faculty of Natural Sciences

By Eyal Fleminger

27/12/2006

Subject: Magnetic simulations for trapping and cooling neutral atoms

Thesis in partial fulfillment of the requirements for the degree of Master in Science

In the Faculty of Natural Sciences

By: Eyal Fleminger

Advisor: Dr. Ron Folman

Department of Physics

Faculty of Natural Sciences

Ben Gurion University of the Negev

Author's Signature: _____ Date: _____

Advisor's Signature: _____ Date: _____

Signature of the chairman of the departmental committee: _____ Date: _____

Magnetic simulations for trapping and cooling neutral atoms

Submitted to the Faculty of Natural Sciences of Ben Gurion University of the Negev in partial fulfillment of the requirements for the degree of Master in Science by Eyal Fleminger in 2006

Abstract

The interactions of neutral atom ensembles with resonant light, magnetic fields, or a combination thereof can be used to trap the ensembles and bring them to ultracold temperatures, and many experiments have been developed to do so. We have made a theoretical study of several configurations of *miniaturized* traps, thereby facilitating experiments with ultracold atoms on an "atom chip" wherein the confining magnetic fields are generated by microcircuits on a semiconductor chip. This thesis describes the basic principles and the details of specific methods for magnetic and magneto-optical trapping, and discusses techniques to simulate such traps. It also describes the development and construction of miniaturized magnetic traps currently being used experimentally in our atom chip laboratory. In addition, several new designs will be described and discussed.

"Think where man's glory most begins and ends
And say my glory was I had such friends"
W. B. Yeats

Acknowledgements

This work could not have been completed without the aid of many people:

First and foremost, the members of the Atom Chip group at Ben Gurion University, including my advisor Dr. Ron Folman, Dr. Mark Keil, Dr. Yoni Japha, Dr. David Groswasser, Tal David, Ran Salem (both of whom performed the experimental measurements on the mount described here), Shimi Machluf, Dr. Plamen Petrov, and the rest of the group.

I would also like to thank Aharon Tabibian and the rest of the staff of BGU's Faculty of Natural Science's machine shop for their extensive support in the fabrication of the mount described herein.

Finally I would like to thank my father, Prof. Gideon Fleminger, as well as Madelon Ruth Fleminger for their assistance in proofreading and editing this work, and the rest of my family and friends (you know who you are) for their support throughout this period.

Table of Figures

1 Introduction

1.1 Background

The field of cooling and trapping of neutral atom ensembles – the subject of the 1997 Nobel Prize for physics – has undergone rapid development since the 1980s. When bosons are cooled to ultralow (micro-Kelvin) temperatures, their de Broglie wavelengths increase to such a degree that they begin to overlap (that is, the distance between the atoms becomes smaller than the de Broglie wavelength). At the very lowest temperatures, the majority of the atoms in the ensemble occupy the ground state, so they can all be described by a single macroscopic wavefunction. First predicted by Einstein in 1924 (based on work by Bose), this phenomenon is known as Bose-Einstein condensation (BEC), and is currently the focus of intensive research. However, achieving BEC is quite challenging – indeed, it took seven decades since the theory was proposed for it to become a reality.

The fundamental characteristic of a BEC is the coherence of all its atoms. This coherence is lost, however, if the atoms interact strongly with external fields or particles. Therefore, ultracold neutral atoms, which have relatively weak interactions with each other and with electromagnetic fields, are promising candidates for applications involving the coherent manipulation of matter. The advent of the magneto-optical trap (MOT) in 1987 [1] was a major step forward, as it allows robust cooling to ultralow temperatures. The combination of MO and purely magnetic trapping, along with the novel technique of evaporative cooling, allowed the first experimental realizations of a BEC (for which the 2001 Nobel Prize in physics was awarded) less than a decade later [2, 3].

There are a variety of techniques for generating MOTs and pure magnetic traps. In particular, there is much recent research based on using integrated circuitry microchips for the purpose of creating magnetic microtraps, with which atom ensembles can be manipulated near the chip surface. Such chips are known as "atom chips" [4] and are being utilized in a wide variety of unique experiments.

The atom chip must be placed near the center of the required external optical and magnetic fields, and it must operate under ultra-high vacuum (UHV) conditions. One method to correctly place the chip is known as a "chip mount", such as that described in [5], and implemented experimentally in [6-10].

1.2 Goals

Given the various components and materials needed, constructing a chip mount can be quite expensive, both financially and in terms of time. It is very important to have simulations which can accurately predict the form and parameters of the trap, and how to use it most effectively for atom chip experiments.

In this thesis, I develop and discuss the mathematical relationships and properties which affect various parameters of the magnetic traps in use. Considerations affecting the experimental realization of these traps are discussed, as are the principles of the simulations used in the design process.

Specifically, I describe the design and construction of a mount (designated as Mount 1 in our lab) intended to hold an atom chip and to generate a MOT as well as a purely magnetic trap. This mount has been used to create ultracold atom ensembles of rubidium 87 (^{87}Rb) in our lab. Ultimately, my intent is to improve the mount described in [5] and its ability to create Bose-Einstein condensates which can be used for subsequent experiments utilizing the wires etched on the chip. Various modifications have been made to optimize the traps' parameters and flexibility, as well as to allow easier construction. In addition, I use the simulations to describe and analyze several new designs under consideration for future systems.

1.3 Outline

Chapter 2 describes the basic principles of magnetic, optical, and magneto-optical trapping. The parameters and effects of particular trapping schemes are discussed. The mathematical relationships between the various trap parameters – such as currents, bias fields, trap height, trap frequencies, etc. – for several different types of traps are developed and discussed in some detail.

Chapter 3 discusses the practical realization of a MOT in the laboratory. Some important considerations which affect the trap design are described, in order to serve as a guide for the development and design of wire traps. This is followed by a brief description of the experimental setup and by some of the initial results obtained with Mount 1.

Chapter 4 discusses the simulation software itself. It describes the techniques and the principles of the programs used, as well as some of their limitations.

Finally, Chapter 5 presents results for several alternative trap configurations, which are now incorporated in current experiments in order to improve the performance of the first system (Mount 1).

2 Theoretical principles of magnetic, optical, and magneto-optical trapping

The core of our experiments involves the trapping of neutral atoms by means of magnetic and optical fields, and using these forces to cool them. In this chapter, I describe several methods of trapping and cooling neutral atoms by means of these fields. This discussion generally follows [11, 12], though some parts – in particular, those related to magnetic trapping and to specific trap configurations – have been developed here in greater detail.

2.1 Magnetic trapping

One method of trapping atoms involves the use of magnetic fields. The interaction energy (the Zeeman energy) of an atom with a magnetic field is

$$E_B = -\vec{\mu} \cdot \vec{B} \tag{2.1.1}$$

where $\vec{\mu}$ is the magnetic moment of the atom, such that

$$\vec{\mu} = g_F \cdot \mu_B \cdot \vec{F} \tag{2.1.2}$$

where g_F is the Landé factor of the atomic hyperfine state, $\vec{F}$ is the total spin of the atom, and μ_B is the Bohr magneton. The frequency of the Larmor precession of the atom is given by

$$\omega_L = \frac{\mu_B \cdot \left|\vec{B}\right|}{\hbar} \tag{2.1.3}$$

If the field is inhomogeneous, the direction and strength of the field experienced by a moving atom varies spatially (and temporally, if the field is not static). Consequently, the motion of the atom induced by the magnetic force is quite complex, as are the dynamics of its spin states. However, if the Larmor precession is sufficiently fast compared to the rate of change of the magnetic field direction (i.e. ω_L is sufficiently large), an adiabatic approximation can be utilized [13]. In this approximation, the magnetic moment follows the field direction adiabatically, and the magnetic quantum number m_F is a constant of motion [14]

$$m_F = \frac{\vec{F} \cdot \vec{B}}{\left|\vec{B}\right|} \tag{2.1.4}$$

Combining (2.1.4) with (2.1.1) and (2.1.2) results in a potential U_{BI} (the potential due to the magnetic field, excluding other factors such as gravity) which is proportional to the absolute field magnitude, and is given by[1] [6, 15]

$$U_{BI} = E_B \cong g_F \cdot \mu_B \cdot m_F \cdot \left|\vec{B}\right| = \mu \left|\vec{B}\right| \qquad (2.1.5)$$

where

$$\mu \equiv g_F \cdot \mu_B \cdot m_F$$

The projection of the magnetic moment relative to the static magnetic field causes two possible states. If both the magnetic moment and the field are pointing (mostly) in the same direction (or in the opposite direction, depending on the sign of the Landé factor), $U_{BI}<0$, and the force drives the atom towards regions of higher field. This state is known as a strong-field (or a high-field) seeking state. In this state, the minima of U_{BI} exist at the maxima of the magnetic field. However, according to a generalization of the Earnshaw theorem [16, 17], maxima of the field cannot exist in current-free space. Thus, in order to trap strong-field seekers, the field source would have to be at the potential minimum [18].

On the other hand, if the directions of the magnetic moment and the field are opposite (or the same, depending on the sign of the Landé factor), then $U_{BI}>0$, and the resulting force causes the atoms to be attracted to the minima of the field (which are at the same locations as the potential minima). This state is known as a weak-field (or low-field) seeking state. Unlike in the previous case, the field sources may be external to the trapping region, and thus this state is the one more commonly used for magnetic trapping. There are various methods of doing so; several are described below.

2.1.1 Quadrupole trap

Perhaps the simplest type of trap is the quadrupole trap. Such a field can be generated by the use of two identical loops or coils through which counterpropagating currents of identical magnitude are running, as shown in Figure 1.

[1] The sign of g_F and hence the sign in equation (2.1.5) may vary in differing sources, depending on the sign convention used. We use the convention such that g_F for the $|F=2,m_F=2>$ ground state is ½ and thus it is a low-field-seeking state.

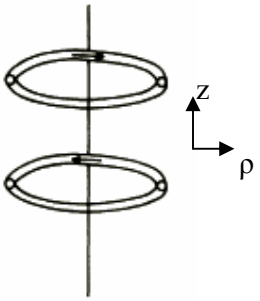

Figure 1 – Schematic of a quadrupole magnetic trap [19]

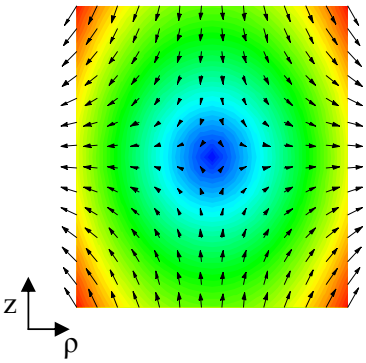

Figure 2 – Magnetic field generated by the trap in Figure 1 (reds indicate stronger field magnitudes)

In cylindrical coordinates[2], the magnetic field magnitude (Figure 2) of the trap is proportional to the coordinates [19]

$$\left|\vec{B}\right| \propto \sqrt{\rho^2 + 4z^2} \tag{2.1.6}$$

The field is zero at the center of the trap, and it will therefore trap low-field seekers.

The field above is an ideal quadrupole field. However, the designation "quadrupole field" is used in a general sense to classify magnetic traps which have a zero-field minimum. These traps tend to have very high field gradients, a desirable trait in a trap. However, they also have a significant drawback, as follows: an atom moving in the trap experiences a time-dependent magnetic field. As noted above, the adiabatic approximation is valid only so long as the rate of the field variation is much smaller than the Larmor precession frequency. According to equation (2.1.3), ω_L=0 where the field is zero. At that point, atoms can make transitions between magnetic states since these states are degenerate for zero field. Should the magnetic sublevel of a low-field seeker undergo a sign reversal (a "spin flip") as a result, it will become a high-field seeker and will be expelled from the trap. Such spin flips are known as Majorana transitions [13].

The loss rate from such a trap can be estimated. An atom of mass m and velocity v will undergo an adiabatic spin flip if v/r (r indicating, in this case, the atom's distance from the trap center) is larger than ω_L. If the atom passes within a distance r of the center of the trap, equation (2.1.3) can be rewritten as [20]

$$\omega_L \sim \frac{\mu \cdot r \cdot B_\rho'}{\hbar} \tag{2.1.7}$$

where

$$B_\rho' \equiv \frac{\partial B_\rho}{\partial \rho} \tag{2.1.8}$$

is the radial field gradient. Therefore, losses occur within an ellipsoid of radius

[2] Where z=0 is the midpoint between the loops; the θ co-ordinate is not shown since this system is axially symmetric.

$$r_0 \sim \sqrt{\frac{v\hbar}{\mu B'_\rho}} \tag{2.1.9}$$

The loss rate is determined by the flux of atoms through the ellipsoid and is

$$\frac{1}{\tau_0} = \frac{N \cdot r_0^2 \cdot v}{l_c^3} \tag{2.1.10}$$

where N is the number of atoms in the cloud and l_c is the cloud's radius. The viral theorem relates mean velocity to cloud size by [20]

$$m\bar{v}^2 \sim \mu \cdot l_c \cdot B'_\rho \tag{2.1.11}$$

By combining equations (2.1.9), (2.1.10), and (2.1.11), we get a loss rate of

$$\frac{1}{\tau_0} \sim \frac{\hbar N}{m \cdot l_c^2} \tag{2.1.12}$$

In a trap for low-field-seeking atoms, l_c increases with the temperature. Therefore, the loss rate increases as temperature decreases, since the atoms are clustered more densely around the trap minimum at lower temperatures and thus more atoms pass through the "hole". Therefore, while the loss rate is tolerable for relatively high-temperature traps such as MOTs, it prevents trapping at lower temperatures, such as those required for evaporative cooling (which is not discussed here; see [21] for more details).

There are various approaches for overcoming this problem. One of them is to generate a field with a temporally-varying minimum location. One such trap is a time-averaged orbital potential (TOP) trap[20]. In such a trap, the location of the field zero is constantly changing (orbiting around a fixed center, hence the name) at a frequency smaller than ω_L (thus permitting retention of the adiabatic approximation of equation (2.1.5)), but larger than the atoms' oscillation frequency [22]; thus, the location of the zero changes faster than the atoms can respond, preventing their escape from the trap.

A second approach involves taking advantage of repulsive optical forces [23, 24]. A blue-detuned laser beam[3] is used to repel the atoms from the location of the trap minimum. This effectively shifts the location of the trap minimum away from the magnetic field minimum, moving the atoms away from the "hole".

[3] A laser that is detuned towards frequencies higher than the resonance frequency.

2.1.2 The Ioffe-Pritchard trap

Another common approach for avoiding trap loss due to Majorana transitions is the use of a magnetic field with a *nonzero* minimum. One such trap configuration is the Ioffe-Pritchard trap [19], shown in Figure 3 (this configuration was proposed by Pritchard [25] based on the Ioffe magnetic bottle used for plasma confinement [26]).

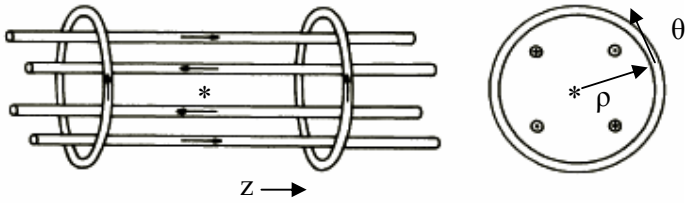

Figure 3 – Schematic of the Ioffe-Pritchard trap from the side (left) and the front (right). The z-axis is parallel to the four rods and ρ indicates the distance from this axis outwards from the center. The star denotes the origin of the co-ordinate system, mid-way between the coils. [19]

The four evenly spaced rods create, when the direction of current propagation alternates in adjacent rods, a quadrupole field identical to that shown in Figure 2 (in this case, however, the field as seen in Figure 2 is in the plane *parallel* to the coils in Figure 3, rather than perpendicular as in the previous case). The four rods produce a "tube" of zero field along the ρ=0 central axis (similar to the side guide; see section 2.1.3) but the $\hat{z}$ field component is zero everywhere, so the rods by themselves do not form a trap.

The two coils are similar to those used for the quadrupole trap in Figure 1, except that the currents are propagating in the *same* direction, and generate a field as shown in Figure 4.

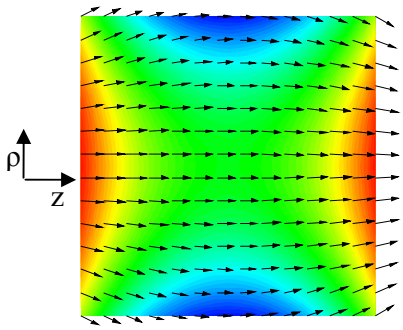

Figure 4 – Field of the two coils in Figure 3. The center of the plot (z=ρ=0) is at the center of the trap. Blue indicates low field while red indicates high field. The value of θ is irrelevant since the field produced by the two coils is axially symmetric.

We now consider the field produced by the rods and the coils acting together. This field is shown in Figure 5. The field from the coils is homogenous near the origin. Since the direction of the field from the four rods is the same as that from the coils everywhere between the rods and coils, the sum of these two fields has no zeroes within that volume, and thus the

Majorana losses are suppressed within the trap, unless the field magnitude at the minimum point is very small [12].

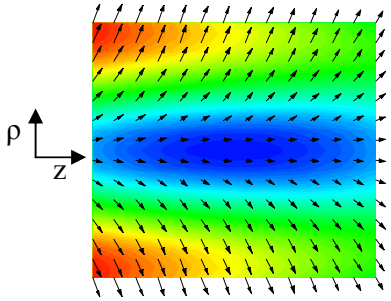

Figure 5 – Field of the trap shown in Figure 3. The center of the plot (z=ρ=0) is at the center of the trap. Red indicates high field magnitudes, while blues indicates low magnitudes. The value of θ is chosen to correspond to a plane passing midway between the rods.

In fields produced by such Ioffe-Pritchard traps, the magnetic field magnitude (and consequently the potential, as per equation (2.1.5)) will approximate that of a simple harmonic oscillator [25]. Such oscillators may be characterized by frequencies along each Cartesian axis as given by [12]

$$\frac{\omega_i}{2\pi} = \frac{1}{2\pi}\sqrt{\frac{\mu}{m}\frac{d^2\left|\vec{B}\right|}{dX_i^2}} \equiv f_i \qquad (2.1.13)$$

where m is the mass of the atom and i and X_i indicate the axis in question (e.g. when i=3 then $\omega_i=\omega_3=\omega_z$, $X_i=z$, etc).

Typically, wire traps are highly elongated (along the z-axis in the present case); the frequency of motion in this direction is therefore considerably lower than for motion in directions perpendicular to the elongated axis. This frequency is referred to as the longitudinal frequency since it corresponds to motion along the longest axis of the trap (i.e., parallel to the rods for this particular trap), while the other two, higher frequencies, are the transverse frequencies. Correspondingly, we can speak of longitudinal and transverse confinement.

In a trap with an approximately harmonic potential, the frequency is related to the trap width[4] w_i for atoms of a given temperature T by [7]

$$w_i = 2\sqrt{\frac{2k_B T}{m\omega_i^2}} \qquad (2.1.14)$$

where k_B is the Boltzmann constant. As the frequency increases, the trap becomes less elongated along the axis in question. For anharmonic traps, as discussed in Chapter 4, trap widths provide better quantitative representations of trap characteristics than trap frequencies.

Typically, the term "Ioffe-Pritchard trap" is used to refer to any trap with a field approximating a harmonic potential sufficiently close to its center and a non-zero minimum,

[4] A commonly used convention is to refer to the amplitude r_i which equals $0.5w_i$.

rather than just the configuration in Figure 3. The field at the minimum is often referred to as the "Ioffe-Pritchard (IP) field".

2.1.3 Wire traps

The systems described above are fairly large, and the trap centers are typically far from the components generating the fields, on the scale of tens of centimeters. Since the field gradient falls with distance from the generating structures, creating sufficiently steep traps (enabling not only tightly confining potentials but also a better resolution in tailoring complex potentials on a small scale) requires high currents, which in turn requires a great deal of power and generates a large amount of heat; dissipating that heat in a UHV environment can be a considerable concern in its own right.

By reducing the size of the system, the generating structures can be brought closer to the trap. In order to have control on the quantum level, we desire tight traps with a resolution comparable to the de Broglie wavelength, on the order of microns at ultralow temperatures, and therefore the sources need to be within microns of the trap.

The simplest way to do this is to miniaturize existing systems like those described in the previous sections. However, such systems can only be miniaturized so far; small coil windings are difficult to construct, and since these systems must surround the trap, they restrict optical access to the trap center, making it considerably more difficult to view the trap as well as to use laser cooling or other applications requiring illuminating the trapped atoms.

A common way to solve this problem is by using a combination of fields generated by wire structures lying in a plane (or planes), which can be located only on one side of the trapping region, combined with an external field that is roughly homogenous (the latter is known as the bias field) [27]. The wires in such a system can be miniaturized easily, without restricting optical access to the trap. In our case, multiple wires are miniaturized and integrated onto a single chip using semiconductor lithographic techniques. At first glance, the miniaturization possible for such a system is limited, since coils are used to generate the bias field. However, high gradients are not necessary for this field (and are, in fact, undesirable), so the bias coils can be run at a much lower current level than that needed for trapping coils. In this section, several configurations ([12, 28-30]) of such wire traps will be described[5].

[5] A word regarding terminology: in the following sections, several wire configurations are discussed where there are two parallel wires (or wire sections) and one wire which is perpendicular to the other two. The former are called "legs", while the latter is referred to as the "crosspiece".

2.1.3.1 The side guide

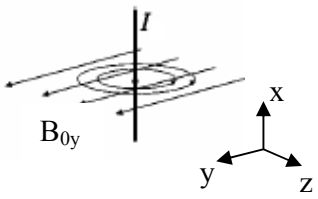

Figure 6 – The side guide. The center of the wire here is assumed to be at (0,0,0) (adapted from [27])

First let us consider a simple configuration known as the side guide. This consists of a single long wire, which is perpendicular to the plane of the bias field (Figure 6).

If a wire is long relative to the distance r from the wire, it can be approximated as being infinitely long; in cylindrical coordinates, this yields (assuming a wire running along the z axis):

$$\vec{B} = -\frac{\mu_0}{2\pi}\frac{I}{r}\hat{\theta} \tag{2.1.15}$$

where I is the current in Amperes running through the wire and μ_0 is the permeability of the vacuum[6]. The radial gradient of the field magnitude is

$$\frac{dB}{dr} = -\frac{\mu_0}{2\pi}\frac{I}{r^2} \tag{2.1.16}$$

In the coordinate system used in Figure 6, if we add a bias field in the y direction (designated as B_{0y}), equation (2.1.15) can be rewritten as

$$\vec{B} = \left(B_{0y} - \frac{\mu_0 I}{2\pi}\frac{z}{y^2+z^2}\right)\hat{y} + \frac{\mu_0 I}{2\pi}\frac{y}{y^2+z^2}\hat{z} \tag{2.1.17}$$

A field minimum will result when the magnitudes of both the y- and z- vector components become zero (as can be seen from equation (2.1.17), there is no x-component to the field when the wire is parallel to the x axis). The z-component is zero at points directly above the wire (i.e. y=0); at such points, equation (2.1.17) becomes

$$\vec{B} = \left(B_{0y} - \frac{\mu_0}{2\pi}\frac{I}{z}\right)\hat{y} \tag{2.1.18}$$

Consequently, the field will have a minimum at a distance above the wire determined by

$$z_0 = \frac{\mu_0}{2\pi}\frac{I}{B_{0y}} \tag{2.1.19}$$

[6] In our applications, it is convenient to work in units of mm and Gauss, for which $\mu_0=4\pi$.

In *two* dimensions (in a plane perpendicular to the wire) the result is a quadrupole trap. The trap depth[7] D_T (the energy above which atoms will escape out the top of the trap) whose minimum is at (x_0,y_0,z_0) is, in general[8], determined by

$$D_T = \frac{\mu}{k_B}\left(\left|\vec{B}\left(x_0, y_0, z \to \infty\right)\right| - \left|\vec{B}\left(x_0, y_0, z_0\right)\right|\right) \qquad (2.1.20)$$

Since the field strength at the minimum point is zero in this case, the trap depth is

$$D_T^Q = \frac{\mu}{k_B}\left|B_{0y}\right| \qquad (2.1.21)$$

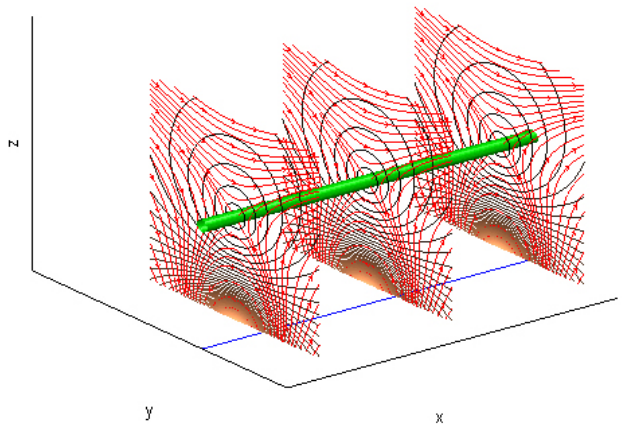

Figure 7 – Field of a side guide. The blue line at the bottom of the figure indicates the wire's position; the red lines indicate field direction; the dark lines indicate field magnitude; and the green surface indicates a constant (arbitrary) field value, thereby constituting a guide.

The z-axis gradient of the field is

$$\frac{\partial\left|\vec{B}\right|}{\partial z} = -\frac{\mu_0 I}{4\pi}\frac{2B_{0y}\pi\left(y^2 - z^2\right) + \mu_0 I z}{\left(y^2 + z^2\right)^{3/2}\sqrt{\left(B_{0y}\pi z - \frac{1}{2}\mu_0 I\right)^2 + \left(B_{0y}\pi y\right)^2}} \qquad (2.1.22)$$

Directly over the wire, (2.1.22) becomes

$$\left.\frac{\partial\left|\vec{B}\right|}{\partial z}\right|_{y=0} = \frac{\mu_0 I}{2\pi z^2}\cdot \mathrm{sgn}(B_{0y}\pi\left(z - \frac{\mu_0 I}{B_{0y}\pi}\right)) \qquad (2.1.23)$$

where sgn is the sign function[9].

Seen in *three* dimensions however, the magnetic field's equipotential surfaces (see Chapter 4) form "tubes" with zero field along its central axis, as shown in Figure 7; atom motion parallel to the wire thus occurs freely and is restricted only in directions perpendicular

[7] The trap depth is an energy quantity, but it is convenient to express it in terms of an equivalent temperature, where 1 mK= 1.38 x 10^{-26} J.
[8] Assuming, as is usually the case, that the lowest potential at large distances from the trap center is encountered at large z, rather than large x or y.
[9] Also known as the signum function

to the wire (the transverse direction). Therefore, this configuration is not suitable for trapping, but it can be used to guide atoms between different regions [12].

Even used as a guide, we note the fact that the side-guide field vanishes at the potential minimum, thereby allowing atoms to escape. This Majorana loss can be overcome by adding a bias field parallel to the wire (designated as B_{0x}). Doing so removes the vanishing minimum, and changes the form of the potential in its vicinity to a harmonic form [12]. The field is then characterized by its curvature in the transverse directions, which is given by

$$\left.\frac{d^2B}{dy^2}\right|_{y=0,z=z_0} = \left.\frac{d^2B}{dz^2}\right|_{y=0,z=z_0} = \left(\frac{2\pi}{\mu_0 I}\right)^2 \frac{B_{0y}^4}{|B_{0x}|} \qquad (2.1.24)$$

If B_{0x} is homogenous, the location of the minimum will not change. The trap depth is

$$D_T^{IP} = \frac{\mu}{k_B}\left(\sqrt{B_{0x}^2 + B_{0y}^2} - |B_{0x}|\right) \qquad (2.1.25)$$

The exact depth of the trap depends on the values of B_{0x} and B_{0y}, but is always smaller[10] than D_T^Q .This results in a "flatter", shallower trap, as can be seen in Figure 8.

It should be noted that under the conditions described above, the minimum will always be directly above the wire. Adding a bias field in the z direction (B_{0z}) moves the minimum along the y axis, but it also changes the height of the minimum. For $B_{0z} \neq 0$, the resulting field curvatures in the vicinity of the minimum in the y and z directions are not identical, as they are in the $B_{0z}=0$ case (as expressed in equation (2.1.24)).

It should also be noted that the analysis above is for a wire whose field follows the infinite-length approximation[11]. In the case of a wire segment of finite length, it is mathematically possible to obtain a three-dimensional potential trap in conjunction with an external potential (such as a gravitational field). Practically, however, such a configuration cannot be built, since any finite-length segment must be connected to leads carrying current – which themselves create a magnetic field. As a result, the side *guide* can only guide atoms, not trap them. In order to create atom traps, we use wires in configurations such as those described below.

[10] This can be easily proven by means of the triangle inequality theorem.
[11] See Appendix B for the equation describing the fields generated by non-infinite wires

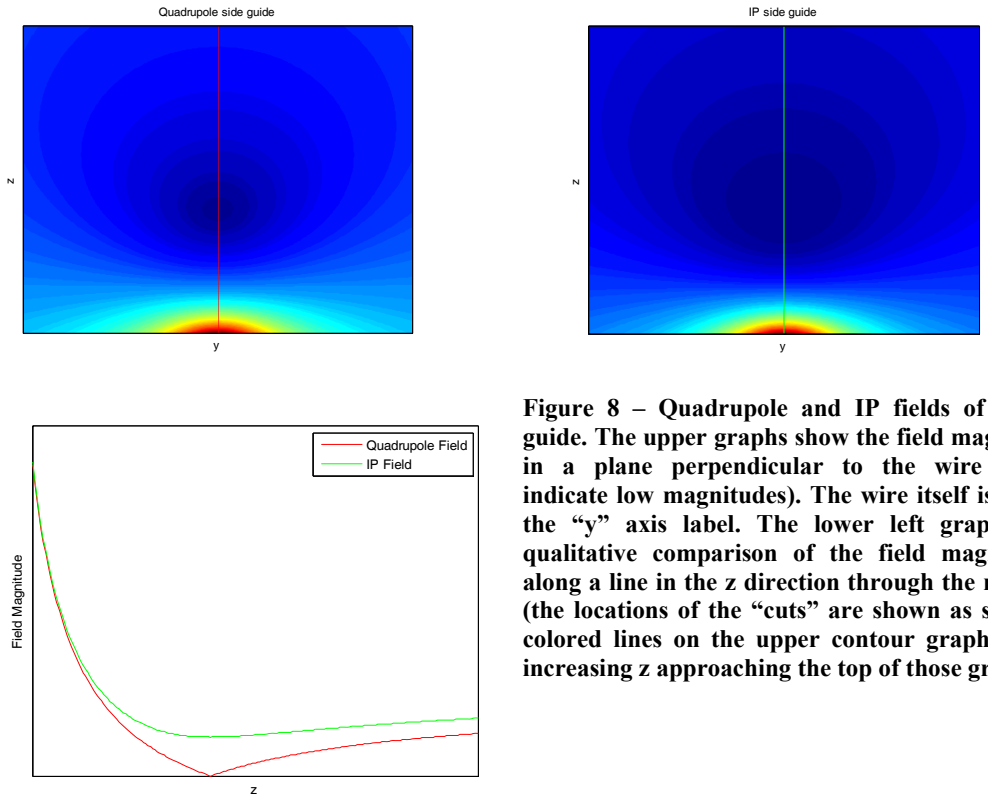

Figure 8 – Quadrupole and IP fields of a side guide. The upper graphs show the field magnitude in a plane perpendicular to the wire (blues indicate low magnitudes). The wire itself is below the "y" axis label. The lower left graph is a qualitative comparison of the field magnitudes along a line in the z direction through the minima (the locations of the "cuts" are shown as straight colored lines on the upper contour graphs, with increasing z approaching the top of those graphs)

2.1.3.2 The U-wire trap

As mentioned above, the side guide provides only two-dimensional trapping (in the transverse directions); atoms are free to move along the wire's length. In order to create a three-dimensional trap, longitudinal trapping must be supplied as well. One method of doing so is known as the U-wire trap (or U-trap), which is a common configuration for creating a quadrupole trap. In such a trap, the wire is twisted into the shape of a U, as shown in Figure 9.

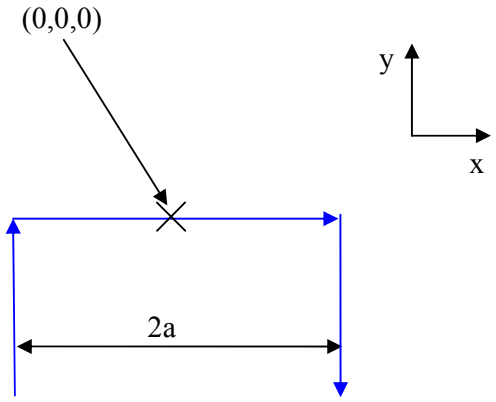

Figure 9 – The U-wire trap, seen from along the z axis. The blue arrows indicate the direction of current flow for positive I.

If the "legs"[12] of the U are sufficiently long (relative to the length of the crosspiece[13] and the distance to the trapping region) for an infinite-length approximation to apply, the resulting field is

$$\begin{aligned}
\vec{B} &= B_x\hat{x} + B_y\hat{y} + B_z\hat{z} \\
B_x &= \frac{\mu_0 I}{4\pi}\left(\frac{z}{y\chi_+ + \chi_+^2} - \frac{z}{y\chi_- + \chi_-^2}\right) \\
B_y &= \frac{\mu_0 I}{4\pi}\frac{z}{y^2+z^2}\left(\frac{x-a}{\chi_-} - \frac{x+a}{\chi_+}\right) \\
B_z &= \frac{\mu_0 I}{4\pi}\left(\frac{y}{y^2+z^2}\left(\frac{a-x}{\chi_-} + \frac{a+x}{\chi_+}\right) + \frac{x-a}{y\chi_- + \chi_-^2} - \frac{x+a}{y\chi_+ + \chi_+^2}\right)
\end{aligned} \tag{2.1.26}$$

where the length of the crosspiece is 2a and

$$\chi_\pm \equiv \sqrt{(a \pm x)^2 + y^2 + z^2}$$

In the x=0 plane, the field becomes

$$\vec{B}(x=0) = \frac{a\mu_0 I}{2\pi\sqrt{a^2+y^2+z^2}}\left(\frac{-z}{y^2+z^2}\hat{y} + \left(\frac{y}{y^2+z^2} - \frac{1}{y+\sqrt{a^2+y^2+z^2}}\right)\hat{z}\right) \tag{2.1.27}$$

By adding a bias field in the y and z directions, a minimum can be achieved at any point in the x=0 plane; B_{0y} and B_{0z} are chosen to cancel B_y and B_z at the desired point. The resulting field is shown in Figure 10, and the trap has the shape of an ellipsoid.

As can be seen in equations (2.1.26) and (2.1.27), the field has a nonzero x component at $x \neq 0$; at x=0 the field magnitude is zero at the minimum point. Also, the center of the trap is not directly above the wire for a bias field exclusively in the y direction, but is displaced on the y axis; this is due to the z-axis component of the field generated by the "legs" of the U. This displacement depends on the separation between the legs (2a) and decreases as a increases, as does the longitudinal confinement. This displacement can be offset by changing B_{0z}.

[12] A note on terminology – throughout this work, in a wire trap, "leg" will refer to the wire (or wires) creating the longitudinal confinement (which are, in the coordinate system used here, parallel to the y axis) while "crosspiece" refers to that wire (or wire segment) parallel to the x axis.

[13] If the crosspiece is also much longer than the distance to the trapping region, so that an infinite-length approximation applies, the U-trap approximates a side guide.

a=4mm, x_0=0mm, y_0=0mm, z_0=6mm

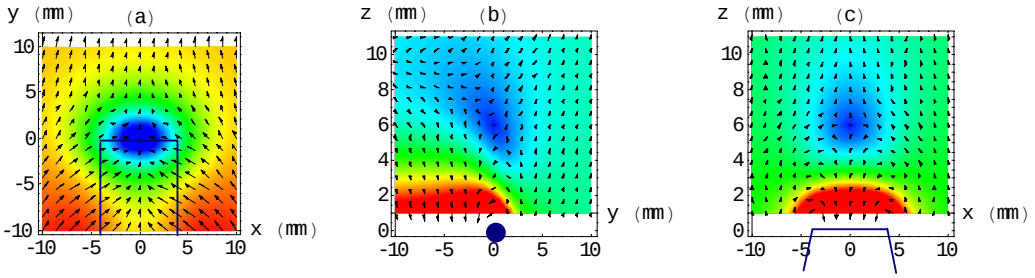

Figure 10 – Planar cuts through the field of a U-trap. The bias field was selected so that the minimum is over the center of the wire; hence, $B_{0z}\neq 0$. Each cut is taken through the minimum point (which is 6 mm above the origin). Blue indicates low field magnitudes, and red indicates high magnitudes. The indigo lines (or dot in (b)) indicate the position of the wire. The effect of the legs can be seen in the increased field magnitude at the lower left corner of (b).

The depth of the trap at the minimum point is given by

$$D_T^U = \frac{\mu}{k_B}\sqrt{B_{0y}^2 + B_{0z}^2} \qquad (2.1.28)$$

It should be noted that by altering the location of the minimum, once the trap is established, it is possible to move the atom cloud to various locations (this is true for the other trap configurations as well).

Since the field magnitude reaches zero at the minimum point, the U-trap is not suitable for trapping atoms at temperatures where Majorana losses become significant. For that, other trap types must be used, which are described below.

2.1.3.3 The Z-wire trap

In the Z-trap, the wire is twisted into the shape of a Z with right angles (Figure 11).

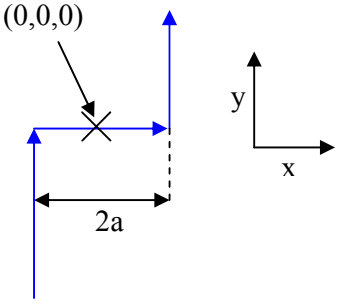

Figure 11 – The Z-wire trap, seen from along the z axis. The blue arrows indicate the direction of current flow for positive I.

If the "legs" are long enough to be considered infinitely long, the field generated by the wire[14] is (using the same notation as in equation (2.1.26))

$$\begin{aligned} B_x &= \frac{\mu_0 I}{4\pi}\left(\frac{z(\chi_- + y)}{\left((a-x)^2+z^2\right)\chi_-} + \frac{z}{y\chi_+ + \chi_+^2}\right) \\ B_y &= \frac{\mu_0 I}{4\pi}\frac{z}{y^2+z^2}\left(\frac{x-a}{\chi_-} - \frac{x+a}{\chi_+}\right) \\ B_z &= \frac{\mu_0 I}{4\pi}\left(\frac{y}{y^2+z^2}\left(\frac{a-x}{\chi_-} + \frac{a+x}{\chi_+}\right) - \frac{x-a}{\chi_-^2 - y\chi_-} - \frac{x+a}{\chi_+^2 + y\chi_+}\right) \end{aligned} \qquad (2.1.29)$$

It can be demonstrated from equation (2.1.29) that B_x is nonzero except when z=0. Therefore, the magnitude of the field from the wire alone will always be nonzero for $z \neq 0$.

The trap is formed by adding B_{0y} to the wire-generated field. This results in a field which is nonzero at the minimum and harmonic in its vicinity [9, 10].

Adding an x-axis component to the bias field reduces the trap depth. Care must be taken, however, not to select too large a value of B_{0x} , otherwise the field magnitude will reach zero at some point (or points). Adding a bias field on the z-axis moves the location of the minimum on both the x and the y axes.

Because the x-axis field of the Z-trap is inhomogeneous, determining the bias field required for a minimum to occur at a specified point is somewhat less straightforward than in the cases of the side guide or the U-trap. If the bias field is parallel to the y axis, the minimum will be directly above the center of the crosspiece. Under these conditions, the bias field necessary to achieve a minimum at height z_0 is

$$B_{0y} = \frac{\mu_0 I}{2\pi}\frac{a^6 + 3a^4 z_0^2 + a^2 z_0^4 + z_0^6}{a z_0\left(a^2+z_0^2\right)^{3/2}\left(a^2+2z_0^2\right)} \qquad (2.1.30)$$

The field at the minimum point is

$$\begin{aligned} \vec{B} &= \frac{\mu_0 I}{2\pi}\left(\frac{z_0}{a^2+z_0^2}\hat{x} + \frac{z_0^3\left(z_0^2-a^2\right)}{a\left(a^2+z_0^2\right)^{3/2}\left(a^2+2z_0^2\right)}\hat{y}\right) \\ \left|\vec{B}\right| &= \frac{\mu_0 |I|}{2\pi}\frac{|z_0|\sqrt{a^2+5a^6z_0^2+9a^4z_0^4+2a^2z_0^6+z_0^8}}{\left(a^2+z_0^2\right)^{3/2}\left(a^3+2z_0^2\right)} \end{aligned} \qquad (2.1.31)$$

and depth of the resulting trap is

$$D_T^Z = \frac{\mu_0 |I|}{2\pi a}\left(\frac{\left(a^6+3a^4z_0^2+a^2z_0^4+z_0^6\right)}{|z_0|\left(a^2+z_0^2\right)^{3/2}\left(a^2+2z_0^2\right)} - \frac{a|z_0|\sqrt{a^8+5a^6z_0^2+9a^4z_0^4+2a^2z_0^6+z_0^6}}{\left(a^2+z_0^2\right)^{3/2}\left(a^3+2az_0^2\right)}\right) \qquad (2.1.32)$$

[14] Some of the terms in the equations for B_x and B_z will have their signs reversed for the case of a Z-wire that is the mirror image (about the y-axis) of the wire in Figure 11.

As can be seen in Figure 12, the IP field (at the trap center) is not aligned with the x axis (this is especially clear in Figure 12d). The angle of deviation from the x axis is given by

$$\theta_B^Z = \sin^{-1}\left(\frac{z_0^2\left(z_0^2 - a^2\right)\cdot \mathrm{sgn}(I\cdot z_0)}{\sqrt{a^8 + 5a^6 z_0^2 + 9a^4 z_0^4 + 2a^2 z_0^6 + z_0^8}}\right) \qquad (2.1.33)$$

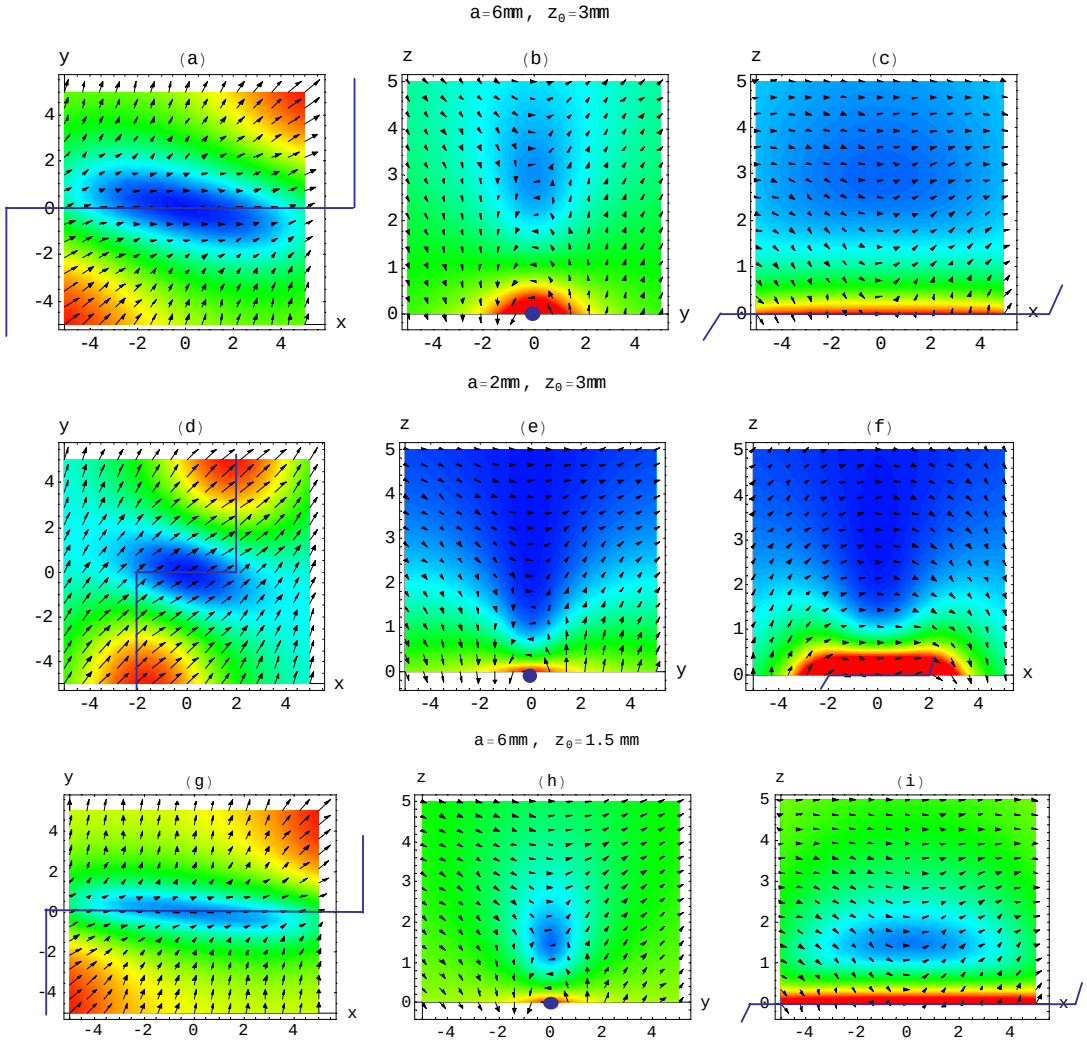

Figure 12 – The field generated by the Z-trap for different values of a and z_0. The plots show cuts in the xy (a, d and g), yz (b, e and h), and xz planes (c, f and i), taken through the trap minimum. Blues indicate low field regions while reds indicate a high field. The indigo lines indicate the location of the wire (the circle in the yz cuts indicates the location of the crosspiece). Note that the trap does exist in (e) and (f), but is so shallow that it is hard to see.

and is shown for various values of a and z_0 in Figure 13. It can be seen that in general, as a increases, the angular deviation of the IP field decreases; however the *magnitude* of the IP field also decreases with a (Figure 14a). Thus, for sufficiently large values of a, the Z-trap, like the U-trap, approximates a side guide near its center.

Figure 12 also shows that the trap has the shape of an elongated ellipsoid – we will call the axis of elongation the *longitudinal axis*. Unlike the case of the U-trap, this longitudinal axis is not aligned with the crosspiece, but is rather rotated at some angle. It is important to note that the rotation angle is *not* necessarily the same as the angle of deviation of the IP field given by equation (2.1.33) – this can again be seen especially clearly in Figure 12d. This rotation is caused by the lack of symmetry in the z-axis component of the field, which is generated by both the crosspiece and the legs (as opposed to the x-axis component, which is generated solely by the legs, and the y-axis component which is generated solely by the crosspiece).

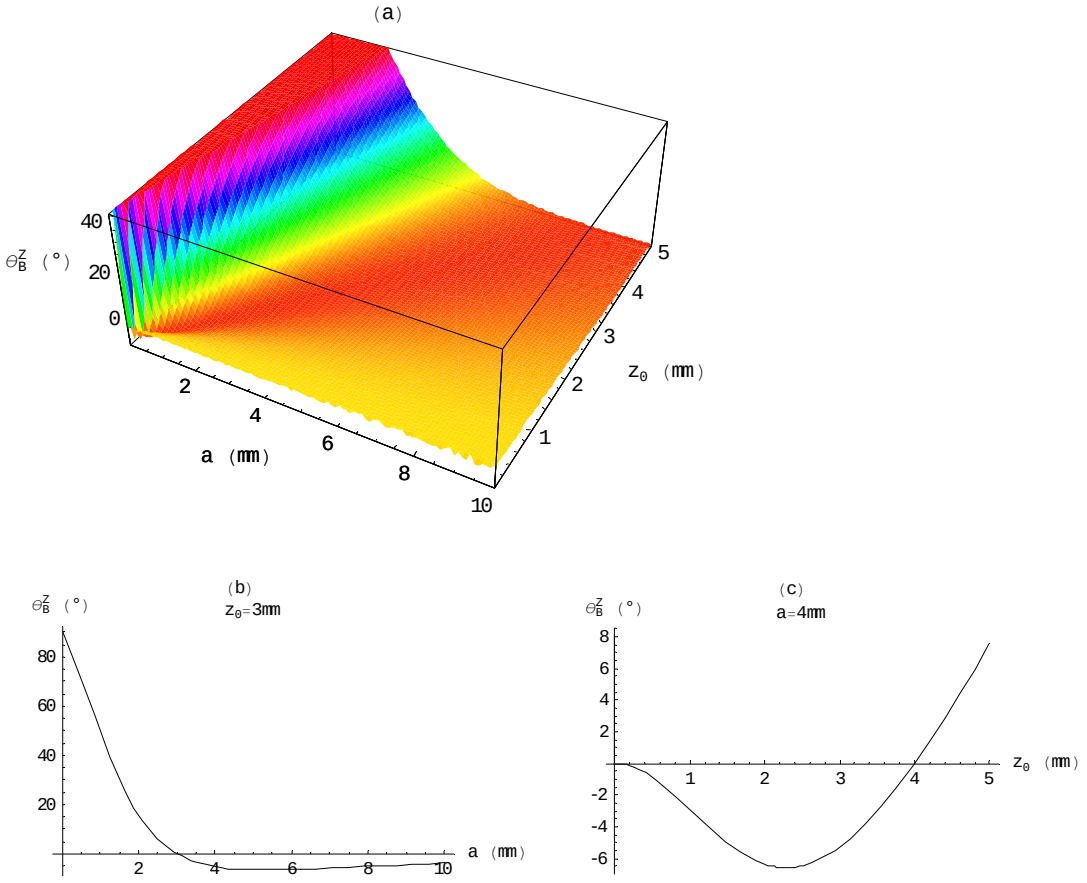

Figure 13 – Angle of deviation θ_B^z for varying values of a and z_0 (a). Figures (b) and (c) show cuts through figure (a) at specific values of z_0 and a, respectively. Negative angle values indicate the field is twisted in a clockwise direction relative to the x axis.

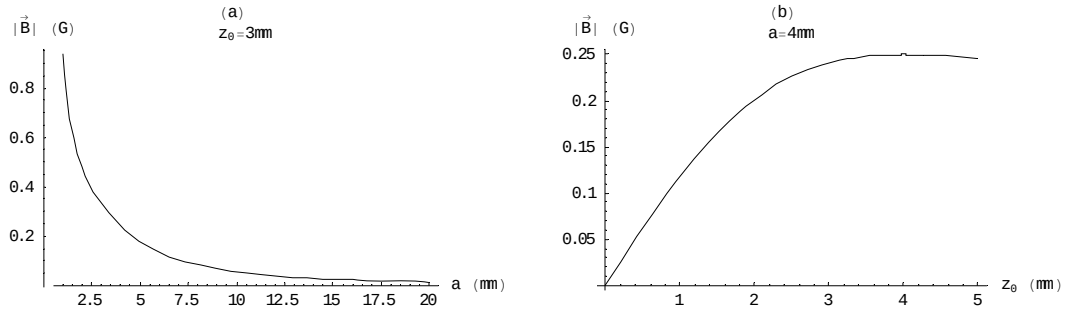

Figure 14 – Variation in the field at its minimum as a function of a (figure (a)) and z_0. These graphs assume a current of 1A; the magnitude is linearly proportional to the current.

In order to find the main axes of the ellipsoid, we will find the eigenvalues of the field's Hessian matrix, from which it is possible to calculate both the angle of the longitudinal axis as well as the frequencies of the trap.

The Hessian matrix[15] of the field magnitude in the xy plane is:

$$H \equiv \begin{pmatrix} \frac{\partial^2 |\vec{B}|}{\partial x^2} & \frac{\partial^2 |\vec{B}|}{\partial x \partial y} \\ \frac{\partial^2 |\vec{B}|}{\partial y \partial x} & \frac{\partial^2 |\vec{B}|}{\partial y^2} \end{pmatrix} = \frac{\mu_0 |I|}{2\pi} \begin{pmatrix} H_{11} & H_{12} \\ H_{21} & H_{22} \end{pmatrix}$$

$$H_{11} = \frac{\left(a^3 + 2az_0^2\right)\left(a^6 + 6a^4 z_0^2 + 4a^2 z_0^4 + z_0^6\right)}{|z_0|\left(a^2 + z_0^2\right)^{5/2}\left(a^2 + 2z_0^2\right)\left(a^8 + 5a^6 z_0^2 + 9a^4 z_0^4 + 2a^2 z_0^6 + z_0^8\right)^{1/2}}$$

$$H_{12} = \frac{a\left(a^3 + 2az_0^2\right)\left(a^4 + a^2 z_0^2 + z_0^4\right)}{|z_0|^3\left(a^2 + z_0^2\right)^2\left(a^8 + 5a^6 z_0^2 + 9a^4 z_0^4 + 2a^2 z_0^6 + z_0^8\right)} \qquad (2.1.34)$$

$$H_{21} = \frac{a\left(a^3 + 2az_0^2\right)\left(a^4 + a^2 z_0^2 + z_0^4\right)}{|z_0|^3\left(a^2 + z_0^2\right)^2\left(a^8 + 5a^6 z_0^2 + 9a^4 z_0^4 + 2a^2 z_0^6 + z_0^8\right)}$$

$$H_{22} = \frac{\left(a^3 + 2az_0^2\right)\left(a^8 + 6a^6 z_0^2 + 10a^4 z_0^4 + 7a^2 z_0^6 + 3z_0^8\right)}{|z_0|^5\left(a^2 + z_0^2\right)^{3/2}\left(a^2 + 2z_0^2\right)\left(a^8 + 5a^6 z_0^2 + 9a^4 z_0^4 + 2a^2 z_0^6 + z_0^8\right)}$$

We will mark the eigenvectors[16] of H as

$$v_1 = \begin{pmatrix} a_1 \\ b_1 \end{pmatrix} \qquad v_2 = \begin{pmatrix} a_2 \\ b_2 \end{pmatrix}$$

The equations

$$a_i x + b_i y = 0 \qquad (2.1.35)$$

[15] It is also possible to calculate the three dimensional Hessian matrix; the results are the same, except that an eigenvector pointing directly in the z-axis direction is added, since the trap rotation is solely around that axis..

[16] The explicit forms of the eigenvectors' equations are quite lengthy and will therefore not be given here; they can be calculated with the program described in Appendix F.1.3.

describe two lines which pass through the origin (in the xy plane). One line (i=1) is oriented with the longitudinal axis, while the second line is oriented in the direction of maximum field increase (this is the trap's *transverse axis*). The angle of rotation of the longitudinal axis is therefore given by

$$\theta_T^Z = \tan^{-1}\left(-\frac{b_1}{a_1}\right) \qquad (2.1.36)$$

Figure 15 shows the values of θ_T^Z for different values of a and z_0. Because of this angle, it can be more convenient in such cases to use a rotated (x'y'z) coordinate system where x' is aligned with the longitudinal axis, so that

$$\begin{aligned} x' &= x \cdot \cos\theta_T^Z \\ y' &= y \cdot \cos\theta_T^Z \\ z &= z \end{aligned} \qquad (2.1.37)$$

This will not be done here, to simplify comparisons between the different types of traps.

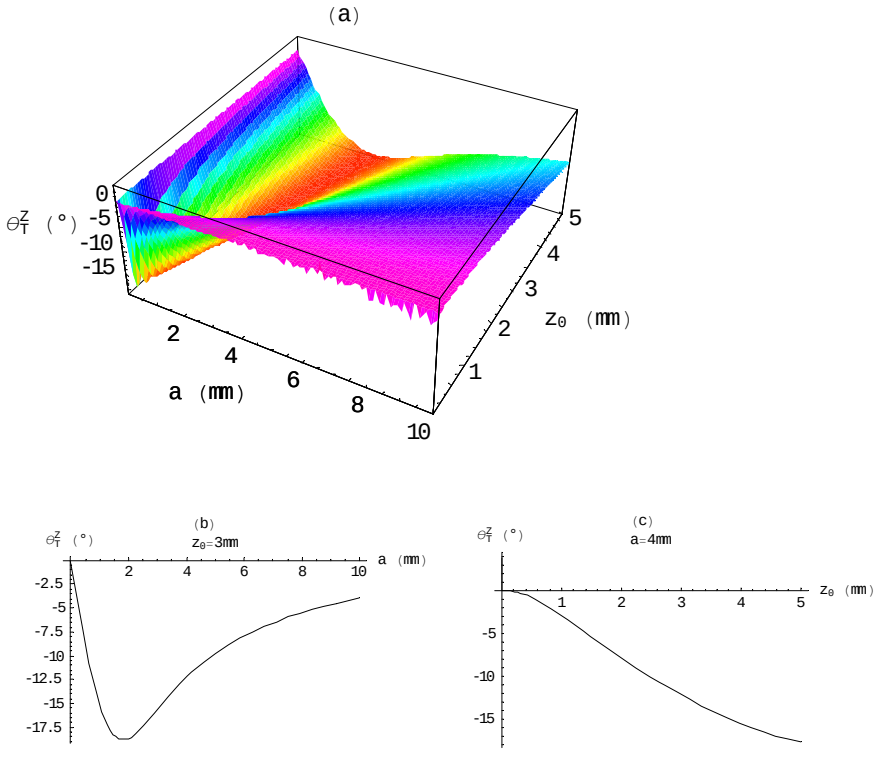

Figure 15 – The rotation of field's longitudinal axis relative to the x axis for varying values of a and z_0. The values selected in figures b and c are the same as for Figure 13. Negative angle values indicate the field is rotated in a clockwise manner.

The frequencies of the trap can be calculated by means of equation (2.1.13). If the minimum is at the origin, and we define

$$c_i \equiv -\frac{b_i}{a_i} \qquad \hat{u}_i \equiv \frac{\hat{x} + c_i \hat{y}}{1 + c_i^2}$$

then the second derivative of the field magnitude along the line with slope c_i is

$$\frac{\partial^2 |\vec{B}|}{\partial u_i^2} = \frac{1}{1+c_i^2}\frac{\partial^2 |\vec{B}|}{\partial x^2} + \frac{2c_i}{1+c_i^2}\frac{\partial^2 |\vec{B}|}{\partial x \partial y} + \frac{c_i^2}{1+c_i^2}\frac{\partial^2 |\vec{B}|}{\partial y^2} \qquad (2.1.38)$$

The resulting trap frequencies are shown in Figure 16. The three variables which affect the frequency are the distance between the legs, the height of the minimum, and the current. It can be seen that the transverse frequency increases with the width of the Z, while the longitudinal frequency does so to a much lesser extent, and eventually reaches a constant value. This is because the frequency is determined by both the x- and y-axis components (since the trap is rotated); as a increases, the x-component decreases, but the y-component increases. In addition, increasing current also increases the frequency, while frequencies drop precipitously as the height of the minimum over the wire is increased. The transverse frequencies in the xy plane and along the z axis converge except for small values of a.

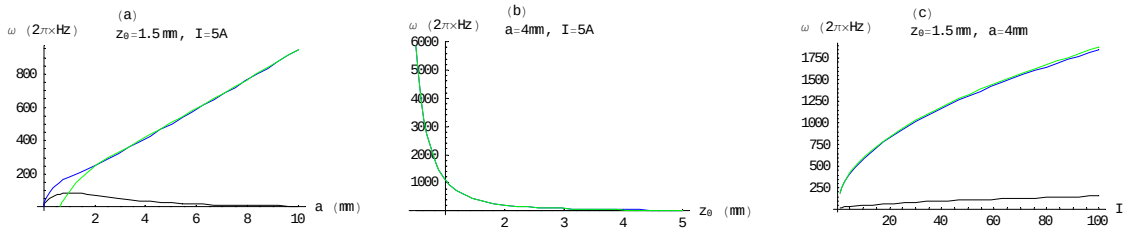

Figure 16 – Frequencies of the Z-trap. In each graph, two variables (out of current, separation of the legs, and height of the minimum) are kept constant. The blue line indicates the transverse frequency in the xy plane, the green line indicates the transverse frequency along the z axis, and the black line indicates the longitudinal frequency (in graph (b), the longitudinal frequency is too small to see; it reaches a maximum of approximately 35 2π×Hz at z0=1.3mm).

It should be noted that the above equations give the angle of the trap's rotation and its frequencies at the trap center. The values of these parameters may change at greater distances from the minimum.

2.1.3.4 The X-wire trap

Both the U-wire and the Z-wire traps are composed of a single wire segment. Because of this, the longitudinal and transverse confinements are interdependent; since both are

generated by sections of the same wire and changing the current to alter one will also alter the other. This can be a problem, for example, when transferring atom ensembles between two different traps (for example from a U-trap to a Z-trap); the longitudinal and transverse frequencies of the two traps should match as closely as possible during the transfer (see section 5.1), but changing the transverse frequency in one of the traps to be closer to the other will also change its longitudinal frequency, possibly *away* from the desired value.

One way to overcome this is to use a trap composed of several unconnected wires, some of which provide the transverse confinement and others which provide the longitudinal confinement. Since the currents in the longitudinal wires are unrelated to those in the transverse wires, the confinements can be altered independently.

A simple trap of such a type is the X-wire trap. This simply consists of two perpendicular wires, as shown in Figure 17; it can be thought of as a side guide with a perpendicular wire added to supply longitudinal confinement. We will designate the wire parallel to the x axis as the "transverse wire" (as it provides the transverse confinement) and the other wire as the "longitudinal wire". We note that this distinction is arbitrary if the wires lie in the same plane since then the structure is symmetric – switching the bias fields will swap the longitudinal and transverse directions – but in any practical design the wires must not cross and the actual structure would not be symmetric. Likewise, we will define the confinement along the x axis as the longitudinal confinement (or, more properly, the x' axis, where x' is the trap's longitudinal axis, since the trap is rotated as in the case of the Z-trap).

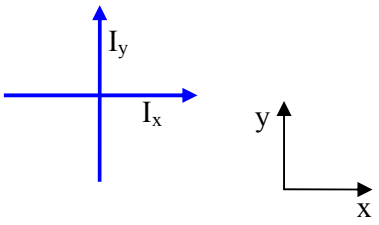

Figure 17 – The X-trap. The origin lies at the crossing point of the two wires.

The field generated by this trap (assuming infinitely long wires and that the transverse wire is at z=0) is

$$\vec{B}\left(x,y,z,I_{\_},I_{|}\right)=\frac{2I_y\left(z-z_d\right)}{x^2+\left(z_d-z\right)^2}\hat{x}-\frac{2I_x z}{y^2+z^2}\hat{y}+\left(\frac{2I_x y}{y^2+z^2}-\frac{2I_y x}{x^2+\left(z_d-z\right)^2}\right)\hat{z} \quad (2.1.39)$$

where z_d is the difference between the z-coordinates of the two wires (negative values mean the longitudinal wire is below the transverse one), I_x is the current in the wire parallel to the x axis and I_y is the current in the wire parallel to the y axis. A trap minimum will exist if $I_y \leq I_x$.

Since, moving along the x axis, the magnitude of the field generated by the longitudinal wire increases as the origin is approached, a bias field on the x axis is required – in addition to that on the y axis – in order to attain a trap. The y-axis bias field required to form a trap at height z_0 over the origin is related to the x-bias field B_{0x} and is given by

$$B_{0y} = \frac{B_{0x} I_y z_0^3 (z_d - z_0) + 2\left(I_x^2 (z_d - z_0)^3 - I_y^2 z_0^3\right)}{I_x z_0 (z_d - z_0)^3} = \frac{B_{0x} I_y}{I_x z'^2} + \frac{2I_x}{z_0} - \frac{2I_y^2}{I_x z_0 z'^3} \quad (2.1.40)$$

where

$$z' \equiv \frac{z_d - z_0}{z_0}$$

B_{0x} must also be properly selected. If it is below a certain critical value, a double-well trap will form (i.e. there will be two minima, neither of which are at the origin). Thus in order to obtain a single trap, the x-axis bias field must fulfill the conditions[17]

$$\begin{aligned} \mathrm{sgn}(B_{0x}) &= -\mathrm{sgn}(I_y) \\ |B_{0x}| &> \left|\frac{2I_y}{z_d - z_0}\right| \end{aligned} \quad (2.1.41)$$

The resulting field can be seen in Figure 18. It can be seen that like the Z-trap, this trap is rotated relative to the x-axis, though to a smaller extent. It is also apparent that the longitudinal confinement for this trap is much weaker than the transverse confinement.

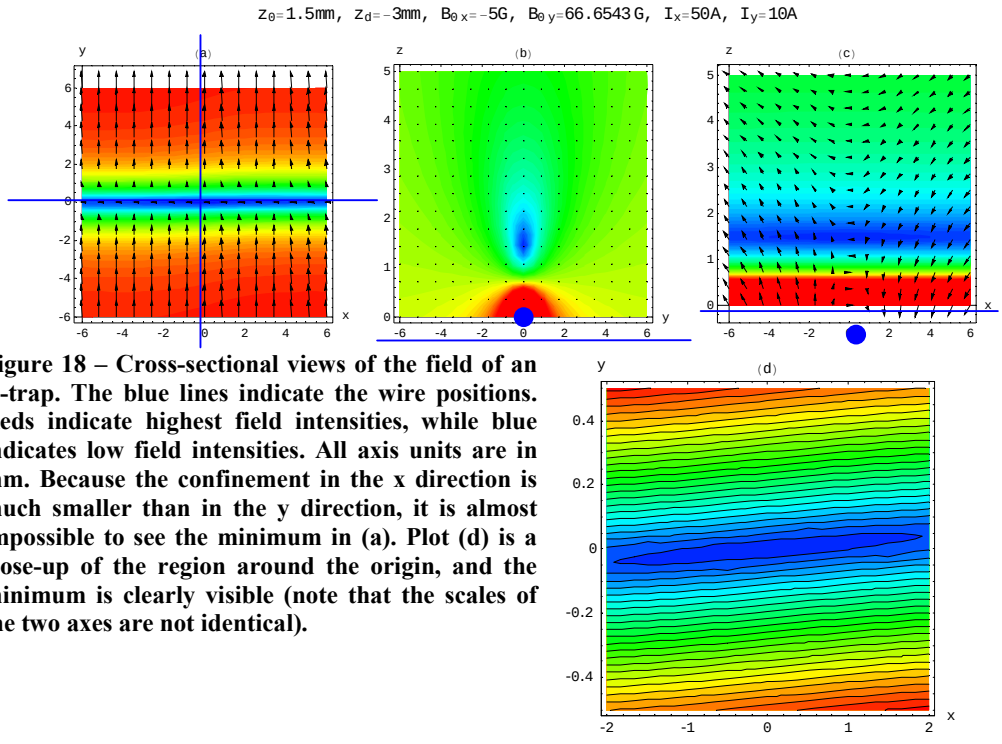

Figure 18 – Cross-sectional views of the field of an X-trap. The blue lines indicate the wire positions. Reds indicate highest field intensities, while blue indicates low field intensities. All axis units are in mm. Because the confinement in the x direction is much smaller than in the y direction, it is almost impossible to see the minimum in (a). Plot (d) is a close-up of the region around the origin, and the minimum is clearly visible (note that the scales of the two axes are not identical).

[17] This is for $z_0>0$, otherwise the signs are inverted.

2.1.3.5 The H-wire trap

Another type of multisegment wire trap is the H-trap. Like the X-trap, the longitudinal and transverse frequencies can be altered independently by altering the currents in the separate wires of the trap. In common with all other traps discussed in this thesis, all the wires lie in a horizontal plane. In the following discussion, we first consider the simplified case in which all the wires are in the *same* plane.

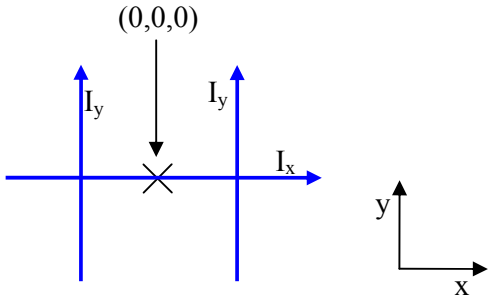

Figure 19 – Schematic of the H-trap. In the case shown here, both legs carry equal and copropagating currents.

The H-trap is composed of two parallel wires, through each of which a current I_y is flowing, and a third wire perpendicular to them through which a current I_x is flowing (Figure 19). Since the current through each wire is independent of those in the other two[18], a variety of traps can be created. If there is current in only one wire, a side guide is formed (its location and orientation depending on which wire is selected). If there are currents in both parallel wires, a two-wire guide [12, 28, 31, 32] results[19]; if there is current in only one parallel wire and in the perpendicular wire, an X-trap is formed. If there is current in all three wires, with copropogating currents in the parallel wires, the result is an IP trap; if the parallel wires bear counterpropagating currents, a quadrupole trap results[20]. Using differing currents in the legs allows moving the location of the minimum on the x axis. The remainder of this section will discuss the case of the IP trap[21].

If the currents in the parallel wires are copropagating, the resulting field is[22]

[18] In this work, we use identical currents in the parallel wires.
[19] In atom chip experiments, such a configuration can also be used to increase the longitudinal confinement for chip-generated fields; this is important, for example, in fragmentation experiments, as the chemical potential relies on the longitudinal frequency.
[20] In the latter case, it will be assumed that $I_y>0$ indicates the current in the leftmost wire (the one placed at –a) is in the positive y direction.
[21] The discussion here will be relatively brief, since most of the aspects have been covered in earlier sections.
[22] In this section, it is assumed that all three wires are long enough, relative to the location of the trap, to use the infinitely-long wire approximation

$$B_x = \frac{\mu_0 I_y z}{2\pi}\left(\frac{1}{(a+x)^2+z^2}+\frac{1}{(a-x)^2+z^2}\right)$$

$$B_y = -\frac{\mu_0 I_x z}{2\pi\left(y^2+z^2\right)} \qquad (2.1.42)$$

$$B_z = \frac{\mu_0}{2\pi}\left(\frac{I_x y}{\left(y^2+z^2\right)}+\frac{I_y(a-x)}{(a-x)^2+z^2}-\frac{I_y(a+x)}{(a+x)^2+z^2}\right)$$

In a similar fashion to the previously described traps, adding a bias field on the y axis will generate an IP trap, as shown in Figure 20.

Increasing the ratio of I_y/I_x increases the rotation of the field, as well as the angle of the IP field (relative to the x-axis). In addition, increasing I_y increases the longitudinal trap frequency while reducing the transverse frequencies (Figure 21).

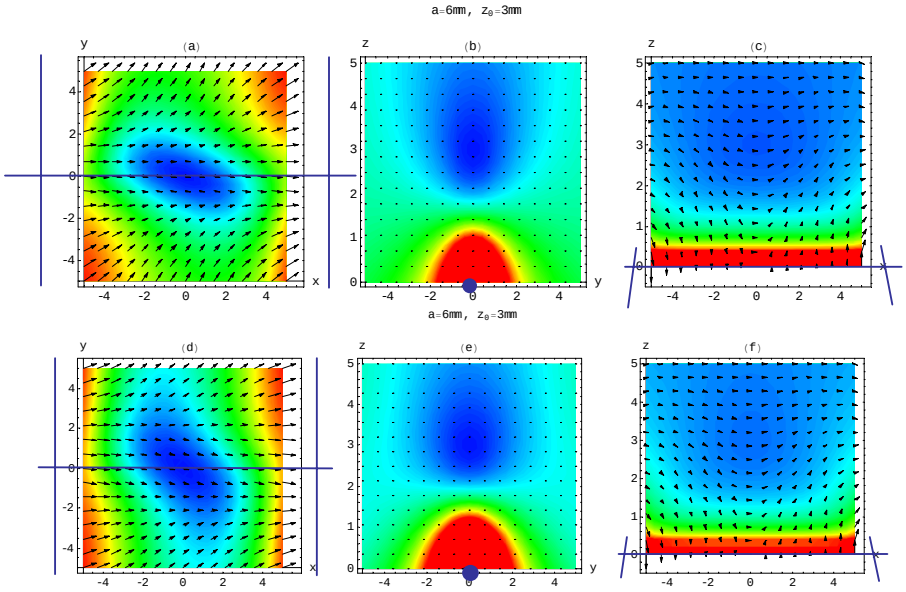

Figure 20 – Effect on the field of varying I_y (in the copropagating case). In the top row, I_x=I_y; in the second row, I_y is increased by 50%. The indigo lines indicate wire positions. Blue indicates low field, while red indicates high field.

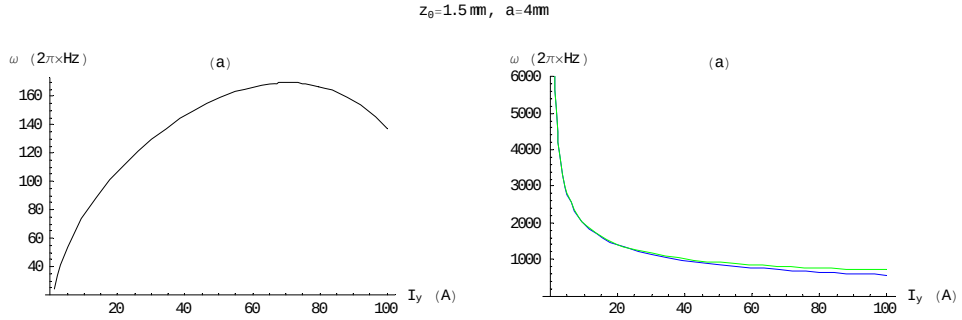

Figure 21 – Effect of altering I_y on the longitudinal (a) and transverse (b) trap frequencies. In (b), the green line indicates the transverse frequency in the xy plane, while the blue line indicates the frequency on the z axis. See text for more details.

It can be seen in Figure 21a that the longitudinal frequency has a maximum for a certain value of I_y. As the current increases past this point, the trap becomes more elongated (and the longitudinal axis becomes closely aligned with the y axis). It should also be noted that for $I_y=0$, the field is not harmonic at the minimum and thus the transverse frequency is not well defined for small I_y and therefore the plot of the transverse frequency (Figure 21b) goes to infinity for very small values of I_y.

Increasing I_y also reduces the trap depth. There is a certain point beyond which the field generated by the legs will overcome the confinement of the trap, destroying it.

While the H-trap described above is very versatile, actually using independent I_x and I_y currents requires the wires to avoid touching each other (it should be noted that if the wires are connected, it is possible to use the structure as a side guide or as a "standard" U- or Z-trap by changing which two of the six terminals are connected to source and ground). This may be accomplished in two different ways:

1) One possibility is simply to place the parallel wires above or below the crosspiece. This solution has the disadvantage that whichever wire(s) is selected to be in the plane farther from the trap will require a greater current to compensate for the added distance – since as the distance increases, the confinement decreases. The IP field depends on the angle between the plane in which the legs lie and a line from one of the legs to the minimum point; it is maximized when that angle is 45° (in other words, when the vertical distance between the legs and the minimum point equals half the distance between the legs). Therefore, the currents must also be modified to maintain the desired IP field. In addition, such a solution is more difficult to fabricate on a chip.
2) A second option is to effectively split each leg wire into two sections, as shown in Figure 22. This has the effect of lowering the confinement effect somewhat, both because the "middle" section of the legs is missing and because of fields produced by the parallel wire segments further from the center (which however, are smaller due to the additional distance). Again, this can be compensated for by slightly increasing the current. This configuration can be implemented on a single-layer chip.

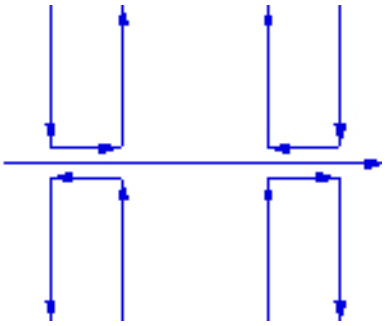

Figure 22 – Modified H-trap.

In Chapter 5 we will further discuss specific Z-, X-, and H-trap configurations.

2.1.4 Effects of gravity

So far, we have discussed magnetic trapping schemes without reference to any external forces. In the absence of such forces, the shape of the potential field and the location of its minimum are identical to that of the magnetic field, since they are linearly dependent on one another (equation (2.1.5)). However, in practice, the potential field is significantly affected by gravity.

The effect of the gravitational potential U_g modifies equation (2.1.5) so that the total potential experienced by an atom in the magnetic field is [33]

$$U = U_{BI} + U_g = mgz + g_F \cdot \mu_B \cdot m_F \cdot \left|\vec{B}\right| \qquad (2.1.43)$$

The actual trap center will be at the point where the force experienced by the atom is zero, or in other words, where the force imposed by the magnetic field is exactly countered by the gravitational pull. This will occur at the point at which the gradient equals (assuming $\hat{z}$ points away from the ground)

$$\nabla\left|\vec{B}\right| = -\frac{mg}{\mu}\hat{z} \qquad (2.1.44)$$

For example, for ^{87}Rb, the minimum will occur at the point at which the field gradient is equal to -1.52 G/mm.

If there is no point where equation (2.1.44) is true, a magnetic trap will not exist[23]. Generally, there is a point where the gradient is sufficiently large between the wire and the minimum; however, the chip – and thus the wire – are usually positioned *above* the minimum point. This is done for several reasons, chief of which is to facilitate time-of-flight [34-36] measurements without the atoms falling onto the chip surface. Therefore, the wire currents need to be selected to ensure a sufficient gradient exists below the minimum to prevent the

[23] In the case of a MOT, the gravity-counteracting force is generated by the lasers, so trapping can occur even with low field gradients.

atoms from dropping out of the trap. If a strong magnetic trap is required, the gradient must be correspondingly larger.

Obviously, the distance between the magnetic field minimum and the potential minimum is determined by the steepness of the trap. For steep traps (which are normally generated close to the wire, and/or by high currents and bias fields), the shift will be very small. In general, the closer the minimum is to the chip, the smaller the shift; when the minimum is several millimeters from the chip, the shift is typically on the order of tenths of a millimeter up to a millimeter at most.

Gravity also reduces the trap depth. In wire traps, for example, when gravity is ignored, the field magnitude (and thus the potential) asymptotically approaches a given value for large z, and the trap depth is the difference between that value and the trap's minimum value. When gravity is taken into account, the potential reaches a maximum at some point beyond the trap and then decreases monotonically; the trap depth is the difference between that maximum and the trap minimum. Since the effect of gravity on the potential is linear, the actual maximum is smaller than if gravity is neglected (Figure 23).

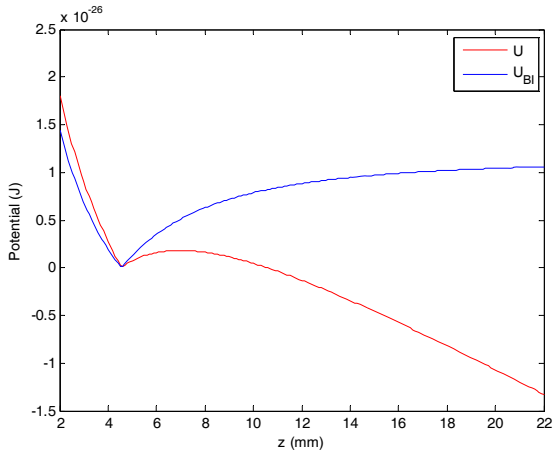

Figure 23 – Potential of a U-trap including (red line) and ignoring (blue line) gravity, where gravity is acting in the direction of increasing z. For this plot, the zero of the gravitational potential was set at the height of the trap minimum

2.2 Optical forces

Another option for cooling atoms is to use purely optical forces – that is, forces induced by light. This section will outline the principles behind one such type of cooling.

2.2.1 The scattering force

When an atom of mass m absorbs a photon whose frequency ν matches a resonance frequency of the atom, the photon's energy hν causes a transition to an excited state, while the

photon's momentum $\frac{h \cdot \nu}{c}$ is absorbed as an addition to the atom's momentum in the direction of the photon's movement (the converse is true for photon emission from an atom). The momentum exchange induces a force

$$\vec{F} = \frac{d\vec{p}}{dt} = \frac{h\nu\gamma_p}{c}\hat{A} \tag{2.1.45}$$

where γ_p is the atom's excitation (or scattering) rate (see below). In the case of absorption, the arbitrary direction vector $\hat{A}$ is the same as the laser's direction of propagation; in the case of photon emission, the vector's direction is opposite that of the emitted photon. The change in the atom's velocity after an absorption or emission event is of the magnitude

$$|\Delta v| = \frac{h \cdot \nu}{c \cdot m} \tag{2.1.46}$$

If we have a gas of atoms of mass m and temperature T in a volume (assuming the gas is dilute or otherwise approximates an ideal gas), their velocity is governed by the Maxwell-Boltzmann distribution

$$f(v) = 4\pi v^2 \left(\frac{m}{2\pi k_B T}\right)^{3/2} \cdot e^{-\frac{m \cdot v^2}{2k_B T}} \tag{2.1.47}$$

The characteristic velocity for the atoms at a given temperature is v_{rms}, given by

$$v_{rms} = \sqrt{\frac{3k_B T}{m}} \tag{2.1.48}$$

Let us consider an atom moving in a direction opposing the laser beam (for the moment, we will consider only the velocity component on the same axis as the beam). If it absorbs a photon, its velocity is reduced, since the direction of Δv is directly opposed to that of the atom's velocity v. As the atom shifts back to its ground state, it emits a photon, further changing its velocity; but as the probability of the direction of the emission is spatially symmetrical, the velocity change due to emission has a mean value of zero over multiple instances of photon absorptions, and the total deceleration of the atom is in the direction of the laser beam.

In order to allow absorption by the atom, ν must be equal to the atom's resonance frequency. There is, however, a complication; atoms moving in the same direction as the laser beam will also absorb photons, accelerating them. To prevent this, the laser frequency is slightly red-detuned from the atomic resonance[24]. From the view point of a moving atom, the frequency is Doppler shifted by

$$\omega_D = -\vec{k} \cdot \vec{v} \tag{2.1.49}$$

[24] That is, the frequency of the laser is reduced below the atoms' resonance frequency.

where $\vec{k}$ is the wavenumber vector whose magnitude is defined by

$$k = \left|\vec{k}\right| \equiv \frac{2\pi\nu}{c} \tag{2.1.50}$$

and whose direction matches that of the photons' direction of propagation. Thus, for atoms heading "into" the laser beam, ν is blue-shifted toward the resonance frequency, while for atoms moving "with" the beam, ν is red-shifted and therefore those atoms will not absorb photons.

The excitation (or scattering) rate γ_p depends on the laser's detuning from resonance (designated by δ), defined as the difference between the atomic resonance frequency ω_a and the laser frequency ω_L, and is given (for a two-level atom) by the Lorentzian [11]

$$\gamma_p = \frac{s_0\gamma}{2\left(1+s_0+\left(\frac{2(\delta+\omega_D)}{\gamma_d}\right)^2\right)} \tag{2.1.51}$$

where γ is an angular frequency corresponding to the excited state's rate of decay ($1/\tau$). The on-resonance saturation parameter s_0 is defined as the ratio between the light intensity I and the saturation intensity I_s (I/I_s); the latter is the intensity for which the atoms spend the minimum time in the unexcited state (or in other words, each atom is excited at the rate of once every τ seconds) and is given by

$$I_s \equiv \frac{\pi h\nu^3}{3\tau c^2} \tag{2.1.52}$$

I_s is dependent on the atoms in question, and is typically of the order of several mW/cm^2, an intensity easily achievable by suitable diode lasers (values of I_s for transitions of ^{87}Rb are given in Appendix C).

As the light intensity increases, so does the deceleration. However, at high intensities, the rate of stimulated emission also increases. Since, in the case of stimulated emission, the photon is emitted in the same direction as the laser beam's direction of propagation, the momentum "kick" is in the opposite direction, nullifying the deceleration caused by absorption. At these intensities, the atom has an equal chance of being in the excited or ground states, and the maximum deceleration is

$$a_{max} = \frac{h\nu\gamma_d}{2mc} \tag{2.1.53}$$

According to equation (2.1.49), $\Delta\nu \propto v$, so the Doppler shift becomes smaller as the atoms slow down, and eventually the shifted frequency will be too far from the resonance frequency to allow excitation. There are various methods to compensate for this effect [37]. The two most common ones are changing the laser's frequency as cooling progresses (known

as “chirping”), and spatially varying the resonance frequency by means of an inhomogeneous magnetic field (such as in a MOT, described later, or in a Zeeman slower [37-39]).

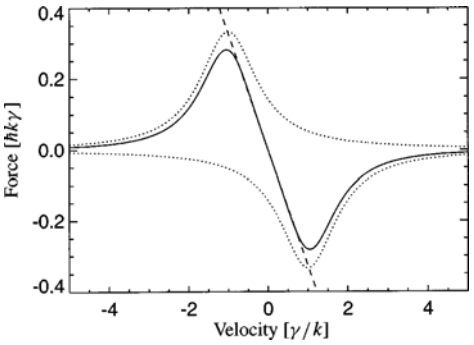

Figure 24 - Velocity dependence of the force in a 1-dimensional optical molasses. The dotted lines show the force of each laser (the top line is the force due to the laser propagating in the positive direction), while the solid line indicates the total force. It can be seen that near the origin, the force acts as a pure damping source (the dashed line). In this plot, s_0=2 and δ=-γ. [11]

With a pair of counterpropagating lasers, it is possible to use this optical force to slow atoms. The force acting on atoms in the beams is shown in Figure 24. The figure shows that atoms moving towards one of the laser beams are more likely to absorb photons from that beam (slowing them) than atoms moving away from it (speeding them up), since in their frame of reference the laser’s frequency is Doppler shifted away from resonance. Therefore, there is a net reduction of the ensemble momentum. The force resulting from the difference in the photon absorption rates for each laser can be regarded as a friction force because it is proportional to the atomic velocity, and the ensuing process is known as optical molasses. Using a system of six lasers, with each pair orthogonal to the other two pairs, it is possible to reduce the atom’s momentum in all three dimensions, thereby cooling them (3-D optical molasses) – this is known as Doppler cooling,

It is important to note that this method of three-dimensional momentum transfer does not create a trap for the atoms; it is precluded from doing so by the optical Earnshaw theorem [17].

A different scheme used for optically trapping atoms is based not on momentum transfer through the absorption and emission of photons, but rather on the energy shifts (Stark shifts) which the internal atomic hyperfine levels undergo in the presence of light. We will not describe these dipole traps here and refer the interested reader to [40].

2.3 Magneto-optical trapping

2.3.1 Basic concept

The most common method of trapping atoms is the magneto-optical trap (MOT). As its name suggests, this trap utilizes a combination of lasers and a magnetic field, the latter creating an additional – restoring – force that is necessary for trapping as well as cooling, as we now discuss.

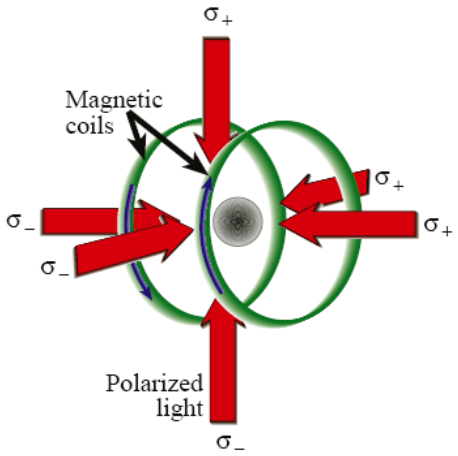

Figure 25 – Schematic of a MOT. Three pairs of counterpropagating laser beams (the red arrows) with opposite circular polarizations are aligned along mutually perpendicular axes; these decelerate atoms and trap them in the center of the trap (the grey sphere). The magnetic coils - which carry counterpropagating currents - provide the required quadrupole field. [41]

Figure 25 shows a schematic of a simple MOT. The coils create a quadrupole magnetic field, as described in section 2.1.1. This field splits the atom's energy levels into several sublevels (Zeeman splitting). For low magnetic fields (first-order Zeeman effect) the energy difference ΔE between the sublevels is linearly proportional to the field magnitude; thus, for a quadrupole field, $\Delta E=0$ at the trap center and increases linearly with distance (Figure 26c). Due to selection rules (arising from conservation of angular momentum), the σ^- beam induces $\Delta m=-1$ transitions, while the σ^+ beam induces $\Delta m=+1$ transitions (Figure 26b). Each laser is detuned by δ below the atomic resonance for zero magnetic field.

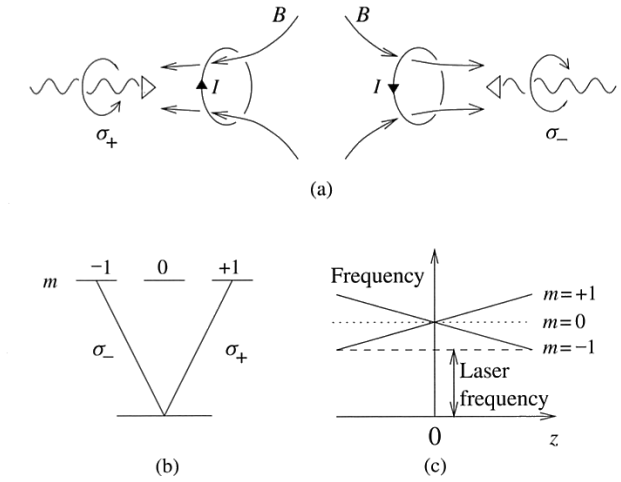

Figure 26 – (a) Schematic view of the magnetic field and laser beams in a MOT, shown only along the z-axis for clarity. (b) The transitions induced by each beam. (c) Influence of the magnetic field on the atomic sublevels (Zeeman shift) [42]

At the trap center (z=0), photons from each laser beam have equal probabilities of being absorbed by an atom. However, for z>0 the frequency of Δm=-1 transitions decreases, approaching the laser frequency, while the frequency of the Δm=+1 transition is tuned further from the laser frequency. Therefore, atoms for which z>0 have a higher probability of absorbing photons from the σ^- beam than photons from the σ^+ beam and conversely for z<0. The net force is therefore toward z=0 in both cases. Hence, atoms throughout the trap tend to move toward its center.

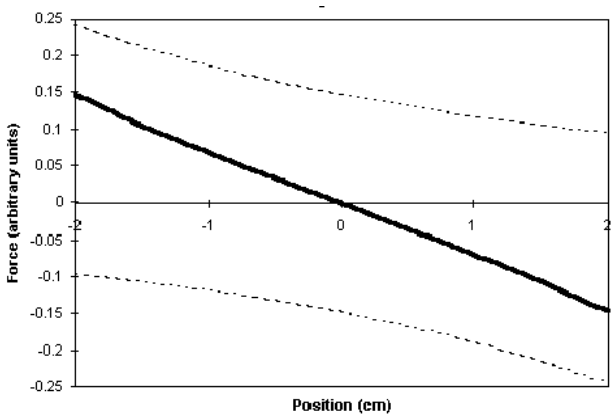

Figure 27 – Force operating on an immobile atom in a MOT. The dotted lines represent the force from a single laser, while the dark line is the net force. Taken from [43]

The force the atoms experience is given by $F=F_+ + F_-$ (representing the total force from both laser beams). The net force can be derived from equations (2.1.45) and (2.1.51), and, if the Doppler and Zeeman shifts are small relative to the detuning, is [11],

$$F = -\beta v - \kappa z \qquad (2.2.1)$$

where

$$\beta \equiv -\frac{2\hbar v^2 \delta s_0}{\pi^2 c^2 \gamma_D \left(1+s_0+\left(\frac{2\delta}{\gamma_D}\right)^2\right)^2} \qquad (2.2.2)$$

and κ is the equivalent of a spring constant. Thus, at a given moment (i.e. for constant v), the net force is linear, as shown by Figure 27.

This force results in damped harmonic motion of the atoms. The damping rate is

$$\Gamma_{MOT} = \frac{\beta}{m} \qquad (2.2.3)$$

while the oscillation frequency is

$$\omega_{MOT} = \sqrt{\kappa / m} \qquad (2.2.4)$$

For magnetic field gradients on the order of 10 G/cm, the oscillation frequency is typically smaller than the damping rate by several orders of magnitude, and consequently the atoms' motion is overdamped. The characteristic restoring time to the center of the trap ($2\Gamma_{MOT} / \omega_{MOT}^2$) is typically several milliseconds.

This description is simplified - in practice, MOTs are more complicated than described above. One problem is that most atoms have multiple hyperfine states. Since the laser does not match the resonances between all the levels, the population of excited atoms in non-resonant states may grow to the point that the MOT ceases to function. For example, the $3S_{1/2}$ ground state of sodium has hyperfine levels F=1,2, while the excited state $3P_{3/2}$ has hyperfine levels F'=0,1,2,3. If the laser frequency is resonant with the F=2→F'=3 transition, off-resonant excitation will cause a few atoms to be excited to F'=2, from which they can then decay either to F=2 or F=1. Since the laser does not match the resonance of the F=1→F'=2 transition, these atoms will accumulate in the F=1 sublevel and will not be subsequently excited, eventually depopulating the F=2 sublevel. This process can be described as unintentional "optical pumping" of the F=1 sublevel. Eventually, the number of atoms in the F=2 level (referred to as the bright state) will be sufficiently low that the MOT will cease functioning. To avoid this, an additional laser frequency resonant with the F=1→F'=2 transition is applied, thus depopulating the F=1 level in a process known as repumping [44, 45].

For evaporative cooling, which is required to achieve sufficiently low temperatures for a BEC, it is necessary to achieve a high density of atoms. However, the emission of photons from excited atoms creates a force which drives the atoms apart at high densities (since photons emitted by one atom are absorbed by another). In addition, at high densities, the atom cloud becomes opaque to the laser, preventing atoms in the cloud interior from being cooled.

One way to reduce the impact of these effects is to reduce the intensity of repumping radiation so that only a small proportion of the atoms are in a level where the laser beams can induce a transition. Although this reduces the effective force of the trap, the attainable density increases. One method [45] of doing so is directing repumping light preferentially to the outer portions of the cloud, causing atoms on the fringes to be driven inward, while atoms in the center will experience a high degree of optical pumping into a dark state, reducing the radiation forces in the interior. This configuration is known as a dark-spot MOT, and can achieve densities two orders of magnitude greater than a conventional MOT [42].

In a MOT[25] there occurs constant competition between the cooling induced by the MOT and the heating caused by each photon emission event. As the velocity of the atoms decreases, so does the differential cooling rate, and at some point it becomes small enough to be counteracted by the random momentum kicks imparted by the emissions. The temperature at which this occurs (known as the cooling limit or the Doppler temperature) is given by

$$T_D = \frac{\hbar \gamma_d}{2k_B} \qquad (2.2.5)$$

The value of this limit varies with the atoms involved, but is usually well below 1 mK; for example, T_D for sodium is approximately 240 μK [36] and 141 μK for rubidium [46].

In 1988, it was discovered that the temperature of Doppler-cooled atoms was well below the Doppler limit [36][26]. This is caused by the inhomogeneity of the light field as a result of the opposing lasers' polarization and by the effects of the atomic hyperfine levels (such as those caused by Zeeman shifts).

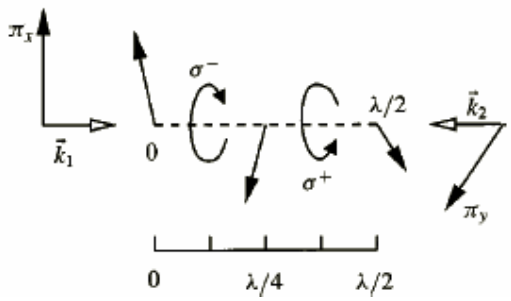

Figure 28 – Polarization of the superposed field of two counterpropagating and perpendicularly polarized lasers. The field has a minimum at 0, a maximum at λ/8, and both maxima and minima have a sinusoidal periodicity of λ/8. [11]

If the lasers are linearly polarized perpendicular to one another, the total electric field potential's magnitude varies sinusoidally along the lasers' axis of propagation. Due to the light shifts, each of the ground state sublevels (e.g. m=±1/2) has a maximum at the other

[25] This applies to optical molasses as well.
[26] The article refers to atoms cooled in an atom molasses, but the same phenomenon occurs in a MOT.

sublevel's minimum, and *vice versa*. The electric field's polarization also varies, from linear at the minima to circular at the maxima, with alternating directions (Figure 28).

This mechanism depends on the fact that optical pumping between two sublevels takes a finite and nonzero amount of time. If an atom begins in a potential "valley" (say at the sublevel m=1/2), it can move a certain distance, climbing the potential "hill". When it reaches the maximum, the light is now polarized in the σ^- direction, optically pumping the atom to the m=-1/2 sublevel. The potential difference between the levels is emitted as a photon in the transition. The atom is now at the minimum for the m=-1/2 sublevel, and climbs the potential to the next maximum, where the polarization is now σ^+, inducing a transition to m=1/2 (Figure 29). In such a fashion, the atom continues to climb potential "hills" without ever descending them, translating its kinetic energy into potential energy [47]. The process repeats until the kinetic energy is too small to climb the next "hill". This cooling mechanism is known as Sisyphus cooling, after the mythological Greek figure who was condemned to eternally roll a boulder up a hill. Through this mechanism, very low temperatures can be reached (e.g. 35 μK for sodium).

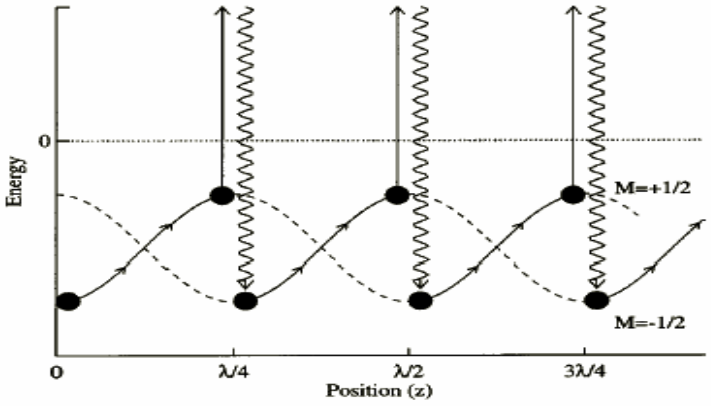

Figure 29 – Sisyphus cooling of an atom. The atom moves up a potential "hill", and as it approaches the crest, it is pumped into the next "valley". As the repeats, the atom loses more and more kinetic energy [11]

In the case that the lasers are circularly polarized, the resulting electric field is linearly polarized everywhere and of constant magnitude, but the polarization's orientation rotates through an angle of 2π over one wavelength. In this case, an effect similar to the force in a MOT (described above) occurs. The m=1 sublevel (with m being the magnetic quantum number) will have a higher population for atoms moving in the positive direction [37], while in atoms moving in the negative direction the m=-1 sublevel will have a greater population. Because of the different Clebsch-Gordan coefficients involved in the various transitions [37], the m=1 sublevel scatters photons from the σ^+ beam at an efficiency six times greater than σ^- photons. Therefore, atoms moving against the σ^+ beam scatter more of its photons and experience a greater momentum shift in the negative direction, while atoms moving in the

negative direction are preferentially pumped to the m=-1 sublevel and recoil in the positive direction. Though difficult to quantify, the final cooling derived from this mechanism is on the same order as for Sisyphus cooling [47] .

In all the methods involved, there is constant absorption and emission of photons by the atoms. That sets a lower temperature limit due to the fact that each time an atom emits a photon, it receives a "kick" in some direction. At low temperatures, the velocity changed caused by emission is of the same order as the atom's total velocity, and thus the atom cannot be cooled further. This limit, known as the recoil limit, is given by [37]

$$T_r = \frac{\hbar^2 k^2}{k_B m} \qquad (2.2.6)$$

While purely optical methods have been developed to cool atoms beneath this limit, description of those methods is beyond the scope of this paper (further material can be found in [48]). More commonly, purely magnetic means allowing for very effective cooling through evaporative cooling are used instead (see for example [3, 20, 21, 37, 42]).

2.3.2 Mirror MOT

As mentioned in section 2.1.3, it is desirable to reduce the size of the field-generating wires; in our case, they are placed on a microchip. However, the small volume of a chip trap entails certain drawbacks. Its small size presents difficulties in loading the atoms into the trap. In addition, the proximity of the trap to the substrate on which the field-generating wire resides presents difficulties when implementing the six-laser MOT described above, since the laser must be positioned between the substrate and the trapping area (otherwise, the substrate blocks the beam). One solution [49, 50] for this problem is a mirror MOT (Figure 30).

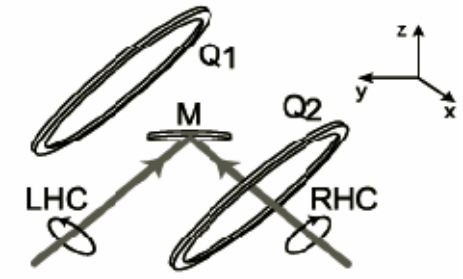

Figure 30 – Schematic view of a mirror MOT (the two beams perpendicular to the page and parallel to the mirror are not shown). [49]

This type of MOT uses four laser beams instead of six. Two of the beams strike a mirror at a 45º angle and are reflected back along each other's paths. The beams are perpendicular to

each other. The other two laser beams are counterpropagating and are both parallel to the mirror surface and perpendicular to the plane in which the first beams lie. There is a region close to the mirror where all four beams intersect. When the beams are reflected, their helicity (circular polarization, or the projection of the angular momentum in the direction of the momentum) is inverted, and thus at the region where all the beams intersect there are effectively three orthogonal pairs of beams, with each (incoming) beam having an opposite helicity compared to its counterpropagating (reflected) counterpart (this can be visualized by rotating the system in Figure 25 by 45º and regarding the two reflected beams as additional counterpropagating beams). Therefore, atoms in this region see fields identical to those in a six-beam MOT.

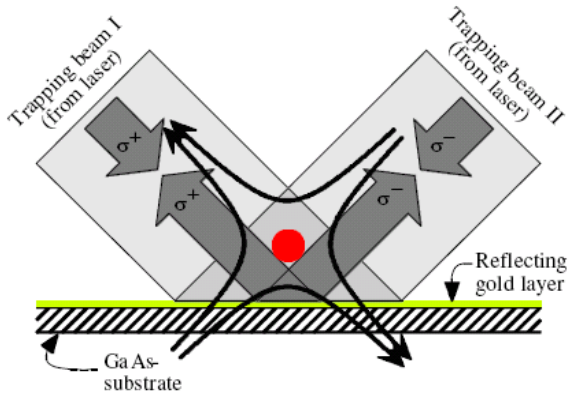

Figure 31 – Path of the lasers in a mirror MOT (there are two additional beams, not indicated here, perpendicular to the page). Note that while in Figure 25 the counterpropagating beams have opposite circular polarization, in this figure they have identical circular polarization. This is simply due to a different notation in their respective sources: in Figure 25 the circular polarization is defined relative to one global quantum axis (and this is the notation used in the text), while here the polarization is defined relative to the propagation direction of the photon. [51]

It should be noted that other types of mirror MOTs exist; some examples can be seen in [52].

For a mirror MOT to be established, several conditions must be met. First, the minimum of the quadrupole magnetic field must be located in the intersection region of the four beams.

The second consideration is the alignment of the magnetic field lines relative to the laser beams. Because the helicity of the photons is reversed, the field lines (at least in the vicinity of the trap) must be parallel to the reflected laser beams [8]. Namely, unlike in the 6-beam MOT, here the quadrupole axis needs to be at a 45º angle to the mirror surface. This will be discussed to a greater extent in section 3.1.4.

3 Design of a U-MOT

So far, we have discussed the basic principles of wire traps and a mirror MOT. In our laboratory, we have constructed experiments to realize and utilize these principles to trap atoms.

In experiments of this type, hot atoms are emitted from an oven or dispenser and trapped and cooled by a MOT. In our particular configuration, in order to avoid the necessity of large coils to create a quadrupole field, we use a U-shaped wire to closely approximate a coil-generated quadrupole field (this type of MOT is known as a U-MOT). In conjunction with the laser fields, this wire produces a trap whose center is 4-6mm from the atom chip's surface. After cooling in the MOT, the atoms are cooled further in an optical molasses (magnetic fields are not used in this stage), and then the lasers are turned off for the rest of the experiment (with the exception of imaging). For the subsequent evaporative cooling, the atom must be transferred to a magnetic trap with a nonzero minimum (an IP trap) which can be generated by several different wire configurations (such as Z-, H- or X-wires). After creating the BEC at a distance of several hundred microns from the surface, this magnetic trap is also used to move the condensate closer to the atom chip's surface, where other physics experiments may be carried out.

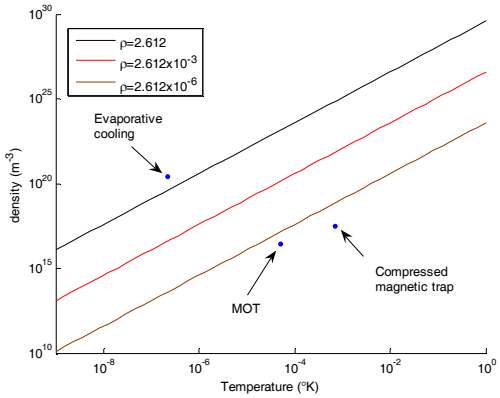

Figure 32 – Temperatures and densities obtained at several phases of a typical BEC experiment. The dots indicate the temperature and density at the end of each stage, while the lines indicate various values of phase space density ρ [37] – a minimum PSD of 2.612 is necessary for achieving BEC. The data for this particular plot was taken from [53]; see that reference for further detail.

I begin this chapter by discussing some of the considerations which must be taken into account when translating the principles described in Chapter 2 to the laboratory. I then describe and discuss the actual system we constructed to create a U-MOT, and present some of the results that were obtained using it.

3.1 Practical considerations for trapping schemes

3.1.1 Finite size effects

Up to this point, it has been assumed that the wires are one-dimensional. In practice, the wires have width and height as well as length, which significantly affect the field[27].

The field generated by an infinitely long wire lying on the x-axis (with current flowing in the positive-x direction), with width L_y and thickness (height in the z axis) L_z, is[28]

$$B_y(y,z,L_y,L_z)=\frac{\mu_0 I}{8\pi L_y L_z}\left(\begin{array}{l}2Z_-\left(\tan^{-1}\frac{Y_-}{Z_-}+\tan^{-1}\frac{Y_+}{Z_-}\right)-2Z_+\left(\tan^{-1}\frac{Y_-}{Z_+}+\tan^{-1}\frac{Y_+}{Z_+}\right)\\ +Y_-\ln\frac{Y_-^2+Z_-^2}{Y_-^2+Z_+^2}+Y_+\ln\frac{Y_+^2+Z_-^2}{Y_+^2+Z_+^2}\end{array}\right)$$

$$B_z(y,z,L_y,L_z)=\frac{\mu_0 I}{8\pi L_y L_z}\left(\begin{array}{l}2Y_+\left(\tan^{-1}\frac{Z_-}{Y_+}+\tan^{-1}\frac{Z_+}{Y_+}\right)-2Y_-\left(\tan^{-1}\frac{Z_-}{Y_-}+\tan^{-1}\frac{Z_+}{Y_-}\right)\\ -Z_-\ln\frac{Y_-^2+Z_-^2}{Y_+^2+Z_-^2}-Z_+\ln\frac{Y_-^2+Z_+^2}{Y_+^2+Z_+^2}\end{array}\right) \quad (3.1.1)$$

where

$$Y_\pm \equiv L_y \pm 2y$$
$$Z_\pm \equiv L_z \pm 2z$$

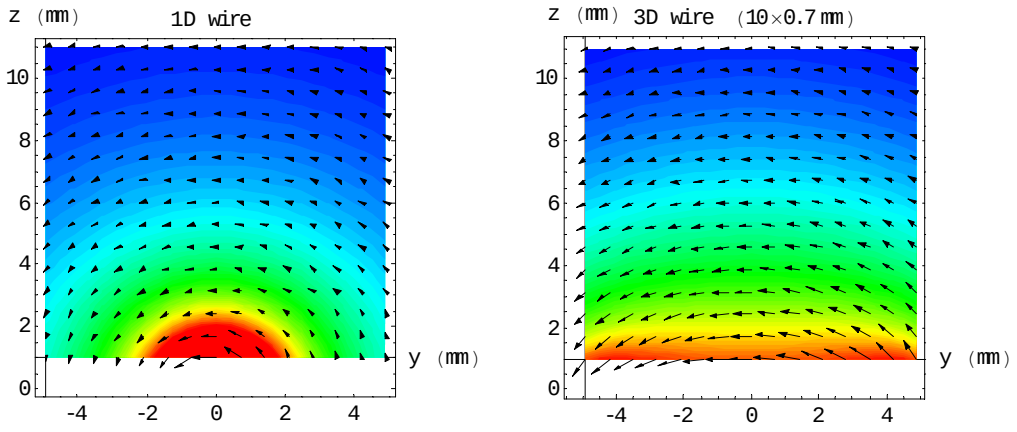

Figure 33 – Plot of the field of a one dimensional wire (left) vs. a thick wire (right), both perpendicular to the page. The thick wire is 10mm wide in the y direction and 0.7mm thick in the z direction, and is centered at (y,z)=(0,0). Violets and blues indicate high fields.

[27] One-dimensional wires are referred to in this text as 1-D wires, while wires also having height and width are referred to as 3-D wires.
[28] See Appendix B.

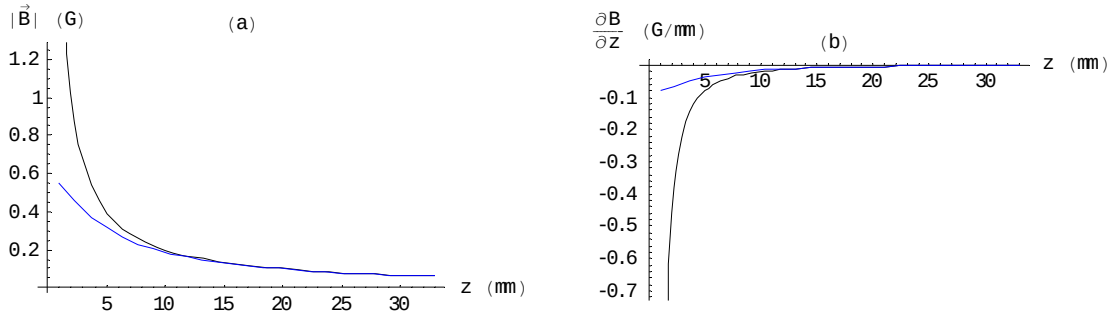

Figure 34 – Comparison of the field magnitudes (a) and z-axis gradients (b) of the fields of a 1-D (black line) and 3-D (blue line) wire, over the wire center (for I=1A)

The behavior of the magnetic field of a 1-D and 3-D wire are compared in Figure 33 and Figure 34. It can be seen that the field magnitude and gradient over the center of a wide wire are smaller than for a one-dimensional wire; however, they are indistinguishable at large distances from the wire. As can be expected, the smaller the value of L_y, the closer to the wire this convergence occurs. A similar (though smaller in magnitude) trend occurs for decreasing values of L_z.

Consequently, for traps close to the wire, thinner wires will create narrower and deeper traps, with significantly higher trapping frequencies, gradients, and depths than thicker wires. The problem is especially significant in the case of an H-trap with legs and crosspiece in different planes, as thicker wires mean the distance between the two planes must be larger. Because of this, thinner wires are generally preferable for magnetic trapping, particularly in the vicinity of the wire, since they produce significantly higher fields and field gradients. However, thick wires have compensating advantages; the thicker the wire, the less heat is produced by resistive heating during the trap's operation; thick wires also have advantages in magneto-optical trapping applications (see the discussion of the U-wire in section 3.1.4).

3.1.2 Current leads

One consideration which must be taken into account regards the effect of the wires which carry current to the trapping wires. In the examples given in Chapter 2, the wires through which current passes – the "legs" (and the crosspiece, in the case of the H- and X-traps) – are assumed to be infinite in length. In practice, of course, they have finite length, and are connected at their termini to other leads, which are in turn connected to the current source (or to yet other leads). In our applications, the leads in question are perpendicular to the chip surface.

The currents running through these leads generate their own magnetic fields. On an atom chip, these additional fields are usually negligible, since the distance from the trapping region to the leads is much larger than the height of the trapping region above the chip. However, these effects can be significant when discussing traps made of larger wires.

As an example, let us look at a U-trap and a Z-trap. Each of them has leads as shown in Figure 35. The locations of the leads were chosen to be similar to those used in our actual experiment. In both cases, the trapping wires lie in the z=0 plane. We will assume that the leads are long enough so that they can be assumed to extend to negative infinity.

a) b)

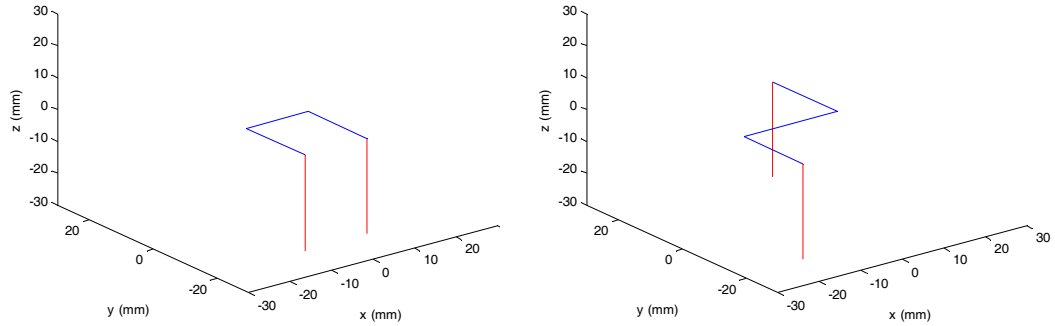

Figure 35 – U- and Z-wires (blue lines) with leads (red lines)

We will look at the field generated only by the leads at the point directly above the center of the wire. For the U-trap, the z-axis component of the field there is zero, and in the x=0 plane, the x-axis component is zero as well. For the Z-trap, the field at the center is perpendicular to a straight line from the xy location of one lead to the xy location of the other, and its x-component opposes the x-component of the field from the Z wire (thus decreasing the trap depth).

The resulting field is shown in Figure 36. The field generated by the leads is quite small; however, it must be remembered that the field is linearly proportional to the current, and as the current increases, so does the effect of these additional fields.

In practice, it is often difficult to accurately model and simulate the effects of leads much longer than the trap wires, due to computer limitations of speed and memory, in particular when the wire is being simulated in three dimensions (see section 3.1.1). Figure 37 shows the ratio between the fields generated by half-infinite leads and by leads of length L. For most simulations, L=40mm was considered sufficiently long for good accuracy. The

discrepancy in results between L=40mm and L=∞ increases with the distance from the wire, but is generally small for typical wire parameters; for example, the effect on the depth of a U-trap is on the order of 1% difference until large (~15mm) distances from the wire are reached.

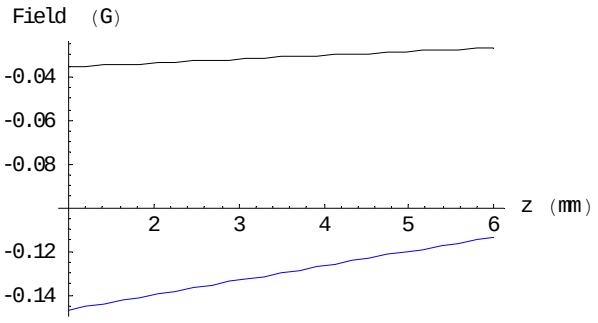

Figure 36 – The y-axis field caused by half-infinite leads to a U-trap (black line) and the x-axis field caused by half-infinite leads to a Z-trap (blue line), for I=1A. z designates the distance from the wire.

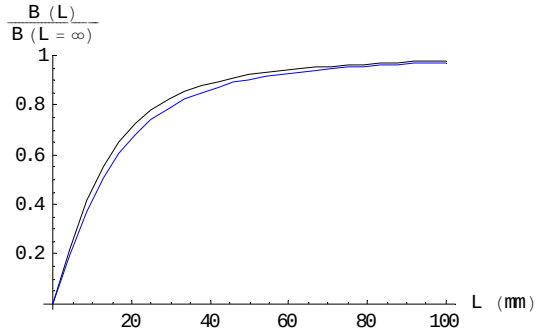

Figure 37 – Ratio between field of half-infinite leads and leads of length L. The black line indicates the y component of the U-trap leads, while the blue line indicates the x component of the Z-trap leads

An alternative solution is to model the lead wires as infinitely thin. The fields of such wires are generally simple to calculate quickly, and the field is modeled more accurately, especially if the lead is circular in profile (since in that case, as per Ampère's Law, it behaves like an infinitely thin wire at any point outside its radius). However, doing this has the drawback that the changes in current direction at the point where the leads meet the legs are not properly modeled. Whether this is significant or not depends on the system and on the location at which the field is evaluated. In the systems discussed in this work, we can ignore these particular changes in current direction.

3.1.3 Current density variations

In a three-dimensional wire, the current density is not necessarily uniform at all points in the wire, as can be seen in Figure 38. It varies when the wire deviates from a straight line (especially at corners) or contacts another wire. These changes in current density and direction may set up fields in varying directions, which may affect the experiment. In the case of the Z-wire, it can be seen that not only does the current density change at bends of the wire,

but that the current is actually not aligned with the axis of the crosspiece. Therefore, an additional bias field may be required to counteract the field generated by both the current direction change in the bends and this twist of the crosspiece current. The significance of these current density variations decrease if the legs are further apart (moving the bends further away, and reducing the twist in the field) or at small distances from the wire.

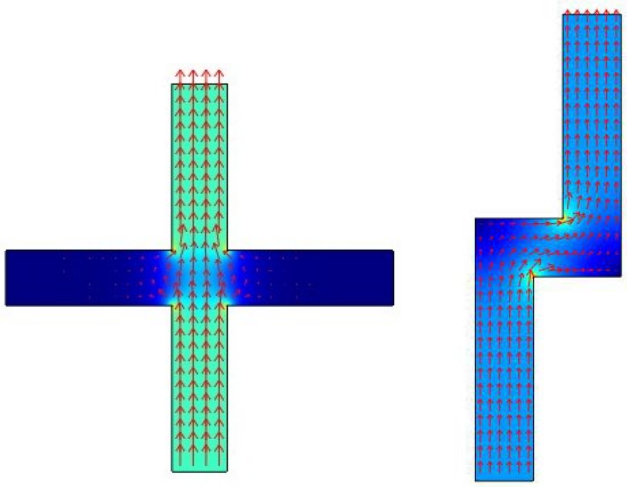

Figure 38 – Current density and flow in a wire cross and in a Z-shaped wire. Darker colors indicate lower current density. The red lines or arrows indicate the direction of current flow.

3.1.4 Field line orientations for a mirror MOT

As discussed in section 2.3.2, one of the requirements for a mirror MOT is that the field lines in the vicinity of the trap be aligned with the directions of the reflected laser beams. This is the case in an ideal quadrupole - the field vectors around the minimum are perpendicular to each other (Figure 39). If the field lines are not aligned with the beams, there will occur a mixing of the interactions – the "deviating" laser will interact with atoms moving in *both* directions, weakening the trapping force. It has been calculated [5] that the maximum acceptable deviation in a U-MOT is 40º. Fields generated by wire traps, however, only approximate a quadrupole – the alignment is imperfect, and tends to become more so as the distance from the minimum grows. This section will first discuss the deviations in the field generated by a side guide (2D quadrupoles) as an example of a simple case, and then deviations in the U-trap. The purpose of these calculations is to optimize the design of the U-wire in terms of the shape of the quadrupole field it produces for the MOT stage of the experiment. In particular, we seek an optimum design for the separation between the "legs" of the U-wire and also the width of its cross-piece wire section.

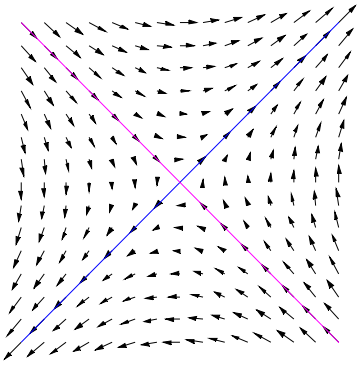

Figure 39 – Vector plot of an ideal quadrupole field. The field vectors around the minimum are oriented along straight lines at 90° to one another (along the blue and purple lines).

As can be seen in Figure 40, a side guide's field deviates considerably from the orientation of an ideal quadrupole field.

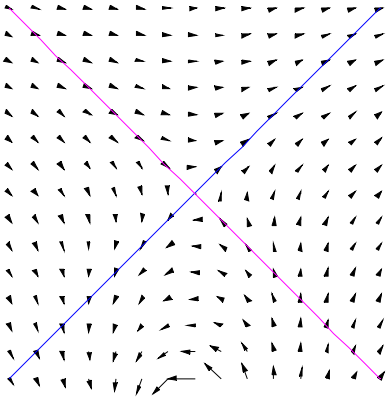

Figure 40 – Vector field plot of a side guide's field (in the x=0 plane). The colored lines designate the field vector orientations of an ideal quadrupole field. In this example, the minimum is at (y=0, z=12)

Analytically, the angle θ_B of the field at a point is expressed by

$$\theta_B = \tan^{-1}\left(\frac{\vec{B}\cdot\hat{X}_{|}}{\vec{B}\cdot\hat{X}_{-}}\right) \tag{3.1.2}$$

where X_- and $X_|$ respectively designate the horizontal and vertical axes of the plot. In this case, by definition, $X_-=y$ and $X_|=z$ and therefore the deviation in the case of a side guide is

$$\theta_B^{SG}(y,z) = \tan^{-1}\left(\frac{\mu_0 I\cdot y}{2\pi B_{0y}\left(y^2+z^2\right)-\mu_0 I\cdot z}\right) \tag{3.1.3}$$

Along the blue and purple lines in Figure 40, θ_B becomes

$$\theta_B^{blue}(y) = \tan^{-1}\left(\frac{z_0}{2y+z_0}\right)$$
$$\theta_B^{purple}(y) = \tan^{-1}\left(\frac{z_0}{2y-z_0}\right) \tag{3.1.4}$$

The deviation from the ideal quadrupole field is shown in Figure 41 (the deviations at a fixed point) and Figure 42 (mean deviations from the ideal for minima at various locations). These figures show the deviations at the various quadrants surrounding the minimum point. For example, when measuring the deviation in the upper left quadrant[29], the field of the side guide is measured at points along the line (the purple one, in this case) shown in Figure 40, starting at the minimum point and proceeding in the negative-x, positive y direction. The deviation is the difference between the field direction at each point and the direction of the field which would result from an ideal quadrupole field (with the minimum of both fields at the same location). Typically, as the deviation in one quadrant decreases, that in another quadrant increases. It can also be seen that, for the side guide, there is a symmetry to the deviations around the y axis.

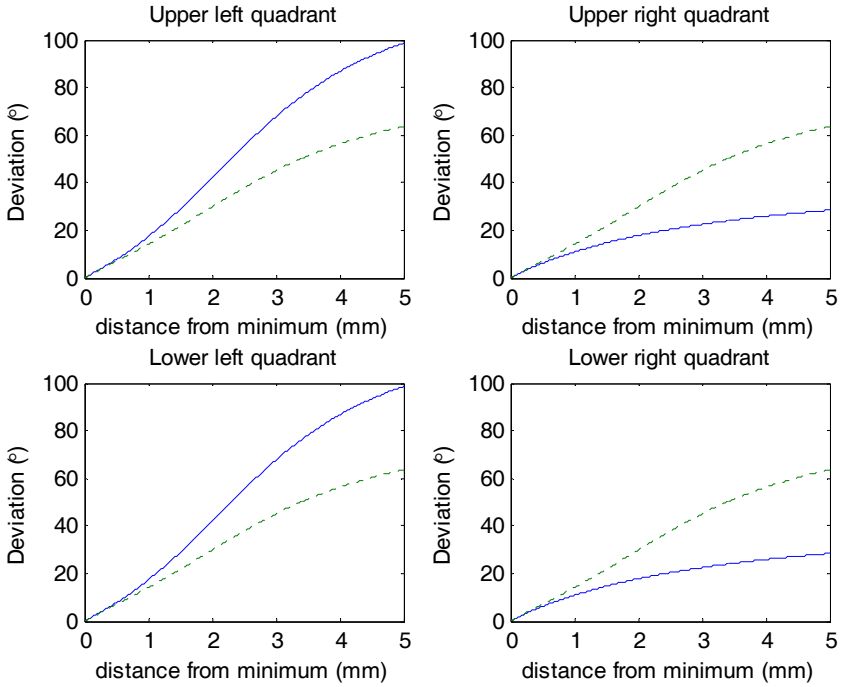

Figure 41 – Deviation of the field of a side guide from field of an ideal quadrupole. The solid line indicates the deviation calculated at points along the purple and blue lines from Figure 40 in the relevant quadrant. The dashed line indicates the mean deviation for all four quadrants. The minimum in this case is at (y=0,z=3)[30].

[29] To clarify, the quadrants may be described as follows – if we imagine a coordinate system shifted so that the origin is at the minimum point, the upper right quadrant is the 1st quadrant, the upper left quadrant is the 2nd quadrant, and so on.

[30] This particular location was chosen for ease of comparison with the case of the U-trap.

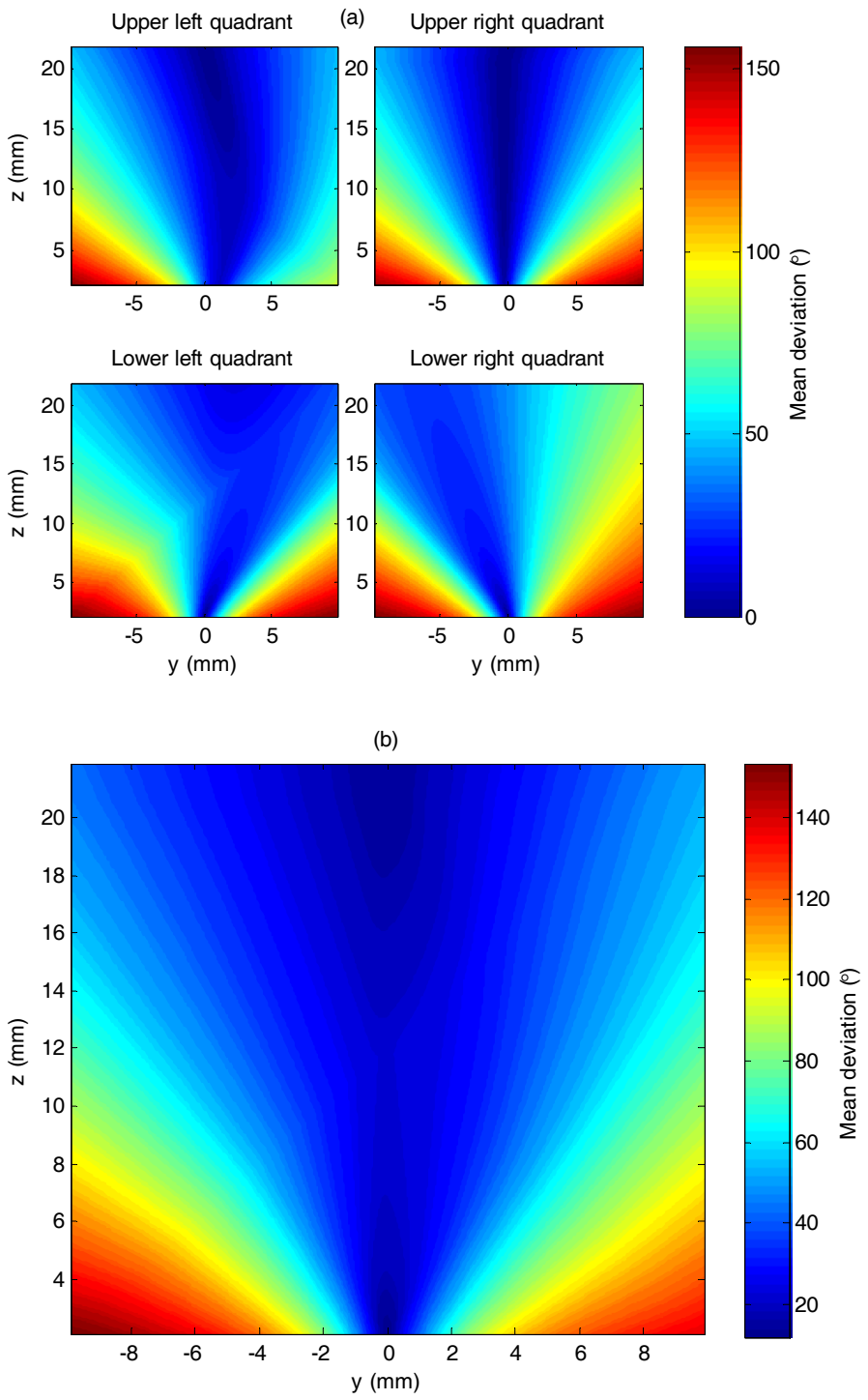

Figure 42 – Mean deviation for various minimum locations for the side guide. The color in the contour graphs in (a) indicate the deviation, averaged over a distance r (2mm in this case) from the minimum, between the direction of the side guide field and that of an ideal quadrupole field, for minima at various locations in the yz plane. Plot (b) shows the averaged deviation for all four quadrants. See text for more details.

While Figure 41 shows the deviations at various distances from the minimum, Figure 42 shows the mean of the deviations for each quadrant. Figure 42a shows the mean deviation in each location for each quadrant. Basically, for each (y,z) coordinate, the four graphs in Figure

41 were calculated. Then, the values for each quadrant (up to a specified distance from the minimum, 2mm in this case) were averaged; the resulting values are the mean deviation of the field, in each quadrant, when the minimum is at the chosen (y,z) coordinate. The process was repeated for all the coordinates (in the ranges -10<y<10, 2<z<22), and the results plotted as contour graphs (where the z axis – the color - of the graph is the mean deviation at that point). Figure 42b shows the average of the values for all four contour graphs (the mean of the means, as it were).

a)

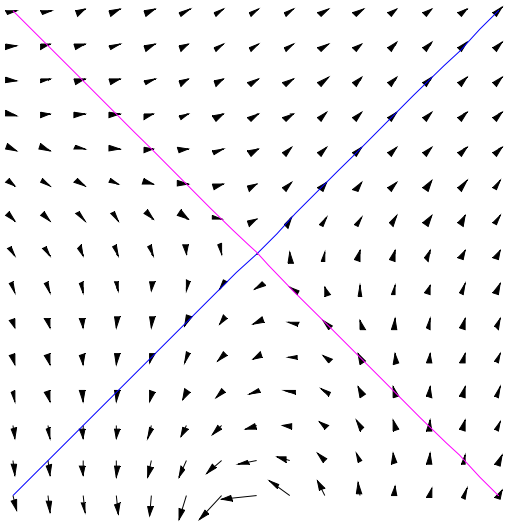

b)

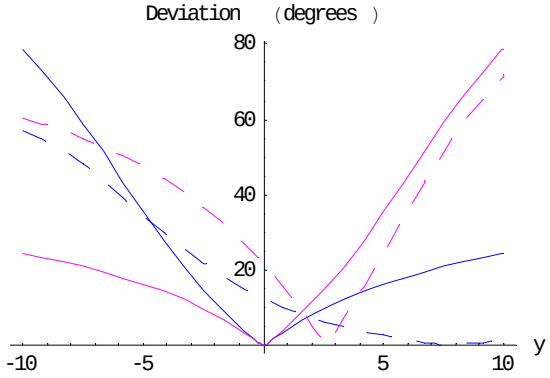

Figure 43 – Vector field plot of a U-trap's field (in the x=0 plane). The colored lines designate the field vector orientations of an ideal quadrupole field. In this example, the minimum is at (y=0, z=12), and the separation between the "legs" is 10mm. The lower graph (b) is a comparison with the deviation in a side guide; the solid lines represent the side guide, while the dashed lines represent the U. The color indicates the line in (a) along which the deviation is calculated. The minimum in both cases is set at the same location, with the same current. It can be seen, for example, that for the U-trap, the field in the upper right quadrant is closer to an ideal quadrupole than that of a side guide, while the opposite holds in the upper left quadrant.

In the case of a U-trap (Figure 43, Figure 44 and Figure 45), the situation is more complicated. As with the side guide, the field vector directions deviate from those of an ideal field. However, in the case of a U-trap, an additional parameter influences the degree of deviation – the separation between the U's two "legs" (and thus the length of its crosspiece).

As can be seen from a comparison of Figure 42 and Figure 45, the averaged deviation values for various locations of the U-trap are similar to those for the side guide, except that

they are tilted away from the U's "legs". Consequently, for larger values of z, creating a trap with minimal deviation requires the trap location to be displaced from locations directly over the U's crosspiece.

As noted above, the deviation also depends on the separation between the U's "legs". The optimal size depends on the location of the minimum; two examples are given in Figure 46. Figure 47 shows the separation required for an optimal deviation at several points.

In addition to proper selection of the minimum location and the separation of the legs, it is often possible to reduce the deviation by angling the bias field in the yz plane, so that it is not parallel to the y axis [8]. Another method to decrease the degree of deviation in the U-trap is to use a thick (in the z direction), broadened (in the y direction) crosspiece, as seen in Figure 48.

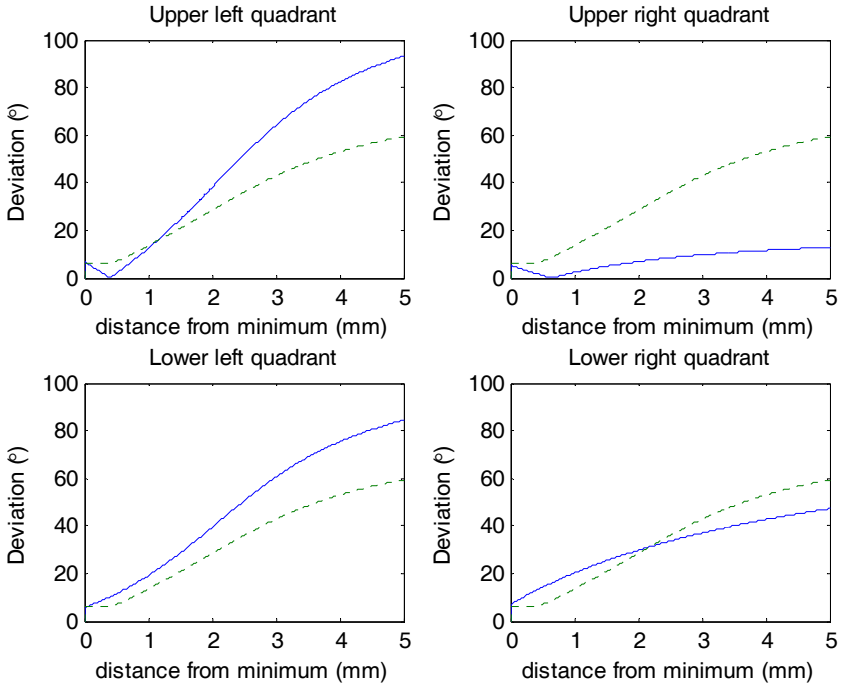

Figure 44 – Deviation of the field of a U-trap from the field of an ideal quadrupole. The solid line indicates the deviation calculated at points along the red and blue lines from Figure 43 in the relevant quadrant. The dashed line indicates the mean deviation for all four quadrants. The minimum in this case is at (y=0,z=3).

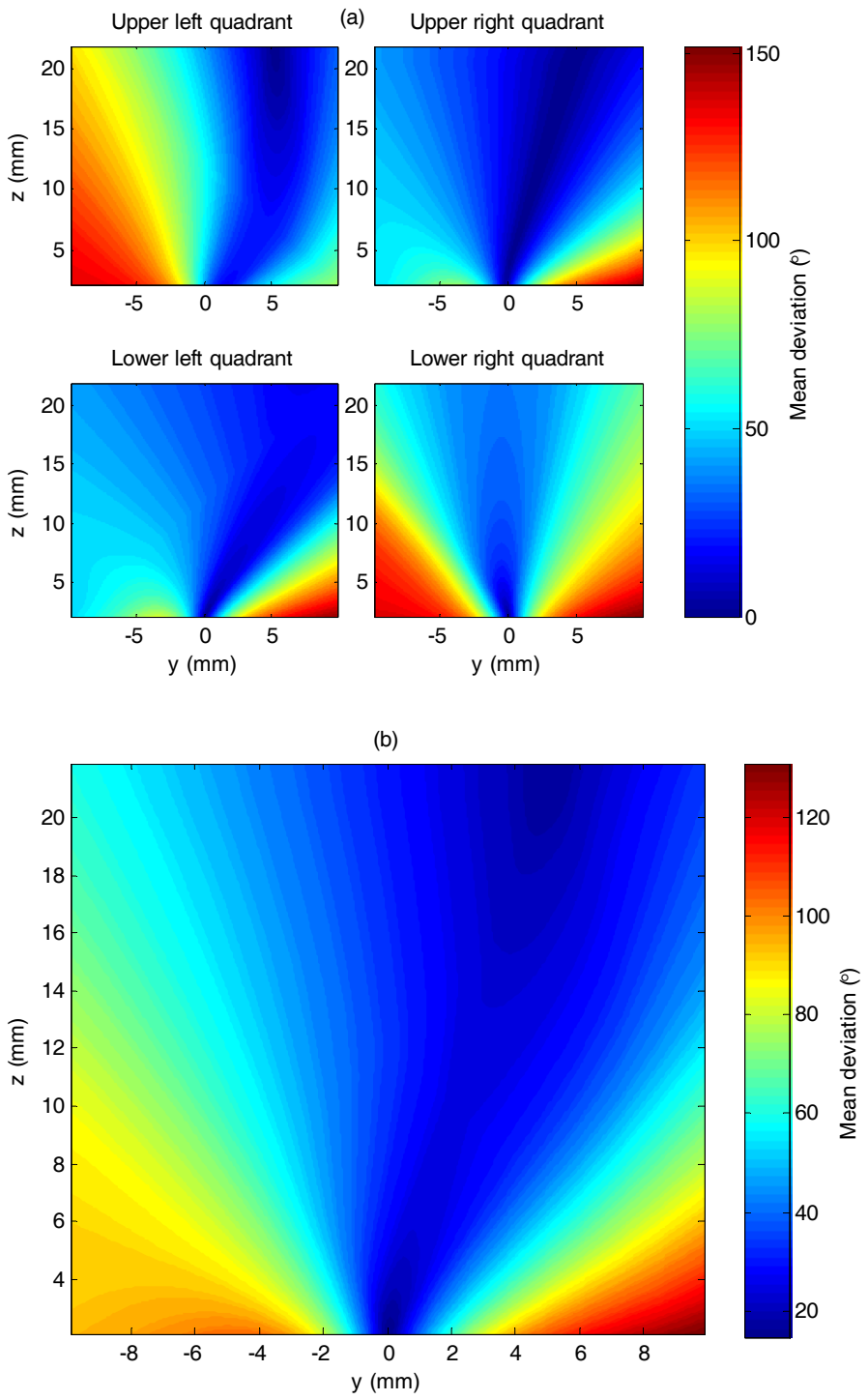

Figure 45 – Mean deviation for various minimum locations for the side guide. The color in the contour graphs in (a) indicate the deviation, averaged over a distance r (2mm in this case) from the minimum, between the direction of the side guide field and that of an ideal quadrupole field, for minima at various locations in the yz plane. Plot (b) shows the averaged deviation for all four quadrants. See the text for Figure 42 for more details.

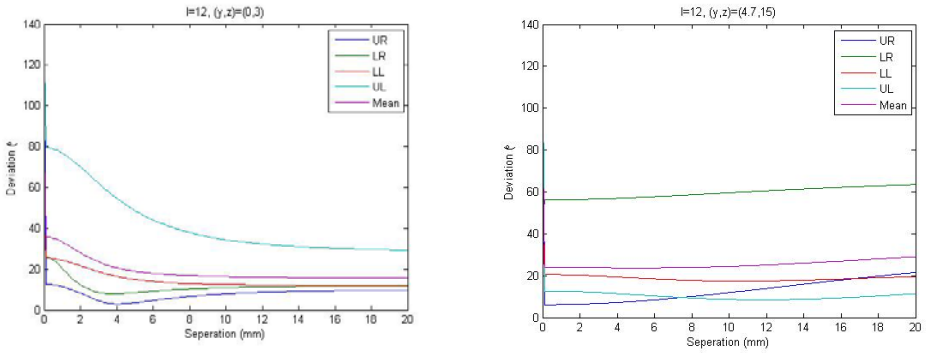

Figure 46 – Deviation as a function of separation of the U's legs at two specific locations. UR indicates the upper right quadrant, LL the lower left, and so on. It can be seen that each example has a different optimal value of separation.

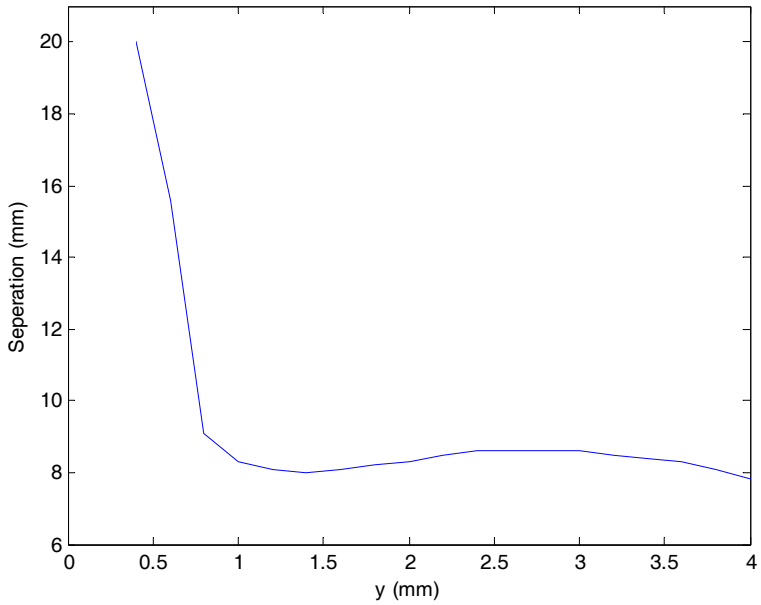

Figure 47 – Optimal separation of a U-wire's legs as a function of minimum location. The optimal point is assumed to be at the point where the mean deviation is minimal; the coordinates of the minimum are (y,z)=(y,3y+3). This relationship was chosen to keep the selected points within an area of small deviations (as seen in Figure 45)

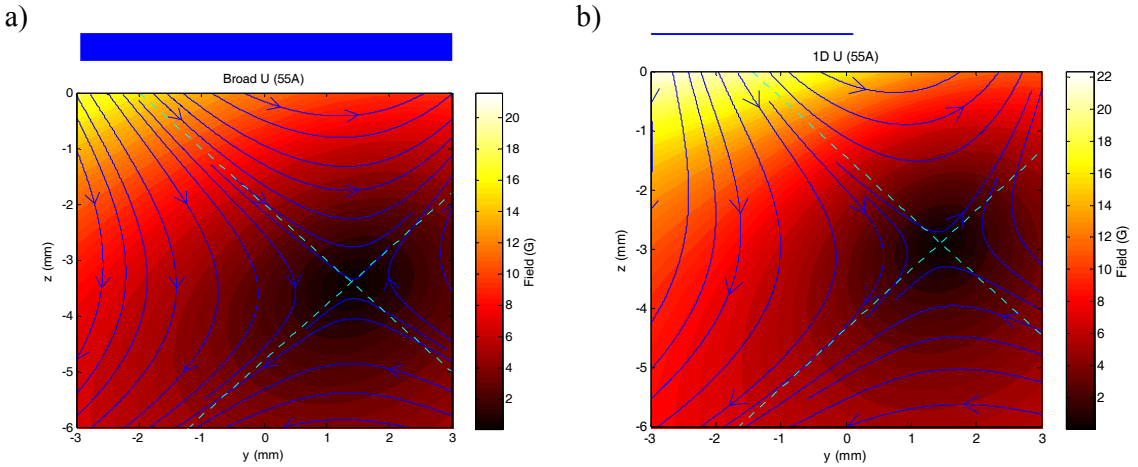

Figure 48 – Comparison of the deviations from an ideal quadrupole field orientation for a U with a thick, broad plate-shaped crosspiece (a) and a U made of a one-dimensional wire (b). The blue bar and line in (a) and (b) respectively indicate the relative position of the U's in each case (seen from the side). The broad U actually extends beyond the limits of the graph (note that here, it is seen as if the mount was in place in the chamber – the wires are *above* the trap, rather than below it). The mirror surface is at z=0. The colors indicate field strength, while the blue lines indicate magnetic field lines and the dashed cyan lines indicate the ideal quadrupole orientation. As can be seen, while the deviations in both cases are approximately the same to the negative-y direction of the minimum, the field lines to the positive-y direction are considerably closer to the ideal case in (a).

3.1.5 Coordinate system and system definitions

Since from this point we will begin to discuss real systems which exist in the lab, it is necessary to define the coordinate system we use. The chip surface is always in the xy plane at z=0; the xy origin is at its center. Unless specifically mentioned otherwise, the graphs are "upside down" – that is, gravity pulls in the direction of positive z.

Current flow is defined as follows. In the case of a straight wire, positive current means the current is flowing in the positive direction along the axis the wire is aligned with, and *vice versa* for negative current (leads are ignored for this purpose).

The current direction in the U- and Z-wires are slightly more complicated to define, since they are constructed from a single continuous wire whose direction varies; in both cases, there are two sections parallel to one another[31] and a third section perpendicular to them[32]. The sign of the current is determined by the direction of current flow in the latter section.

Specific examples of the coordinate systems used for various systems[33] can be seen in the schematics of the wire traps in 2.1.3 (such as Figure 9) as well as those in Chapter 5.

[31] As noted previously, these will be referred to as the "legs".
[32] Referred to as the "crosspiece".
[33] It should be noted that in some of these systems, the z axis is reversed from what is described in this section – this is specified in the relevant text.

3.2 Experimental design: Mount 1

3.2.1 Motivation

As noted in the previous chapter, since we wish to place (magnetic) field-generating structures in the vicinity of the cooled atom cloud for various experiments, doing so in conjunction with a six-beam MOT is problematic, hence the use of a mirror MOT. While a basic mirror MOT simply requires external coils and something to hold the mirror in place, manipulating the cooled cloud requires additional structures in its vicinity. In addition, as noted in section 2.1.3, generating the quadrupole field (and other fields, at later stages) by use of wires in the vicinity of the trapping location allows better trap gradients for smaller currents.

3.2.2 Design

In order to generate the requisite fields, as well as support the mirror (a chip, in this case), we designed the system designated in this work as Mount 1. The mount is intended to generate the fields (except the external bias fields) needed to generate quadrupole (MOT) and IP traps, as well as supply current to the wires on the chip itself for various experiments. Figure 49, Figure 50, and Figure 51 show the mount and point out the components comprising it. These components will be briefly described below; detailed schematics of the H- and U-wires may be found in Appendix D.

1) Flange - The flange is the interface between the vacuum chamber's interior and the outside world. Eight power feedthroughs, each capable of passing a current of 185A, are welded to the flange, passing power for the U- and H-wires into the vacuum chamber, and a 35-pin instrumentation feedthrough transfers current to the wires on the chip[34].

[34] A note on terminology. Throughout the discussion of the mount, "chip wires" will refer to the wires on the surface of the chip, while "pin wires" will refer to those wires which lead current **to** the chip.

a)

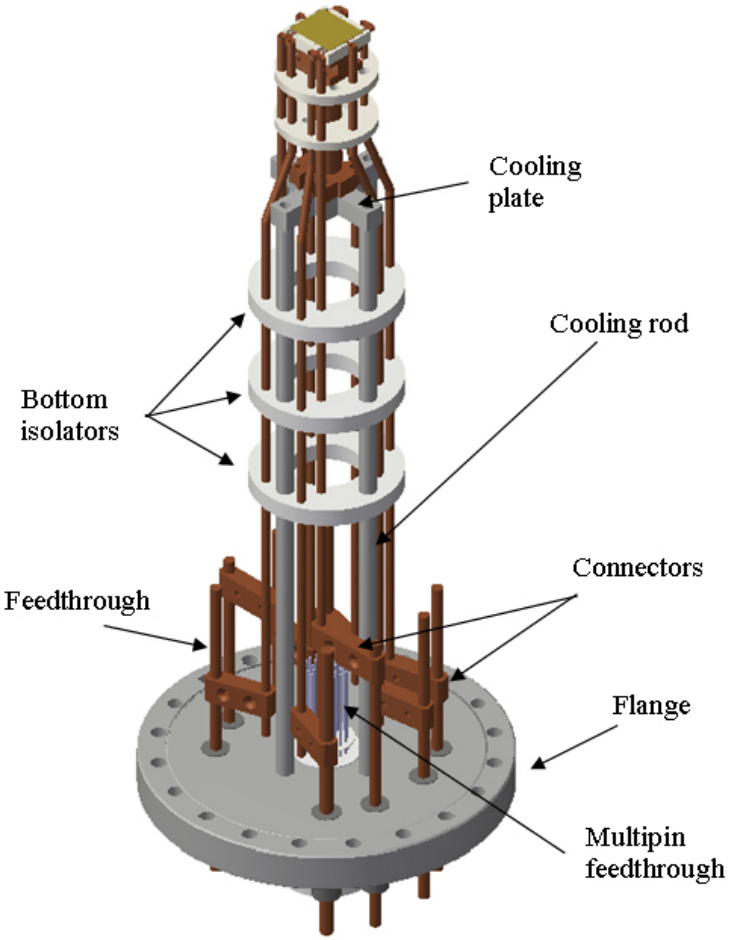

b)

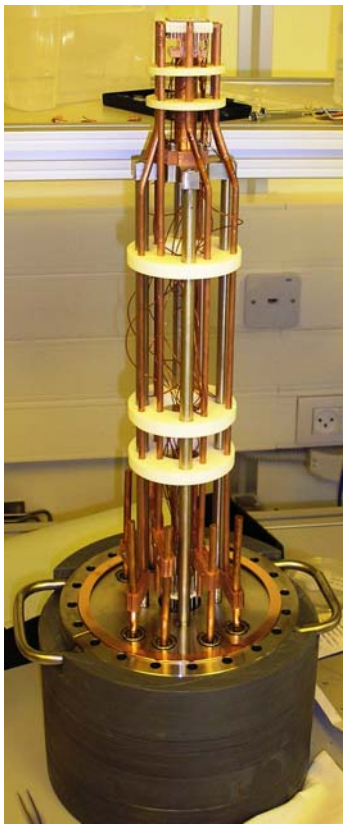

Figure 49 – Mount 1 diagram (a) and actual (b). The wires and pins which lead current to the chip can be seen in (b). It should be noted that when inside the chamber, the mount is upside down relative to what is shown here.

2) Cooling rods and cooling plate - As noted above, these four 316LN stainless steel rods are welded to the flange. They are connected (by means of screws) at their tops to a cross-shaped 316LN plate, which locks them into the proper alignment. The purpose of this structure is twofold. First, it supports the upper portion of the mount and stabilizes it against vibrations. Their secondary purpose is to assist in carrying heat out of the system, though most of the heat is channeled through the copper rods.
3) Copper column and copper block - Like the cooling rods and plate, the copper column and block are intended to support the upper section of the mount, and to carry some of the heat away.

a)

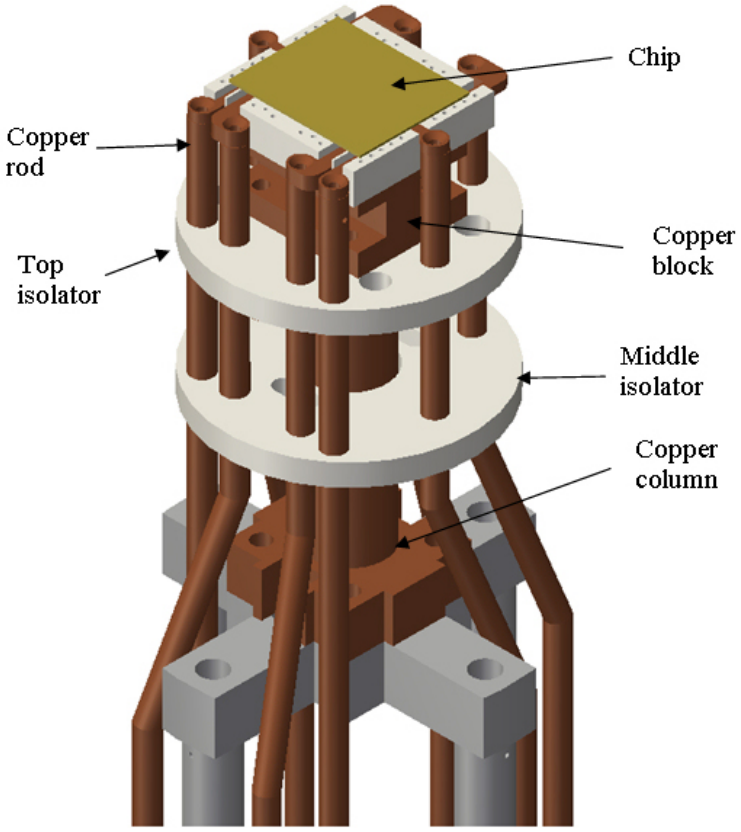

Figure 50 – (a) Close-up diagram of the mount's upper section (the wires on the chip itself are not shown here) (b) photo of the same section (not all the wires leading up to the chip are present here)

b)

4) Top, middle and bottom isolators - The term "bottom isolator" actually refers to the *three* lowest isolators, which share the same design. The middle and top isolators each have separate designs. These disk-shaped ceramic pieces are intended to hold the copper rods in place, preventing them from swinging and assuring their alignment relative to the termini of the copper wires.
5) Connectors - These copper connectors connect the power feedthroughs to the copper rods. Because not all the rods are at same distance from their respective feedthroughs, the connectors are made in two sizes.
6) Copper rods - These 5mm-diameter copper rods carry the current to and from the U-wire and H-wires. In addition, they serve as heat sinks for those wires, carrying away most of the ohmic heat generated by the high currents passing through them. The tops of the rods are highly polished, to ensure better electrical contact with the wires – the total wire resistance is on the order of 0.1Ω or less.

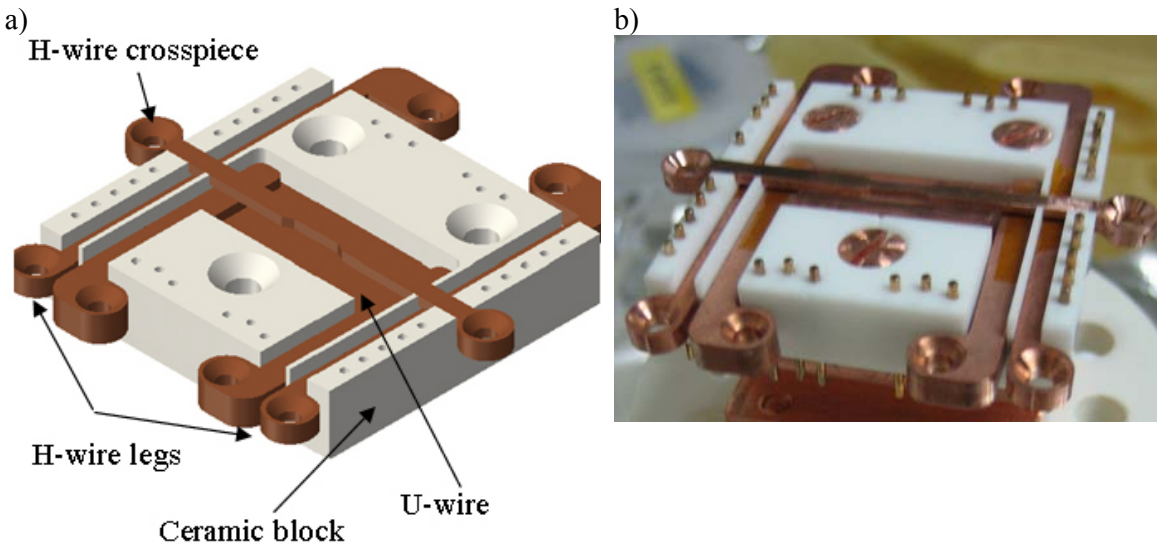

Figure 51 – Diagram (a) and image (b) of the ceramic block and the field-generating wires. The pins used to transport current to the chip can be seen in (b). The orange-brownish patches seen on the copper pieces in (b) are strips of Kapton tape, placed to prevent the risk of electrical contact. The rounded termini at the end of each wire are the points at which the copper rods are attached (using screws)

7) Ceramic block - The purpose of this block is to properly position the wires and to support the chip and the pins which pass current to it. It is the most crucial component in the mount and is shown in Figure 52. Each wire for the U- and H-traps is placed in a channel cut into the block. The small holes around the perimeter hold pins which are connected to the wires on the chip; the central portions of the block's perimeter are left without pins so as to leave a clear axis for optically imaging the ultracold atom cloud. The block was fabricated from MACOR. This machinable ceramic material has a high electrical resistivity, insulating the various current carriers from each other. Unfortunately, MACOR's thermal conductivity is poor, meaning that most of the heat generated by ohmic heating must be removed by the copper rods and the pin wires
8) Pin wires - These 28 wires (plus one for ground) pass current from the outside of the chamber (through the 35-pin connector in the flange) to the wires on the chip.
9) Pins - These beryllium copper (BeCu) pins transfer current from the pin wires to the chip. The pins are glued in place in the MACOR block; the pins' upper surfaces are bonded to the appropriate electrical connections ("pads") on the chip – using several 25μm-diameter (1 mil) wires for each pad – by means of an ultrasonic bonder.

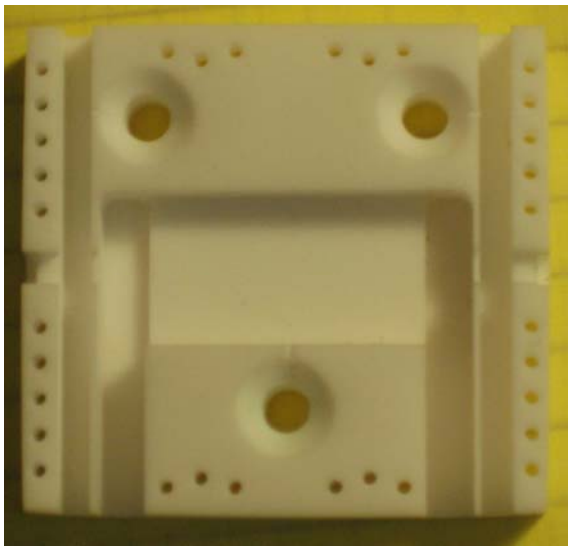

Figure 52 – The ceramic block.

10) U-wire and H-wire (crosspiece and legs) - These copper structures[35] generate the magnetic fields used in the experiment. As described in section 2.1.3, the U-wire creates a quadrupole field, while the H-wire creates an IP field[36]. The former is used to generate a MOT, while the latter is used for later stages of the experiment (including evaporative cooling to create a Bose-Einstein condensate). The central plate of the U-wire is broad and thick, allowing a better approximation of an ideal quadrupole field[37] [6].

[35] In the context of this and similar designs (such as those described in Chapter 5), the off-chip field-generating wires (the U- and H-wires, in this case) are sometimes collectively referred to as the "copper structures".
[36] The H-wire crosspiece's central section was designed to be narrower than the rest of its length for a later stage of the experiment.
[37] See section 3.1.4.

a)

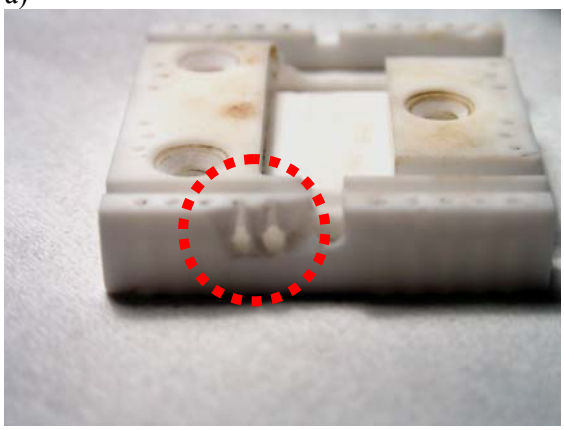

b)

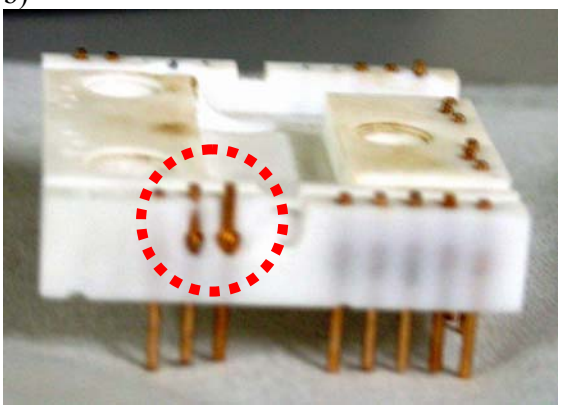

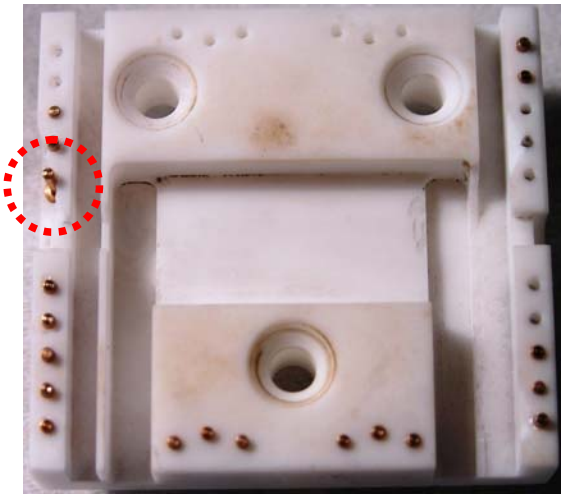

Figure 53 – A cutaway view of the pins' channels in the ceramic block (marked by the red circles) without (a) and with (b) the pins in place, and seen from above (c). The block shown here was broken - normally, the channels are open only on the top and the bottom (as can be seen on the right side of the block in (b)).

The legs of the U-wire have a larger cross-section than the plate, again reducing the wire's total resistance, and thus its heat generation. Figure 54 shows the current distributions and the temperatures reached; for low currents and/or short times, the temperature increase is not significant, but operation for long times at high currents would require some means to reduce the heat, such as an alternating work cycle (where the current is on for a given interval and off for another interval; a 50% work cycle, for example, is the case where both intervals are the same length). This is important because excessive heating (in particular in the crosspiece, which is both the most prone to overheating and the only piece in direct contact with the chip) may damage the chip (either directly or by warping as the crosspiece expands) and may cause outgassing in the copper, compromising the vacuum at exactly the location where the best vacuum is needed.

a) b)

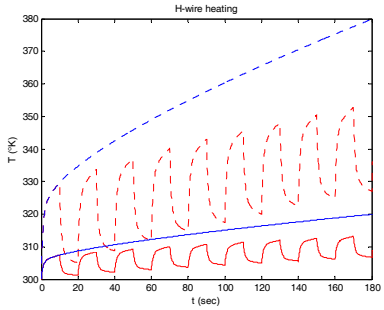

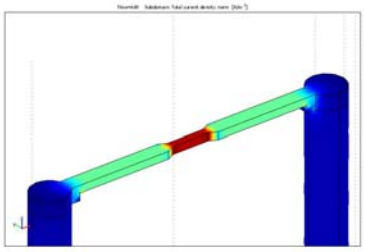

c) d)

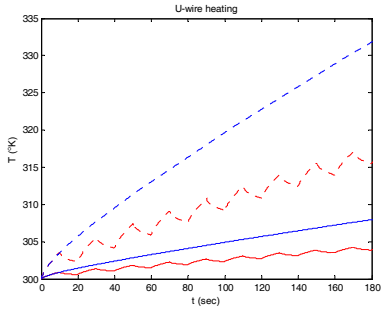

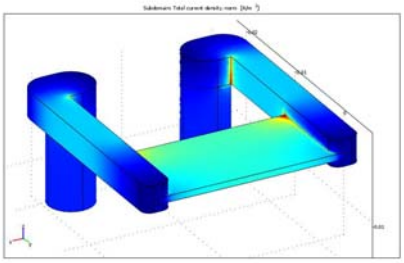

Figure 54 – Current densities and heating in the U-wire and the crosspiece of the H-wire (the H-wire legs are not shown here; their current density is somewhat lower than the crosspiece's – and they have no narrower sections to increase it at one point - so consequently their heating is also lower). Graphs (a) and (c) show temperature vs. time for a current of 50A (the solid lines) and 100A (the dashed lines) in the crosspiece and U-wire respectively. The blue lines indicate temperature if the current is constant; the red lines indicate temperature for a 50% work cycle with an interval of 10 seconds. Plots (b) and (d) show the current distribution in the crosspiece and U-wire respectively; dark blues indicate low current densities, increasing through light blue, green, and yellow to maximum density at red (although the color scale is not the same in both graphs).

The atom chip

The atom chip has two functions in the overall experiment. Initially, the chip serves as a mirror, for the creation of a mirror MOT. Subsequently, after atoms have been cooled first in the MOT and then by optical molasses, the atom cloud is brought closer to the chip by manipulation of the magnetic fields formed by the H-wire and the wires on the chip, where a variety of experiments on it may then be performed.

Figure 55 shows the atom chip used in this experiment. It is fabricated from a 500μm-thick silicon wafer covered by a 2μm-thick gold layer. Channels are etched in the gold to form electrically isolated wires. The chips we used were fabricated in the BGU nano-fabrication facility [54].

a) b)

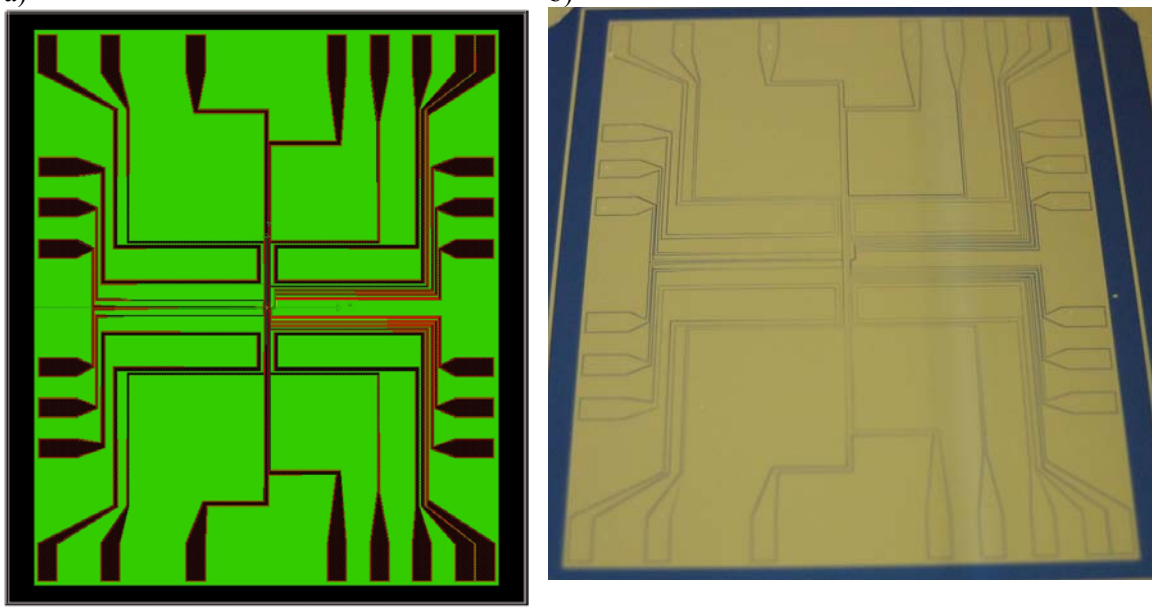

Figure 55 – The atom chip in schematic (a) and actual views (b). Note that in these views, the (black) sections of wafer surrounding the chip edges have not yet been removed. The broader areas on the edges are the pads through which current is supplied to the wires on the chip.

To prevent overheating and thus damage to the chip, we limit the current in each chip wire to a maximum current density on the order of 10^{-2} A/μm^2 for the larger wires and 1 A/μm^2 for the thinner ones (see [55] for a discussion of heating in chip wires). Higher currents risk vaporizing the wire.

A full description of the function of each wire is beyond the scope of this work. Of note, however, are the wires known as the main loading wire and the four U-wires, which can be seen in Figure 55a (see also Appendix E).

Ideally, the top of the chip should be parallel to the flange (and thus to the optical table). In practice, there was a 0.13º angle between the two planes, not enough to cause a significant effect.

3.2.3 Initial experiment and results

The experimental sequence summarized in Table 1 is typical for atom chip experiments [7]; this sequence was repeated for each measurement (constituting an "experimental cycle") since measuring the cloud heats it or requires its release [34-36], thereby destroying it. The experimental measurements presented in this section were conducted by Tal David and Ran Salem; the analysis software used was written by Shimi Machluf and Mark Keil.

#	Stage
1	U-MOT
2	Compression of the trap
3	Optical molasses
4	Optical pumping
5	Loading the IP trap

Table 1 – The experimental sequence

Stage 1- Establishing a U-MOT: The magnetic field was generated by a current of 44A through the U-wire and a 7G bias field along the y axis. The cooling laser beam was red-detuned relative to the F=2→F'=3 transition in ^{87}Rb, resulting in a MOT centered 7mm below the chip surface. At the end of this stage, the trap contained up to 10^8 atoms at a temperature of approximately 300μK (measured by using the time-of-flight method [34-36]). The number of atoms in the trap was calculated from the optical absorption profile of the MOT (Figure 56b). The size of the cloud was taken to be twice the standard deviation of Gaussian curves fitted to the absorption profile in both directions.

Stage 2 - Compressing the resulting cooled atom cloud: The current in the U-wire was increased to 95A and the bias field increased to 24.3G. This moved the trap towards the chip (for loading into the IP trap) and increased the trap gradients. At the end of this process, the atom cloud was approximately 2mm below the chip surface.

Stage 3 - Cool the atoms further by optical molasses: All magnetic fields were switched off, and the cloud cooled further by means of optical molasses. The atom cloud consisted of 5-8x10^7 atoms at a temperature of 40μK at the end of this stage.

Stage 4 – Optical pumping: Following the optical molasses, the atoms were equally distributed over the five magnetic sublevels of the F=2 ground state. Since only two of those states are weak-field seekers, a laser was used to pump the other m_F states into the m_F=2 state.

Stage 5 – Loading the IP trap: The current was ramped up in the H, establishing the IP trap. Measurements of the number of atoms in the trap before and after loading indicate that the loading efficiency (atoms retained in the trap after the magnetic field is created) approached 100%.

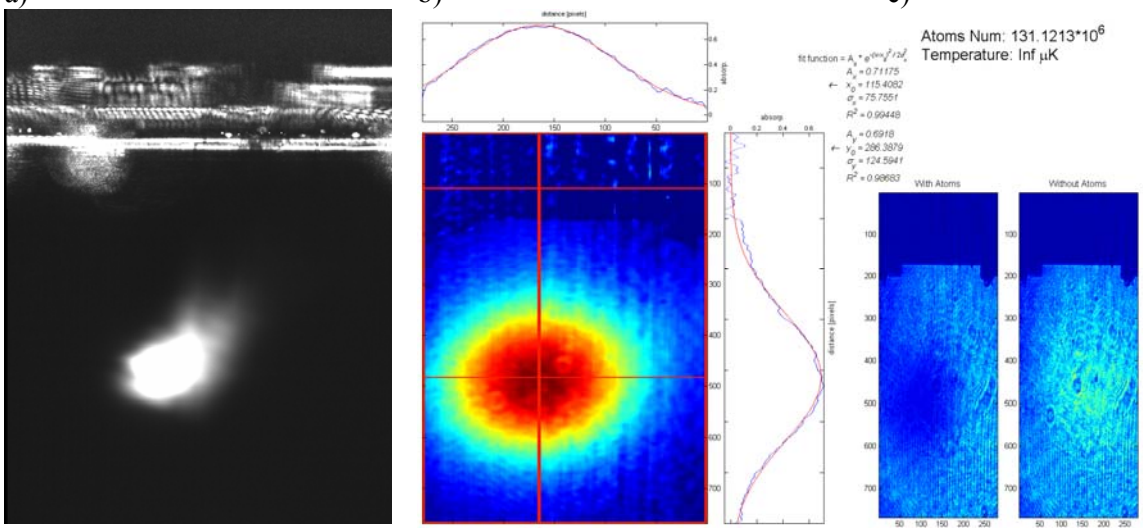

Figure 56 – Two images of the U-MOT achieved in the system. The cloud in the image on the left (a) shows the fluorescence of trapped ultracold Rb atoms at 780nm. The trapped atoms appear as the large region of light seen in the bottom half of the image. The bright horizontal bar above the trapping region is the chip (seen edge-on) and the bright "bump" on its left is light reflected from one of the pins. The image in the centre (b) shows an absorption profile of the MOT; the size of the MOT cloud in this image was estimated with a Gaussian fit (the graphs above and to the right of the image) to the image (in this version of the program used for the estimate, the temperature is not determined, hence the "Inf" value). The two images (c) at the extreme right show the imaging laser beam with and without atoms present in the trap, respectively; their ratio is used to determine the absorption image that is shown in (b).

4 Simulation techniques

4.1 Software used

Three programs were used to generate the simulations in this thesis:

1) Mathematica (version 5.2) – Mathematica was primarily used for simulations based on analytical equations and expressions (or to derive those equations, such as those in Chapter 2, in the first place). Mathematica generally allows more accurate simulations – since it generates equations, which may be used to find the field at any desired point, it generally avoids the problems of grid resolution which can occur with MatLab (see below). However, generating the desired equations may, in more complex cases, be extremely time consuming and sometimes impossible.
2) Comsol Multiphysics (versions 3.1-3.3) – this software (known as FemLab prior to v3.2), unlike Mathematica and MatLab, has the capability of defining models with a CAD interface (the Magsim program referred to below can also do so, but only to a very limited extent) and solving them with finite element methods. This makes it much easier to create models of the current-bearing structures used. Even more importantly, Multiphysics can calculate the current distribution in a 3-D, nonuniform wire, making it possible to take into account the current density changes referred to in section 3.1.1, creating an accurate model of the actual system.
3) MatLab (version 7.2) – This program was our primary tool for data analysis. While Multiphysics brings crucial capabilities to the table, it is sometimes inconvenient to extract numerical data from it, and more critically, calculating magnetic fields with it is a very time- and memory-expensive problem – often prohibitively so. Because of this, we used a combination of Multiphysics and MatLab.

4.2 Simulating the magnetic field

Most of the magnetic simulations in MatLab were based on a program known as Magsim, written by Dr. Yoni Japha. The inputs this program receives are (through a GUI) a wire configuration composed of several elements – each of which represents a single

continuous wire – and three vectors representing the desired x, y, and z coordinates[38]. The combinations of these three coordinate vectors form a coordinate grid in space, which is cuboid in form. The program uses these inputs to construct a structure array (known here as "mag"), each element of which corresponds to a single element in the wire configuration, and which contains the following fields[39]:

1) B – a 3*m*n*k array which contains the x, y, and z components of the magnetic field generated by a current of 1A through the element in question at each point on the spatial grid.
2) absB – an m*n*k array which contains the absolute magnetic field magnitude at each spatial point, under the same conditions as B.
3) coords – this field is an array of three cells; each cell (1,2,3) contains the respective coordinate vector (x,y,z).

Two functions, called sumelements and biasAdd[40], were then used to generate the actual fields, given a current vector I (which has one current – that can be 0 – for each element) and (optionally) an external homogenous bias field. Once the total resulting field is calculated, the data can be used for various graphs, calculations, and analyses. This particular approach was designed to allow rapid calculation of different current parameters; while it is possible to do a new calculation of the entire structure "from scratch" every time a new plot is needed, doing so is extremely time-consuming.

4.3 Modeling the wire configuration

The current-bearing structures can be modeled in Magsim in two ways.

1) The first method is native to the program – each element consists of a single continuous wire, for which the coordinates (for the termini and for each bend) are supplied by the user. The wire can be considered to be one-dimensional, or can have a thickness (with either a circular or a rectangular profile). In the latter case, the thick wire is simulated by breaking it into multiple discrete "filaments", each of which is considered a one-dimensional wire and which carries a portion of the current.
2) The second method involves use of Multiphysics. The structure is drawn and modeled in Multiphysics, and then solved. The structure is divided into compartments, each of which contains a vector representing the current

[38] These vectors each have m, n and k elements, respectively.
[39] Not all the fields are described here, as some are not relevant to the way I used the program here.
[40] The m-file code for these two functions can be found in Appendix F.

distribution at that point (the compartment's center). The resulting matrix of current distributions is then imported into Magsim.

The first method has the advantage of speed; it is significantly faster for Magsim to calculate the field in that case. However, it has a critical disadvantage in that it does not take into account changes in current distribution at bends; the current density is uniform throughout the wire, and is always parallel to its center (so for example, in the case of the Z-wire shown in Figure 38, the current would abruptly switch direction by 90 degrees at the bend, and would always be aligned with the wire).

Figure 57, Figure 58 and Figure 59 show a comparison of the magnetic fields generated by three systems – a straight wire, a Z-wire whose length (the distance between the x-axis centers of the leg wire sections) is 7mm, and a very long Z with a length of 23mm – as calculated with Magsim and Comsol Multiphysics. In the case of the straight wire, the field is also calculated analytically. For each system, 6 evaluations of the field were carried out – along the z axis (above the minimum and above a second point), along the x axis (at two different heights) and along the y axis (at the same heights). Each calculation (except the analytical calculations) was done twice for each program. In the case of Magsim, the calculations were done using a 4-filament model and with a 10-filament model. In the case of Multiphysics, one model used 60 points (compartments) along the x-axis and the other used 90 points. In all cases, the center of the wire is assumed to be at the origin, and it has a rectangular cross-section of 1x1mm.

Several things can be seen from these comparisons. In the case of the straight wire (Figure 57), the results given by the various techniques for fixed x and y converge approximately 1mm above the surface of the wire as z increases (Figure 57e and Figure 57f). The evaluations done with Multiphysics, however, are slightly more divergent from the analytical (theoretical) case than the Magsim filament simulation.

A critical limitation of Multiphysics can be seen in the simulations along the x axis (Figure 57a and Figure 57b). Since the current density model is divided into a finite number of compartments, which are evaluated as discrete points ("concentrating" the current at certain points), the model has a finite resolution. As a result, when moving along the x axis, the field fluctuates. Close to the wire (Figure 57a) these fluctuations can become quite significant (note the large scale change between Figure 57a and Figure 57b). These fluctuations can be significantly reduced by increasing the density of the current density matrix (increasing the number of points – however, this has a cost in memory and execution time). Along the y axis, all the techniques tend to show similar results. In both the x-axis and y-axis cuts, as the distance from the wire increases, the different methods give closer results.

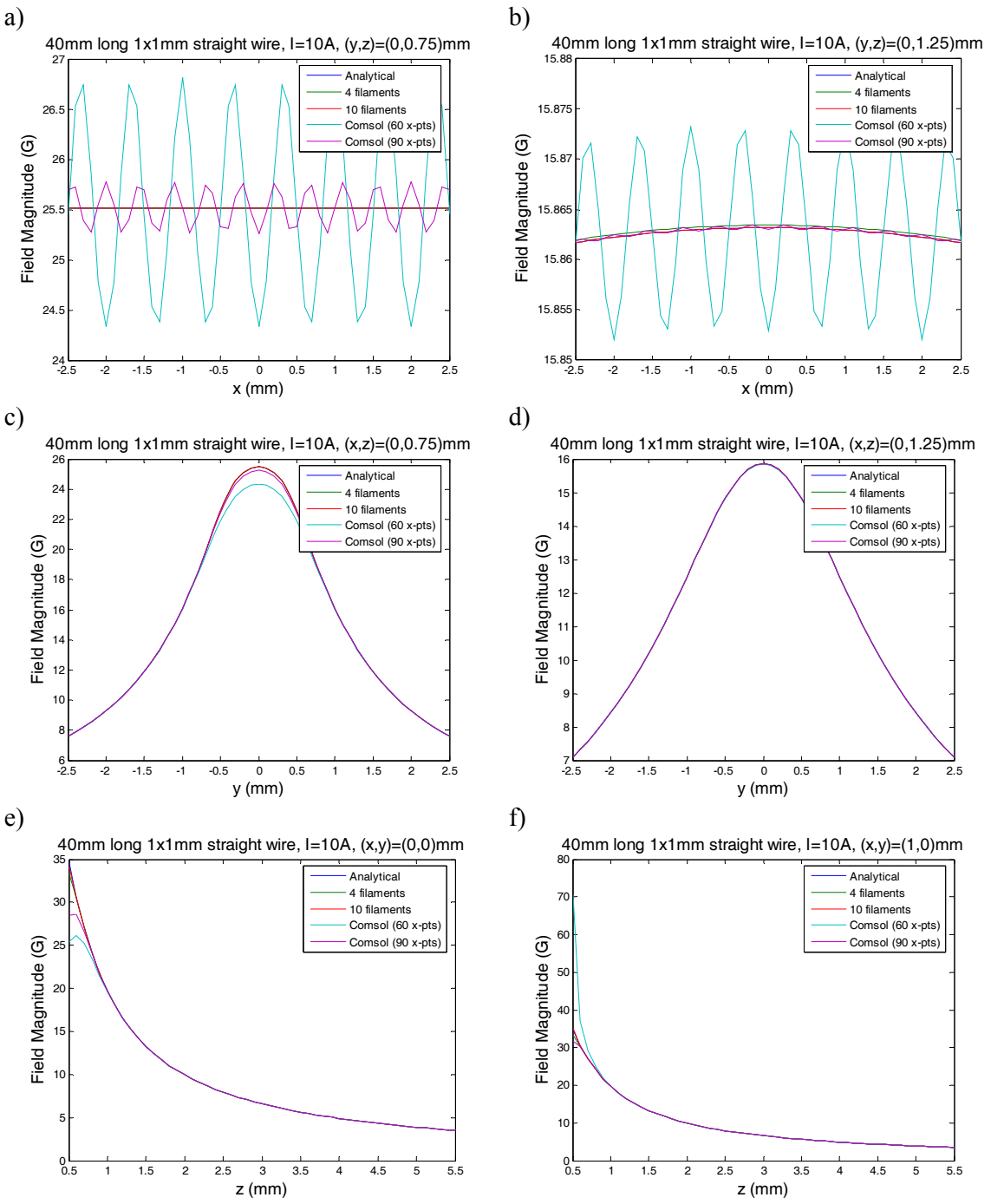

Figure 57 – Magnetic simulations with filaments vs. Comsol Multiphysics for a straight wire. Analytical results are also shown, but are obscured in (a) – as are the results of the 4-filament simulation -- because the values are nearly identical.

In the case of the 7mm-long Z-wire (Figure 58), the situation is different. The different techniques do not converge nearly as quickly for increasing distances from the wire (e and f). Also, along the x and y axes, there is a distinct gap between the fields of the two Multiphysics simulations and those given by the Magsim simulations. This is caused by the difference at the crosspiece ends – as noted above, Magsim cannot accurately model the changing current

direction in the wire bends. The troublesome fluctuations so obvious for the Multiphysics straight-wire simulations is absent here because the 7mm Z is shorter on its x axis than the other two systems, so the current density matrix is denser for a given number of points.

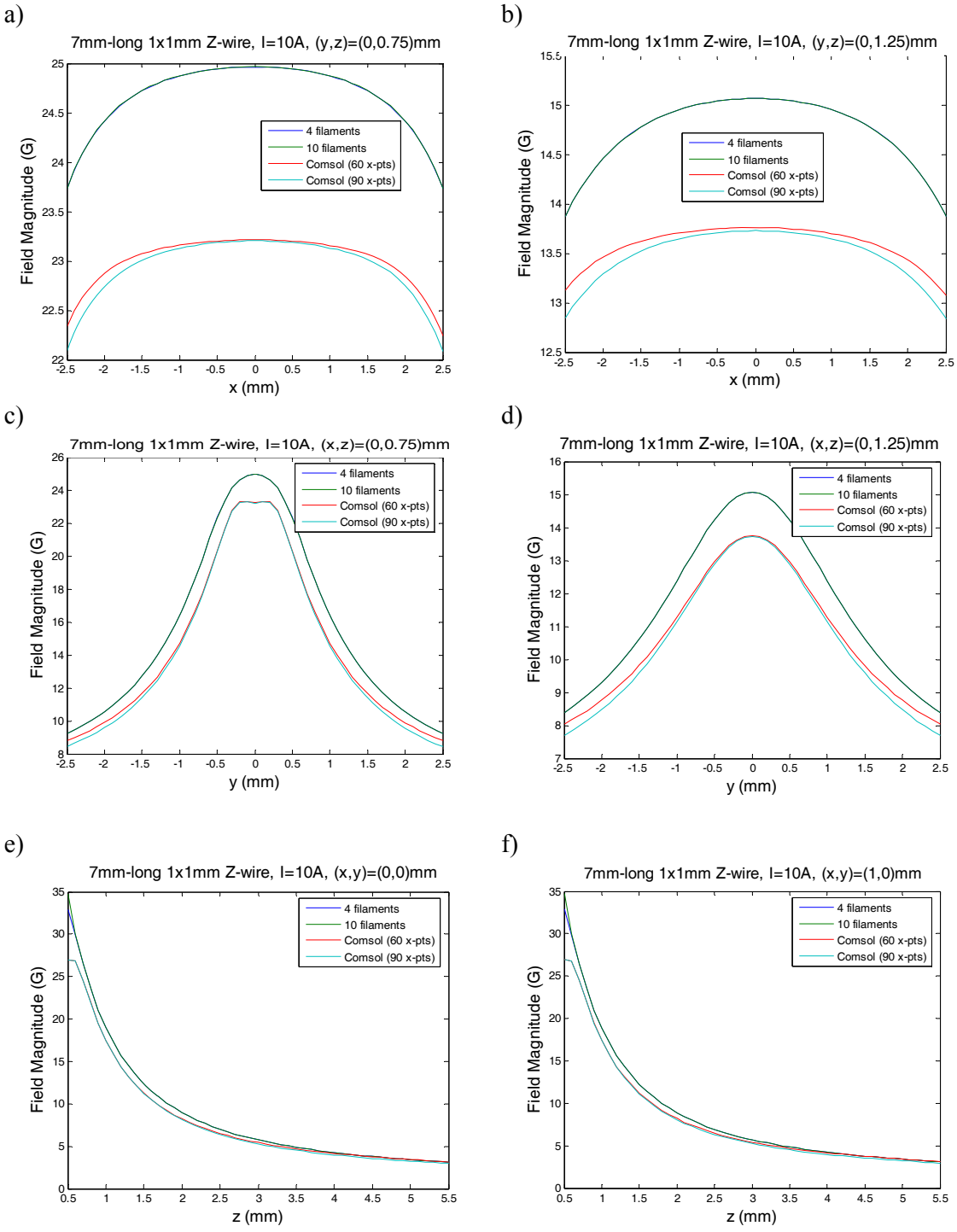

Figure 58 – Magnetic simulations with filaments vs. Comsol Multiphysics for the 7mm wide Z-wire

For the 23mm-long Z (Figure 59) there are similar effects. However, the greater distance between the ends means that the results are closer to those for the straight wire.

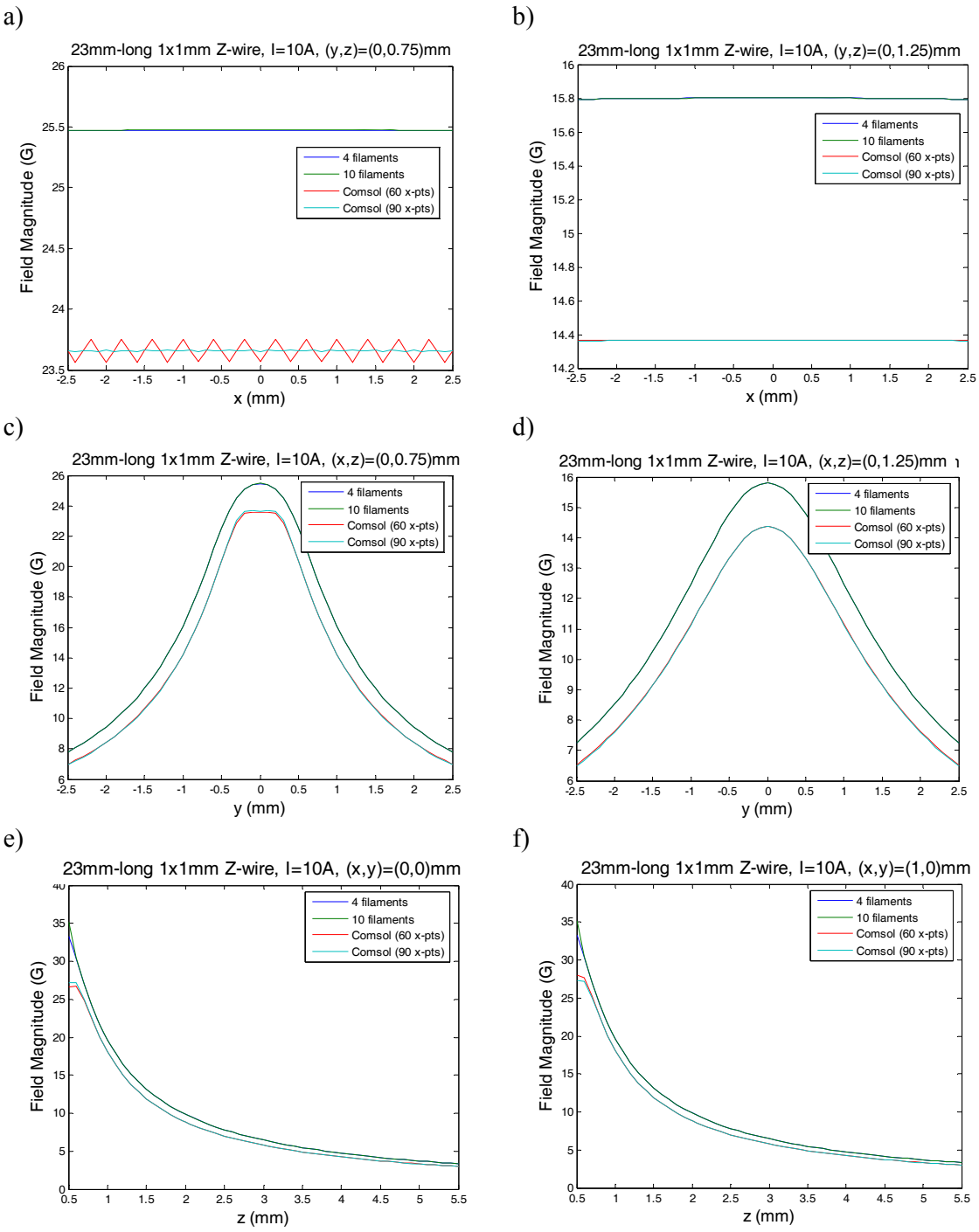

Figure 59 – Magnetic simulations with filaments vs. Comsol Multiphysics for a 23mm wide Z-wire.

In conclusion, for a long straight wire (or wire section) using Magsim to construct the model of the wire is preferable – it will give accurate results quicker than Multiphysics. However, as the separation between bends in the wire decreases, it becomes more important

to use an accurate model for the current direction, requiring the use of Multiphysics. It is, however, *extremely* important to consider the geometry being modeled and to select a sufficiently dense current matrix. Otherwise the problems demonstrated in Figure 57a can have a disastrous effect on the simulation's accuracy.

4.4 Cross-checking the simulation results

a)

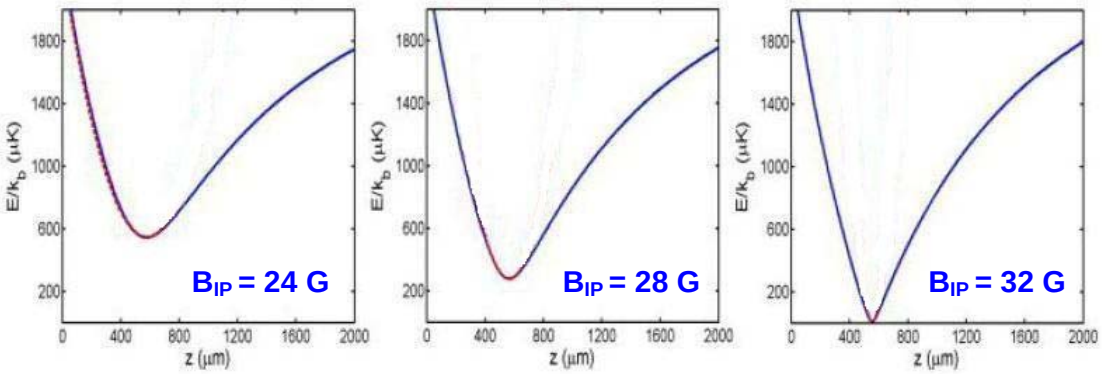

b)

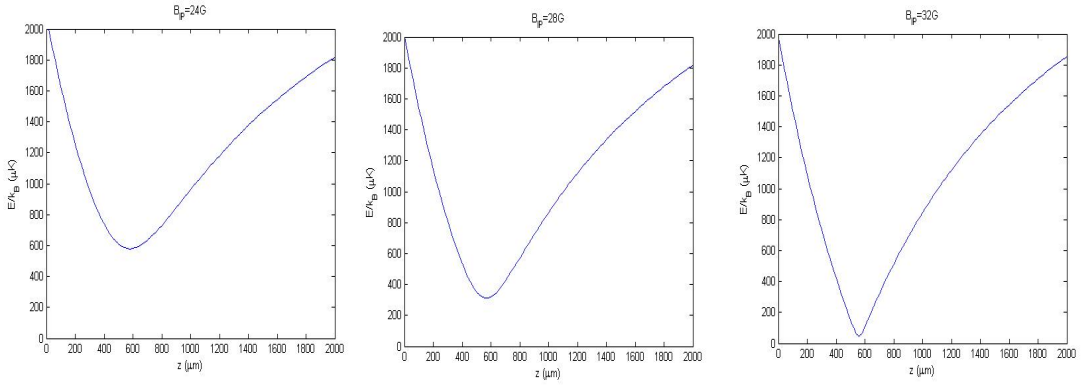

Figure 60 – Cross-check of magnetic simulation program. The x-axis indicates distance from the chip, while the y axis indicates the potential. B_{IP} indicates the x-bias field. See text for further details. The plots in (a) where taken from [7].

As a test of the program, we recalculated the magnetic trap described in [7] and compared our results to those described therein.

Figure 60 shows the results of that comparison. Figure 60a shows the graphs from [7], while (b) shows the graphs I calculated for a similar system (a Z-trap in both cases). As can be seen, our simulation resulted in an almost exact match – the shape of the field is virtually the same. There is a slight difference in the minimum value for the graph at the highest bias field; this is probably due to small differences in the initial models used in each simulation.

4.5 Resolution limitations

While Magsim can give accurate results when calculating the field at a specific point or points known in advance, limitations arise when trying to analyze the resulting field (e.g. when trying to find the location and/or magnitude of the field minimum), since such analyses generally require evaluation of the field at locations between the grid points where the field has been calculated explicitly. Consequently, the desired result may be affected by the resolution of the coordinate grid (e.g., in general, the actual minimum lies between points on the grid, but the point found will be at one of those grid points exactly). This creates a gridding error, or a resolution limit, in most simulations. The problem may be minimized by increasing the resolution (decreasing the spacing between grid points) but this requires reducing the overall size of the coordinate space due to considerations of memory and execution time. One way to deal with this issue is to use a dense coordinate grid covering a small region (when the region of interest is known in advance) to calculate the desired values and then use those values in a lower-resolution but larger grid for displaying results graphically over a larger volume.

Besides errors in analyses, resolution may also cause difficulties in graphing. While limited resolution is often a mainly aesthetic issue, it can be a major problem in certain instances, for example when generating isosurface plots.

An isosurface plot is a 3-dimensional plot displaying a surface defined by some function (or data set) so that the value of the function at all points on the surface is identical. A simple example is the electric field of a point charge, for which the isosurface is a sphere centered on the charge. In the case of this particular work, the plots of concern are equipotential plots – plots showing areas of constant potential (i.e. magnetic plus gravitational fields).

In these plots, resolution can be a critical issue. In areas where the gradients of the data values (the potential in this case) are large, relatively widely spaced points may cause errors in the interpolation function used to generate a continuous surface. This gives the surface a "lumpy" look, and may show false potential barriers. This can be disastrous when trying to determine the true shape and extent of the equipotential surface.

a) b)

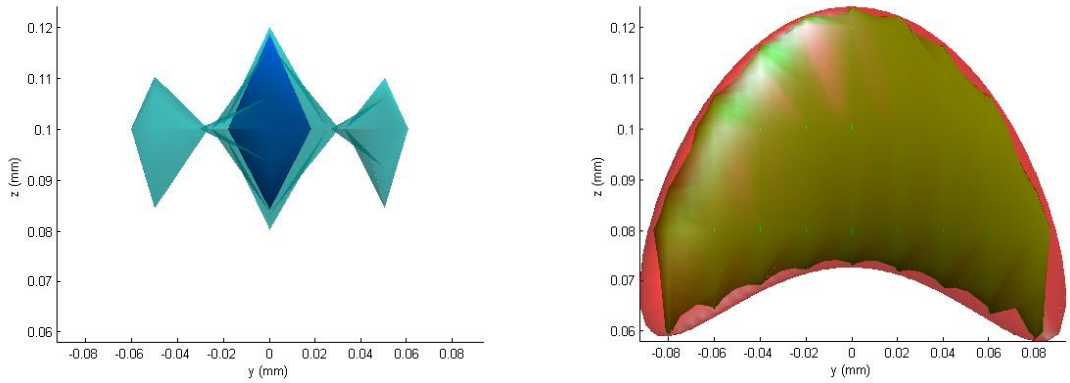

Figure 61 – Effects of varying resolutions on isosurface plots. See text for details.

Figure 61 demonstrates this effect. It shows the same potential, plotted with grids of four different resolutions: 100 μm/point (blue surface), 50 μm/point (cyan), 20 μm/point (green) and 5 μm/point (red). As can be seen, at the lowest resolution, only a small part of the surface appears. At 50 μm, a greater part of the surface is visible, but there are three separate "clusters", which may indicate (falsely, in this case) the existence of multiple minima. As the resolution is increased still further, the "real" shape of the potential emerges, though it is still lumpy in form, and its full extent is unseen, until the highest resolution of 5 μm/point is used.

Though it is not visible in the graphs, the plots above are also examples of another problem caused by resolution. The program which generated the plots also finds the location of the potential minimum. For all but the highest resolution, the location of the minimum is found to be at (x,y,z)=(0,0,0.1)mm. But at the highest resolution, it is revealed that the minimum is actually at (x,y,z)=(0,0,0.095)mm. While the difference in this case is quite small, this can be problematic when very high accuracy is required, such as when simulating traps very close (on the order of tens of microns) to the chip surface. This issue must always be born in mind, and great care employed to avoid being led astray by false data – as will be described later, gridding issues can give severely erroneous results, e.g. for frequencies or trap depths.

A second, less serious drawback, of calculating the field on a grid is that the coordinate space is fixed; changing the grid can be very time consuming (though not prohibitively so).

4.6 Specific algorithms

4.6.1 Finding a bias field

One problem that must be solved often is finding the bias field required to achieve a potential minimum at a specific point with specific currents running through the wires, and with a particular magnetic field magnitude at the minimum. An algorithm was developed to calculate those bias fields in the fashion described below.

First, the magnetic field was calculated without the presence of a bias field. The negative of the resulting field at the desired point served as an initial guess as to the required field.

The field was recalculated, using the initial guess as the bias field. The potential resulting from this magnetic field was also calculated, and its minimum found – this is necessary because, as previously discussed, gravity may affect the location of the minimum – and the value of the field was checked at that point.

If both the magnetic field magnitude and the location of the potential minimum are at the desired values, the algorithm terminates here. Otherwise, the bias field on the y axis was adjusted by ΔB_{0y} to change the height of the minimum (its z-axis location). When the desired height was reached or passed, ΔB_{0y} was halved. If the minimum height was passed, its sign was inverted and the bias field adjusted again (this time in smaller steps) until the proper height was achieved or passed. If the field at the minimum was not at the desired value, the bias field on the x axis was, in a similar fashion, adjusted by ΔB_{0x}. After each change, the location minimum and magnetic field value at the minimum were recalculated.

The algorithm terminated upon encountering one of the following conditions:

1) When the desired values are reached (to within a specified tolerance).
2) When the program's run time exceeds a specified timeout limit.
3) When ΔB_{0x} or ΔB_{0y} becomes too small.

One problem that occasionally occurs is that if the x-axis bias field is adjusted in the wrong direction at the initial point, the field minimum splits into two (i.e. a component of the magnetic field changes sign) – while the algorithm contains checks to determine the correct direction in advance, the method used is not 100% effective. If necessary, the entire process is repeated, with the initial sign of ΔB_{0y} reversed.

This algorithm can obtain fairly precise results with a precision estimated to be 0.1G. However, the algorithm has considerable limitations in certain cases. While a change in the y-axis bias field primarily affects the minimum location, it also affects the field magnitude there, and *vice versa* for the x-axis bias field. In some wire/current configurations, these

changes in the bias field are significant, so the algorithm cannot achieve the desired values and it ends up oscillating around the desired values without ever achieving them. In addition, since the fields are calculated on a grid as described above, some of the calculated values for differing parameters may be exactly equal to each other, since those values would in actuality give points with locations spaced closer then the resolution. Alternatively, a graph of bias fields as a function of a given parameter may appear discontinuous, since values will "snap" to an approximate solution. Some examples of this can be seen in Table 3 (in Chapter 5).

Another problem which is occasionally encountered is that while changing ΔB_{0x} in one direction splits the minimum as described above, adjusting it in the opposite direction causes the height and/or field magnitude to move *away* from the desired value – in these cases, it seems that there is no bias field which will give a minimum for the specified location and current parameters.

4.6.2 Calculating longitudinal frequencies, trap width, and trap depth

Once a field with the desired parameters has been generated in the simulation, it is desirable to analyze it. One particularly important parameter is the longitudinal frequency of the trap.

The algorithm to calculate this is fairly simple in concept. Once the potential is calculated, it is "sliced" along the x axis into separate yz planes. In each plane, the location of the minimum (and the potential at that location) is calculated. Stringing those results together gives the minimum energy path (MEP).

Once that path is derived, the coordinates of the minimum on the path are identified, as are those of the two end points (these are classical turning points) along the path where the energy reaches a desired value. For each such energy U, a 2nd degree polynomial fit is calculated (using those three points), yielding coefficients a_1, a_2 and a_3 so that

$$U = a_1 r^2 + a_2 r + a_3 \qquad (3.5.1)$$

where r is the distance along the MEP. Consequently, by extension from equation (2.1.13), the longitudinal frequency for that energy will be given by

$$f_l = \frac{1}{2\pi}\sqrt{\frac{2a_1}{m}} \qquad (3.5.2)$$

Again, this method has the drawback that when relying on a field on a grid, the points on which the fit is calculated may not be at precisely the correct energies and coordinates. This can lead to problems in the vicinity of the trap bottom, which, if the MEP is plotted, will

appear as "bumps" in the parabola in the vicinity of the minimum. This may cause the algorithm to incorrectly calculate the quadratic fit, especially for lower energies.

Another issue to keep in mind is that this is accurate only for harmonic or nearly-harmonic traps. If the trap is not at least close to harmonic, it is not meaningful to talk about its frequency – it is more useful to calculate and compare trap gradients or volumes instead – in order to give a much more accurate picture of the degree of compression of the trap in three dimensions. Currently, we do not have an algorithm to calculate the volume[41], but for the purposes of comparing different traps, it is possible to use the length L of the MEP between the classical turning points at a given energy.

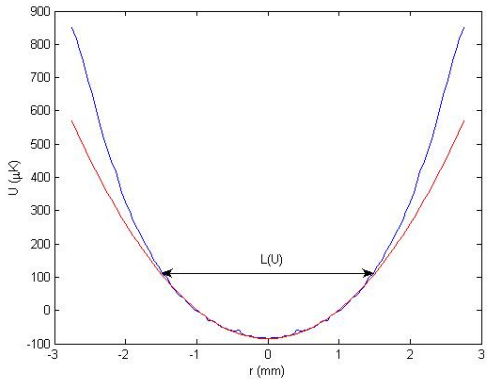

Figure 62 – Width of a trap. The trap here is somewhat anharmonic – the blue line indicates the actual calculated energy, while the red line is the fit. The black line is the length L of the trap in the longitudinal direction for a given energy U.

Figure 63 shows several examples of the problems described above. In (a), (b) and (d), the MEPs (blue lines) are smooth, but have markedly different frequencies at different energies in the trap – in other words, they are not harmonic – so a fit at one energy (the red line) will not necessarily result in an accurate result (the green line indicates an energy 67 μK above the minimum). In (c), the trap is "bumpy" near the minimum and at the energy where the fit is made, so the algorithm fits the wrong point, changing the calculated frequency from its actual value. One way to overcome this problem is to compare the calculated values for the frequency at several relatively low and closely-spaced energies; widely divergent frequencies would indicate the existence of such problems. The difficulties illustrated in Figure 63 prohibit meaningful comparisons between different potentials using only the calculated frequency as a figure of merit for the potential. While we could still make comparisons at very low energies – since, in the vicinity of the minimum, if the energy function is smooth it is very close to harmonic – we are often interested in much higher energies, where these problems have a major impact.

[41] If the trap is ellipsoidal in shape, it is possible to calculate the volume based on the longitudinal and transverse frequencies, but this is often not the case for some trap configurations.

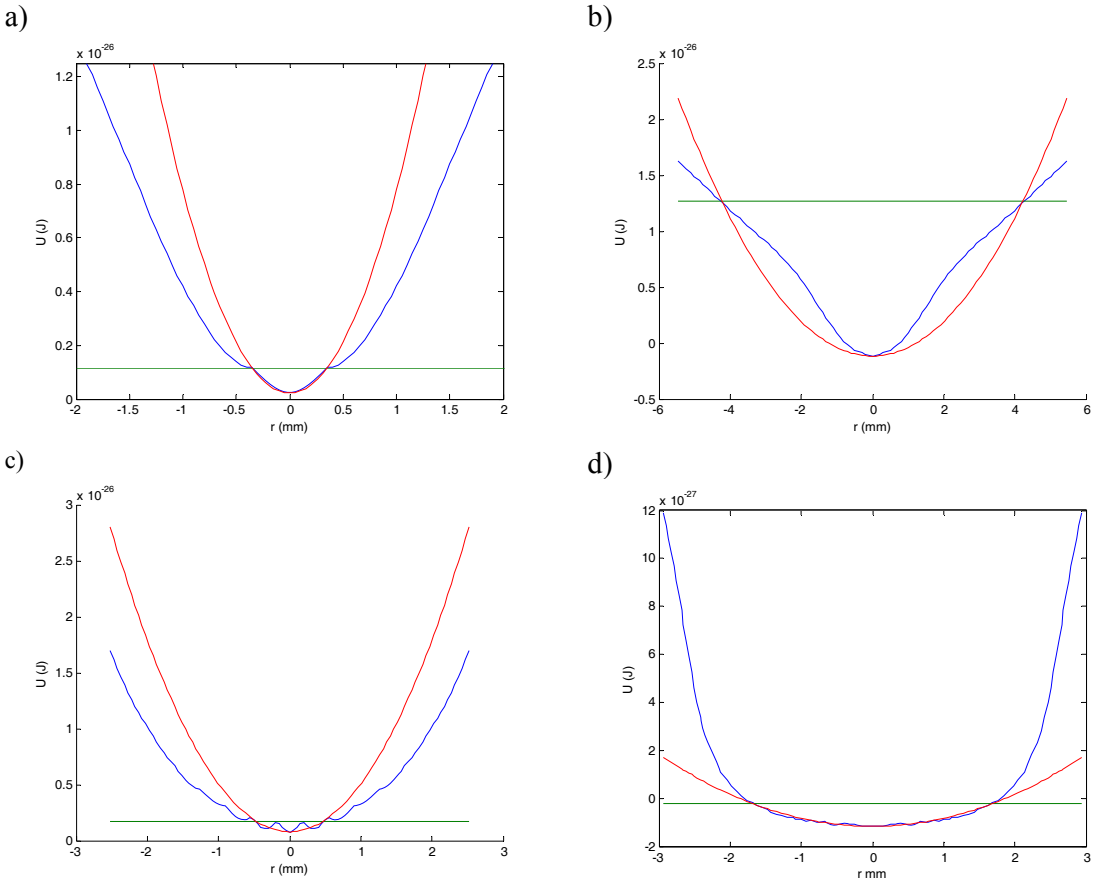

Figure 63 – Several problematic minimum energy paths. See text for details.

The MEP can also be used to calculate trap depth, by starting at the minimum point and following the MEP; the trap depth is the difference between the energy at the point where a (local) maximum is reached and the absolute minimum energy. The algorithm used must include safeguards to deal with cases of "jaggedness" as described above. However, since the grid uses a predefined space, the MEP may not have a maximum in that region. To avoid that, in this work (specifically, Chapter 5), I verified that the trap was at least as deep as one of several predefined values, rather than looking for the exact depth.

4.7 Conclusion

Simulations of magnetic fields are a powerful and highly important tool for the design and planning of magnetic trap experiments. We have developed several tools for the performance of these simulations.

Currently, the limitations of our programs and algorithms mostly stem from the fact that we can only calculate the field at a certain resolution. There is a practical limit to the

resolution we can achieve; while in theory, we could choose any resolution we desired, using too high a resolution narrows the extent of the calculated field to such a degree that we will see only a small portion of the "true" field; also, if we are not certain of the region which we desire to look at, we can miss it entirely. Increasing the resolution, while maintaining a large field of view, incurs computer memory limitations at some point.

We are currently working on alternative algorithms, ones which can work with very fine grids without being dependent on a certain region. These algorithms will allow us to obtain results that are more accurate and less prone to artifacts.

Another limitation of our simulations in their current incarnation is that they are limited to the effects of the magnetic field and gravity. Part of the improvements we need is to develop an algorithm which can take optical fields into account, and thus enabling us to simulate the trap at every stage.

5 Ioffe-Pritchard trap configurations

So far, I have mainly discussed the generation of MOTs. In this section, I will discuss and compare several different wire configurations for the creation of IP traps, to be used in latter phases of the experiment which require purely magnetic trapping. The design and simulation of these traps is the major focus of this thesis.

5.1 Criteria

When judging the viability of a design, there are several criteria which must be assessed:

1) Trap depth – the design must be capable of generating a trap of the desired depth. In graphical terms, an equipotential plot (see section 4.5) of the surface at the desired energy must result in a closed surface. As described in section 3.2.3, prior to loading into the IP trap, the atoms are cooled in an optical molasses. At the end of that stage, the atoms are in a cloud with a radius of the order of 1mm and at a temperature of 40μK, centered approximately 2mm from the chip – this is assumed to be our starting point. Ideally, the magnetic trap should have the same extension as the cloud (this is known as *mode matching*). An excessively steep trap will cause heating of the atoms as the cloud compresses during loading, while an insufficiently steep trap will cause expansion and hence loss of density of the cloud [7]. It is important to note that when the ensemble is at a given temperature, individual atoms have kinetic energies ranging far higher than the mean kinetic energy at that temperature (Boltzmann distribution). Should the trap depth be insufficient, these high-energy atoms will escape the trap. Therefore, as a rule of thumb, the desirable trap depth is ten times the temperature. Since the atoms may heat up considerably as they are compressed in the IP trap, we desire a trap depth of 1500 μK (the depth is expressed in ºK above the trap minimum).
2) A second escape channel for the atoms is by crashing into the chip surface. This can be seen graphically as an equipotential surface intersecting the chip surface. This creates a limitation on the attainable trap depth at a given height (or, put another way, on the range of heights attainable for a given trap depth); at small distances from the chip, the surface of the chip forms an obstacle to all but the tightest of traps.

3) There can be no zeros of the magnetic field within the closed surface; such zeros serve as escape channels for the trapped atoms by allowing Majorana transitions, as described in Chapter 2.
4) The potential must have a single minimum. Multiple minima can result in isolated traps within the desired region; however, these will be much shallower than the central minimum. Because of that, atoms may be trapped in them but prevented from cooling to the desired temperature. Such multiple minima appear in equipotential plots as multiple closed surfaces (which do not intersect). It should be noted that the secondary minima may occur outside the highest energy surface, in which case they can generally be ignored.

As noted previously, the trap forms below the chip in the experimental chamber. For clarity and ease of viewing, the situation is reversed in the graphs shown in this chapter (unlike in some of the previous discussions); the trap is above the chip, and "down" (i.e. the direction of gravity) is in the direction of positive-z.

Many of the current configurations (i.e. a collection of specific current settings on a given wire system) result in anharmonic traps. Therefore, the graphs will mainly discuss the trap width, which (for harmonic potentials at a given energy) is inversely proportional to the frequency (see section 4.6.2). The width used for the comparisons was the trap width at the energy of 150 μK; this energy is high enough to avoid most of the instabilities around the absolute minimum which may effect the calculation and low enough to avoid errors due to multiple minima (which, if the occur, typically appear at energies between 200-500 μK). Table 2 shows some frequencies and their corresponding trap widths (assuming the potential is harmonic)

frequency (Hz)	L_{150} (mm)
10	5.431259
20	2.715629
30	1.81042
40	1.357815
50	1.086252

Table 2 – Frequency→L

5.2 Configuration 1 – Z with side legs

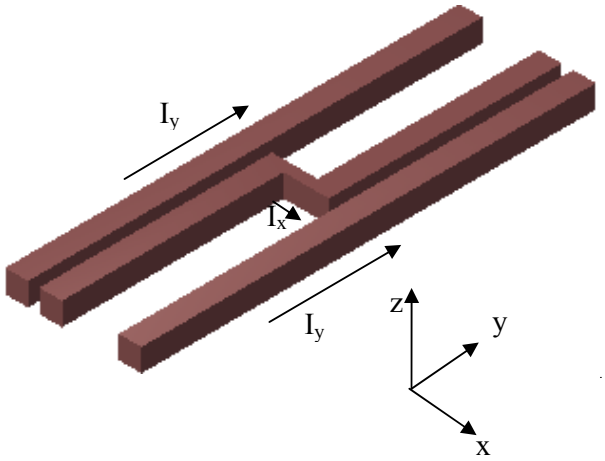

Figure 64 – Z with side legs

The first system we will examine is a variation on the Z-wire – a pair of legs are added, one either side (for this configuration only, the term "legs" will be used differently than was previously defined, referring to these additional wires rather than to those sections of the Z-wire parallel to the y axis), as seen in Figure 64. All the wires have a cross-section of 2x2mm except for the crosspiece (the section which lies in the x-direction), which has a width (in the y direction) of 1mm. The length of the crosspiece, measured between the centers of the Z's y-parallel sections, is 4mm. The surface of the chip is at z=0; since the chip is assumed to be 0.5mm thick, the center of the wire is at z=-1.5. The leads are not shown explicitly in the figure, but are taken into account in the simulations and calculations[42].

I_{II} (A)	h (±0.02mm)	Bias field (±0.1G)			Trap depth (μK)	$\bar{\theta}$ (º)	Error in $\bar{\theta}$	Trap width at 150 μK (mm)	Error in width (mm)
		B_{0x}	B_{0y}	B_{0z}					
-100	0.1	-21.84	66.80	0	250	10.21	1.35	0.95	0.03
-100	0.5	-16.83	46.55	0	1500	18.53	2.77	1.17	0.03
-100	1	-10.53	32.43	0	1500	28.85	2.06	1.52	0.03
-100	1.5	-4.87	23.81	0	1000	36.24	1.64	1.98	0.03
-75	0.1	-23.11	66.80	0	250	7.20	1.29	0.97	0.03
-75	0.5	-19.24	46.55	0	1000	14.74	2.61	1.18	0.03
-75	1	-14.10	32.43	0	1500	24.28	2.07	1.56	0.03
-75	1.5	-9.23	23.69	0	1000	32.62	1.57	2.03	0.07
-50	0.1	-24.39	66.80	0	250	4.50	1.27	0.99	0.03
-50	0.5	-21.65	46.55	0	1000	11.37	2.53	1.20	0.03
-50	1	-17.66	32.43	0	1500	21.28	1.95	1.61	0.03
-50	1.5	-13.68	23.69	0	1000	27.72	1.54	2.06	0.07
-25	0.1	-25.66	66.80	0	250	2.63	1.32	1.01	0.03
-25	0.5	-24.06	46.55	0	1000	7.78	2.53	1.27	0.03
-25	1	-21.23	32.43	0	1500	15.33	1.87	1.62	0.03

[42] The same is true for the other systems in this chapter as well.

-25	1.5	-18.13	23.69	0	500	22.16	1.52	2.07	0.07
0	0.1	-26.93	66.80	0	250	0.00	1.22	1.03	0.03
0	0.5	-26.47	46.55	0	1000	4.96	2.48	1.34	0.03
0	1	-24.70	32.18	0	1500	10.37	1.85	1.69	0.03
0	1.5	-22.51	23.56	0	500	16.97	1.51	2.09	0.07
25	0.1	-28.21	66.80	0	250	-3.56	1.15	1.08	0.03
25	0.5	-28.88	46.55	0	500	0.00	2.41	1.38	0.03
25	1	-28.24	31.93	0	1000	4.37	1.77	1.75	0.03
25	1.5	-26.92	23.44	0	1000	11.26	3.22	2.12	0.07
50	0.1	-29.48	66.80	0	250	-6.15	1.10	1.14	0.03
50	0.5	-31.29	46.55	0	500	-4.69	2.34	1.46	0.03
50	1	-31.80	31.93	0	500	0.00	1.71	1.86	0.03
50	1.5	-31.37	23.44	0	500	6.25	3.11	2.12	0.07
75	0.1	-30.76	66.80	0	150	-9.00	1.18	1.21	0.03
75	0.5	-33.70	46.55	0	500	-7.09	2.04	1.62	0.03
75	1	-35.37	31.93	0	500	-5.56	1.57	2.03	0.07
75	1.5	-35.78	23.19	0	500	-3.09	2.91	2.20	0.07
100	0.1	-32.03	66.80	0	150	-10.83	1.13	1.32	0.03
100	0.5	-36.11	46.55	0	250	-11.53	1.76	1.88	0.03
100	1	-38.94	31.93	0	250	-11.97	1.32	2.40	0.07
100	1.5	-40.23	23.19	0	250	-10.06	1.34	2.40	0.07

Table 3 – Z-trap data. See text for details of the columns.

As noted above, to achieve a deep trap, a high crosspiece current is necessary; the current used in these simulations was 60A. The bias fields (B_{0x}, B_{0y} and B_{0z}) were selected so that the magnetic field strength at the location of the potential minimum – which was, variously, set at heights of 0.1, 0.5, 1 and 1.5mm above the chip surface[43] - would be 1G, thus preventing atoms from escaping through Majorana transitions. The current in the legs was then varied, from -100A (current flowing in the negative-y direction) to 100A (current flowing in the positive-y direction), in steps of 25A.

Table 3 shows some of the calculated values for this configuration. I_y is the current in the legs, and h designates the distance of the potential minimum from the chip. Trap depth indicates the maximum energy for which a closed surface exists (we examine six energies and check which is the highest for which a closed surface exists; the energies in question are 67, 150, 250, 500, 1000 and 1500 μK). θ is the angle between the trap's longitudinal axis and the x axis (positive values indicate the longitudinal axis lying in the 1st and 3rd quadrants; negative values indicate the axis lies in the 2nd and 4th quadrants) Since the angle may change as the distance from the trap center grows (or, in other words, at higher-energy regions), as described in section 4.6.2, the values shown are the means of the angles calculated for the

[43] For B_{0z}=0, the trap is directly above the origin, which is the center of the Z-wire, due to trap symmetry (or almost so; there is a small z-component to the field due to the changes in current direction at the bends of the Z.

three lowest energies (the values of the angles for those energies – and usually for the higher ones - tend to be quite close).

Several trends can be seen in the data. First, the deepest traps exist only at intermediate distances from the chip surface – that is, energies of 1500 μK cannot be achieved at either h=0.1 or h=1.5 – and in any case, the deepest traps appear only when strong negative currents are used in the legs. It can be seen in Figure 65 that increasingly negative values of I_y decrease the trap width (that is, increase the frequency), thereby compressing the trap. At smaller distances from the chip, the effect of I_y on the trap width becomes more pronounced, and the maximum compression attainable also becomes significantly greater.

The currents also affect θ; as the current varies from -100A to 100A, the (absolute) angle decreases until it reaches 0 (at which point the longitudinal axis is parallel to the x axis) and then begins increasing again, as the field continues rotating (viewed from above – i.e. from positive z to the origin - as I_y goes from -100 to 100A, the longitudinal axis revolves in a clockwise direction).

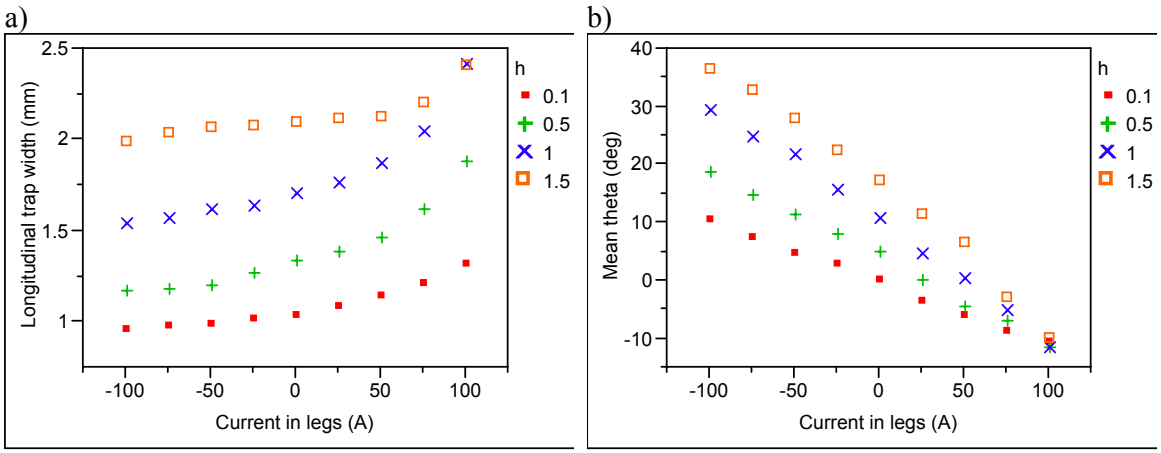

Figure 65 – Effect of changing I_y on trap parameters. Trap width is calculated at 150 μK.

5.3 Configuration 2 – H-wire

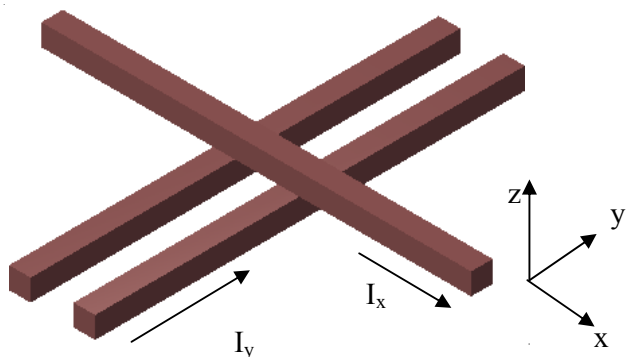

Figure 66 – H-wire

Figure 66 shows the second system under consideration – an H-trap. The wires here have a cross section of 1x1mm, with lengths of 40mm. Three separations between the legs were examined – 6, 8 and 10mm.

Because, unlike the Z-wire, the system is symmetric around the y axis, the behavior of the field is likewise symmetric (Figure 67[44]) with respect to I_y. As the current approaches zero, the trap becomes more and more elongated, until at zero there is no longitudinal confinement and the trap becomes a side guide parallel to the crosspiece.

The crosspiece current affects the frequency as well as the angle of rotation. Trap width declines with increasing crosspiece current; the effect is more pronounced for H-wires with small separations between the legs. Decreasing crosspiece current causes the angle to increase until it reaches ±90º at 0 current, at which point the H becomes a two-wire guide (though this would mean the atoms would crash into the chip; as the currents are co-propagating, the guide's minimum is directly between the legs). In addition, high crosspiece currents are required to achieve deep traps.

[44] It should be noted that the data for the 0.1mm height was omitted from some of the graphs. This is because in the H-wire, the data was particularly vulnerable to the instability issues described in section 4.6.2.

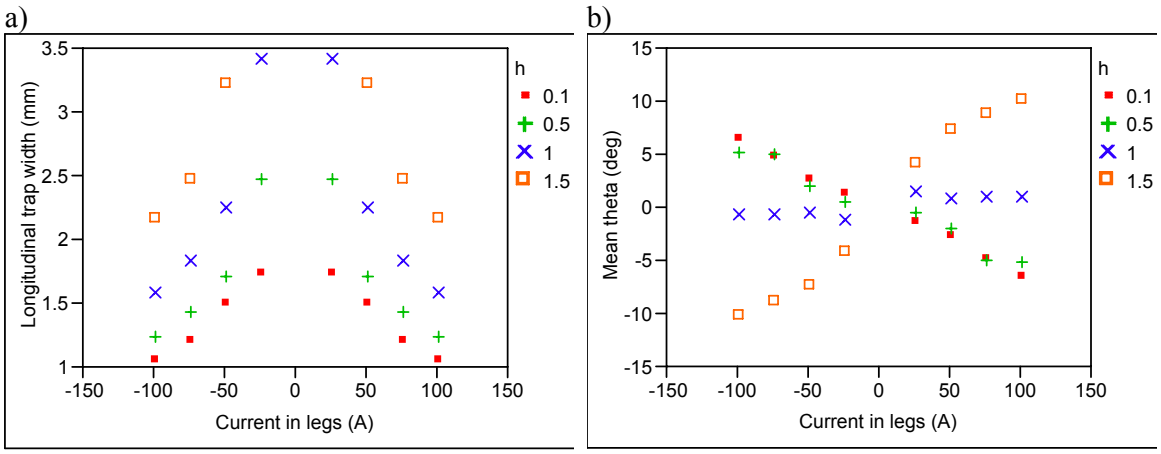

Figure 67 – Longitudinal trap width (trap width is calculated at 150 μK) and angle of rotation as a function of I_y (crosspiece current equals 60A, separation between legs is 6mm).

The separation of the legs also has an effect on the trap width (Figure 68). At small separations, trap widths are smaller, while the angle of the field changes significantly as the trap height above the chip changes. Trap height also affects the trap width; traps are narrower closer to the surface.

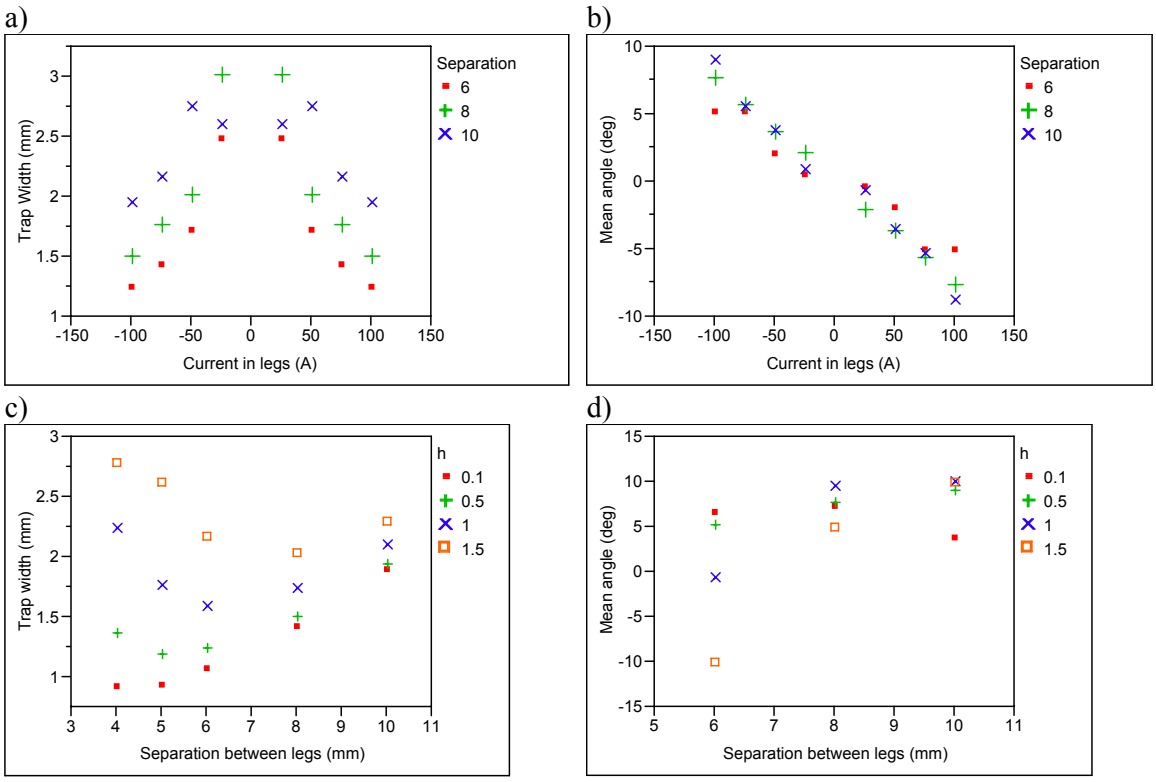

Figure 68 – Alteration of longitudinal trap width (trap width is calculated at 150 μK) and angle of rotation for different separations between the H legs. Crosspiece current is 60A; In a and b, the height is 0.5mm above the chip, while in c and d the leg current is -100A

It can be seen (Figure 68c) that for each height, there is a separation which will give a minimal trap width (or, put another way, for each separation of the legs there is an optimum height where the frequency is maximal). This separation is such that the distance between the

given height above the chip and the plane in which the legs lie is exactly half the separation. At this point, the IP field has its maximal value (see section 2.1.3.5).

Compared to the Z-wire, the H-trap has a weaker longitudinal confinement. However, the H-trap allows considerably more leeway in terms of the maximum height at which a deep (depth>1500 μK) trap can be established, in terms of the usable crosspiece currents and distances from the chip. It is still extremely difficult to achieve a deep trap at very close distances to the chip – largely because that region of the trap intersects the chip – but with the H it is possible to create a deep trap at relatively larger heights than with the Z.

Figure 69 shows several different current configurations for the Z- and H-traps at two heights. Plots (a), (b) and (c) show the field with the minimum at 0.5mm above the chip, while it is 1mm above the chip in the other three graphs.

It can be seen that the H-trap produces weaker longitudinal confinement than the Z-trap, and that the 10mm-long H provides weaker confinement than the 6mm H. However, the 10mm H-wire can provide a greater depth, by "pinching off" the energy "channels" leading to the chip surface (when looking at the figure, it should be kept in mind that the legs are at x=±3mm for the 6mm H and x=±5mm for the 10mm H).

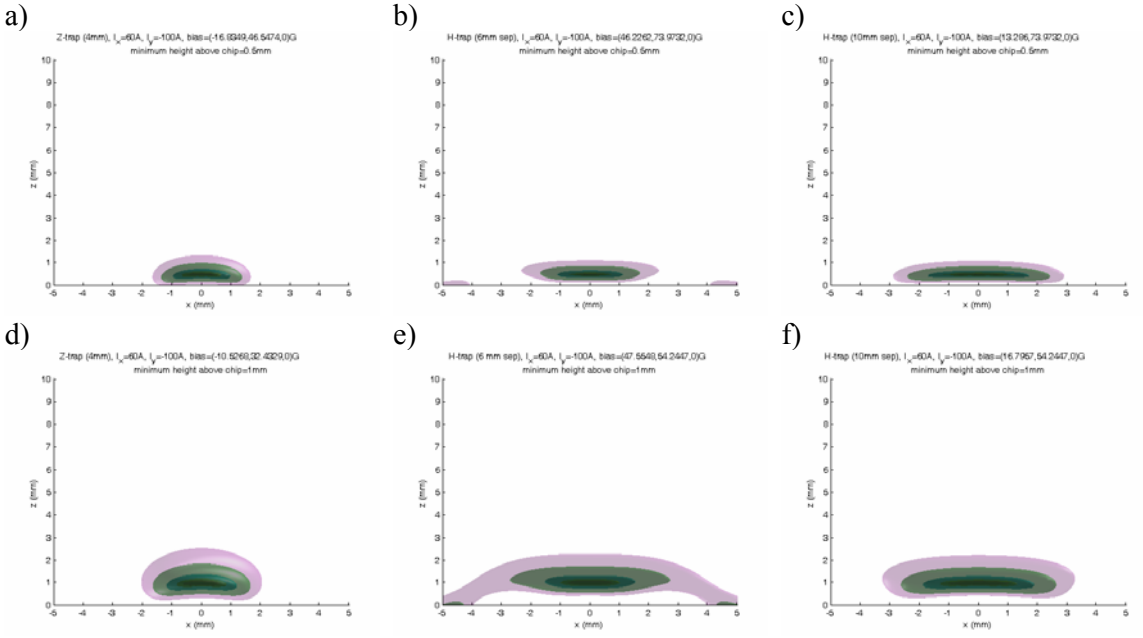

Figure 69 – Equipotential surfaces for the Z- and H-traps. The concentric black, red, yellow, cyan, green and magenta surfaces represent temperatures of 67, 150, 250, 500, 1000 and 1500 μK respectively (the colors of some of the inner shells may appear different in the actual graphs since they are being viewed through other surfaces with a different color). The two leftmost graphs are the (4mm-long) Z-wire, the middle graphs are for an H with 6mm separation between the legs, and the rightmost graphs are for an H with 10mm separation between the legs. In plots a-c the potential minimum is 0.5mm above the chip, while it is at 1mm above the chip in plots d-f.

There is a certain degree of interplay between the crosspiece current, the current in the legs, and the maximum attainable depth. At high crosspiece currents, maximum depth is achieved for high leg currents. If the crosspiece current is dropped somewhat, lower leg currents are required (otherwise contact is made with the chip surface).

Separation of legs (mm)	I_x (A)	I_y (A)	h (±0.02)	Bias field (±0.1G)			Trap depth (μK)	$\bar{\theta}$ (°)	Error in $\bar{\theta}$	Trap width at 150 μK (mm)	Error in width (mm)
				B_{0x}	B_{0y}	B_{0z}					
6	45	-100	0.5	46.23	55.48	0	1500	6.34	2.57	1.61	0.03
8	45	-100	0.5	25.88	55.48	0	1500	11.31	2.03	2.05	0.03
10	45	-100	0.5	13.29	55.48	0	1000	10.55	1.61	2.65	0.07
6	45	-100	1	47.55	40.68	0	1500	-0.91	2.01	2.10	0.03
8	45	-100	1	29.16	40.68	0	1500	11.28	1.83	2.27	0.03
10	45	-100	1	16.80	40.68	0	1000	15.31	1.42	2.86	0.07
6	45	-100	1.5	47.03	32.02	0	1500	-14.05	1.40	3.05	0.07
8	45	-100	1.5	30.94	31.77	0	1000	7.23	1.56	2.63	0.07
6	45	-75	0.5	34.42	55.48	0	1000	4.42	0.87	1.86	0.03
8	45	-75	0.5	19.16	55.48	0	1500	9.36	1.84	2.26	0.03
10	45	-75	0.5	9.71	55.48	0	1500	7.74	1.39	2.94	0.07
10	45	-75	1	12.35	40.68	0	1000	9.63	2.76	3.15	0.07
10	45	-50	0.5	6.14	55.48	0	1500	5.91	1.16	3.47	0.07
10	45	-50	1	7.90	40.68	0	1000	6.83	2.23	3.75	0.07
10	45	50	0.5	-6.14	55.48	0	1500	-5.91	1.16	3.47	0.07
10	45	50	1	-7.90	40.68	0	1000	-6.83	2.23	3.75	0.07
6	45	75	0.5	-34.42	55.48	0	1000	-4.42	0.87	1.86	0.03
8	45	75	0.5	-19.16	55.48	0	1500	-9.36	1.84	2.26	0.03
10	45	75	0.5	-9.71	55.48	0	1500	-7.74	1.39	2.94	0.07
10	45	75	1	-12.35	40.68	0	1000	-9.63	2.76	3.15	0.07
6	45	100	0.5	-46.23	55.48	0	1500	-6.34	2.57	1.61	0.03
8	45	100	0.5	-25.88	55.48	0	1500	-11.31	2.03	2.05	0.03
10	45	100	0.5	-13.29	55.48	0	1000	-10.55	1.61	2.65	0.07
6	45	100	1	-47.55	40.68	0	1500	0.91	2.01	2.10	0.03
8	45	100	1	-29.16	40.68	0	1500	-11.28	1.83	2.27	0.03
10	45	100	1	-16.80	40.68	0	1000	-15.31	1.42	2.86	0.07
6	45	100	1.5	-47.03	32.02	0	1500	14.05	1.40	3.05	0.07
8	45	100	1.5	-30.94	31.77	0	1000	-7.23	1.56	2.63	0.07
6	60	-100	0.5	46.23	73.97	0	1500	5.15	2.57	1.60	0.03
8	60	-100	0.5	25.88	73.97	0	1500	7.64	2.18	1.96	0.03
10	60	-100	0.5	13.29	73.97	0	1500	8.94	1.60	2.57	0.03
6	60	-100	1	47.55	54.24	0	1000	-0.91	2.01	2.07	0.03
8	60	-100	1	29.16	54.24	0	1000	9.36	1.84	2.24	0.03
10	60	-100	1	16.80	54.24	0	1500	9.84	3.23	2.61	0.07
6	60	-100	1.5	47.03	42.61	0	1000	-10.20	1.44	2.95	0.07
10	60	-100	1.5	19.30	42.36	0	1000	9.91	2.83	2.99	0.07
6	60	-75	0.5	34.42	73.97	0	1000	5.08	2.53	1.86	0.03
8	60	-75	0.5	19.16	73.97	0	1000	5.70	1.85	2.22	0.03
10	60	-75	0.5	9.71	73.97	0	1500	5.44	1.58	2.87	0.07
10	60	-75	1	12.35	54.24	0	1500	8.34	2.67	3.09	0.07
10	60	-75	1.5	14.23	42.36	0	1000	7.53	2.47	3.39	0.07
10	60	-50	0.5	6.14	73.97	0	1500	3.66	1.19	3.41	0.07
10	60	-50	1	7.90	54.24	0	1000	5.38	2.16	3.68	0.07

10	60	50	0.5	-6.14	73.97	0	1500	-3.66	1.19	3.41	0.07
10	60	50	1	-7.90	54.24	0	1000	-5.38	2.16	3.68	0.07
6	60	75	0.5	-34.42	73.97	0	1000	-5.08	2.53	1.86	0.03
8	60	75	0.5	-19.16	73.97	0	1000	-5.70	1.85	2.22	0.03
10	60	75	0.5	-9.71	73.97	0	1500	-5.44	1.58	2.87	0.07
10	60	75	1	-12.35	54.24	0	1500	-8.34	2.67	3.09	0.07
10	60	75	1.5	-14.23	42.36	0	1000	-7.53	2.47	3.39	0.07
6	60	100	0.5	-46.23	73.97	0	1500	-5.15	2.57	1.60	0.03
8	60	100	0.5	-25.88	73.97	0	1500	-7.64	2.18	1.96	0.03
10	60	100	0.5	-13.29	73.97	0	1500	-8.94	1.60	2.57	0.03
6	60	100	1	-47.55	54.24	0	1000	0.91	2.01	2.07	0.03
8	60	100	1	-29.16	54.24	0	1000	-9.36	1.84	2.24	0.03
10	60	100	1	-16.80	54.24	0	1500	-9.84	3.23	2.61	0.07
6	60	100	1.5	-47.03	42.61	0	1000	10.20	1.44	2.95	0.07
10	60	100	1.5	-19.30	42.36	0	1000	-9.91	2.83	2.99	0.07

Table 4 – selected parameter values for the H-wire

5.4 Configuration 3 – Inverted H-wire

Figure 70 – Inverted H-wire

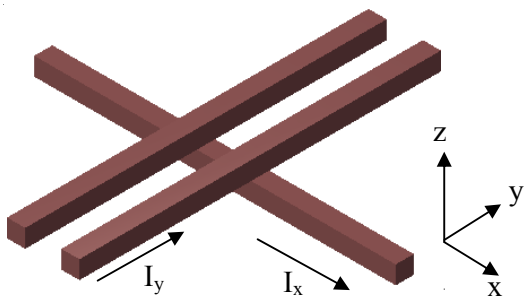

In addition to the H-wire, we also examined another variant of it – the inverted H. In this configuration, the legs of the H are *above* the crosspiece, rather than below it (all other dimensions are the same as for the normal H). The intent was to try to improve the longitudinal confinement by moving the legs closer to the trapping region.

In practice, the opposite occurred. This is because moving the legs up requires moving the crosspiece down – in other words, increasing the distance between the crosspiece and the trap. This has a detrimental effect on both the attainable longitudinal frequencies – which are lower than those obtained for a normal H – and on the trap depth. The deepest traps are obtained for values of I_y which are closer to zero than in the normal H. Throughout the simulations' parameter space, I was unable to find a set of currents which yielded a trap depth greater than 500μK.

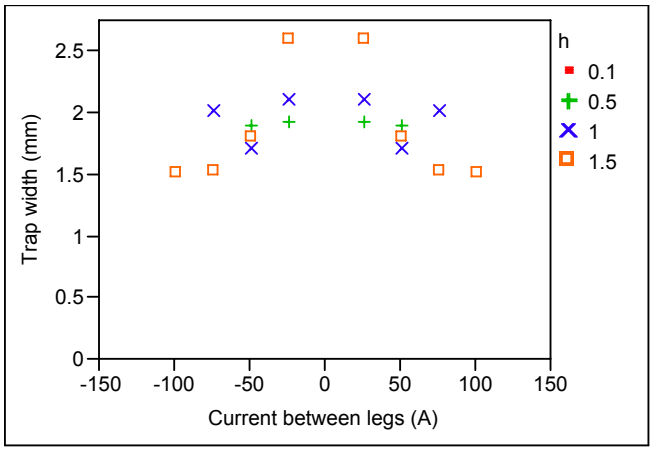

Figure 71 – Effect of I_y on longitudinal trap width of inverted H-wire. Longitudinal trap width is calculated at 150 μK.

As in the case of the normal H, reducing the separation between the legs decreases the trap width.

Separation of legs (mm)	I_x (A)	I_y (A)	h (±0.02)	Bias field (±0.1G)			Trap depth (μK)	$\bar{\theta}$ (°)	Error in $\bar{\theta}$	Trap width (mm)	Error in width (mm)
				B_{0x}	B_{0y}	B_{0z}					
10	45	-75	1.50	9.85	21.11	0	500	42.54	0.59	5.24	0.14
10	45	75	1.50	-9.85	21.11	0	500	-42.54	0.59	5.24	0.14
10	60	-100	1.50	13.50	28.19	0	500	42.72	0.61	4.89	0.07
10	60	100	1.50	-13.50	28.19	0	500	-42.72	0.61	4.89	0.07
8	60	-100	1.50	26.10	28.19	0	500	47.46	0.86	4.50	0.07
8	60	100	1.50	-26.10	28.19	0	500	-47.46	0.86	4.50	0.07
10	60	-25	1.50	2.57	28.81	0	500	11.45	1.60	3.88	0.07
10	60	25	1.50	-2.57	28.81	0	500	-11.45	1.60	3.88	0.07
10	60	-25	1.00	1.41	34.45	0	500	11.42	1.71	3.78	0.07
10	60	25	1.00	-1.41	34.45	0	500	-11.42	1.71	3.78	0.07
10	60	-25	0.50	-0.03	42.36	0	500	9.19	1.63	3.73	0.07
10	60	25	0.50	0.03	42.36	0	500	-9.19	1.63	3.73	0.07
8	60	-25	1.50	5.72	28.81	0	500	10.53	2.06	3.07	0.07
8	60	25	1.50	-5.72	28.81	0	500	-10.53	2.06	3.07	0.07
8	45	-25	1.00	4.46	25.59	0	500	17.60	1.06	2.96	0.07
8	45	25	1.00	-4.46	25.59	0	500	-17.60	1.06	2.96	0.07
8	60	-25	1.00	4.43	34.45	0	500	13.24	1.09	2.83	0.07
8	60	25	1.00	-4.43	34.45	0	500	-13.24	1.09	2.83	0.07
8	60	-25	0.50	2.59	42.36	0	500	12.55	1.11	2.81	0.07
8	60	25	0.50	-2.59	42.36	0	500	-12.55	1.11	2.81	0.07
6	60	-25	1.00	9.74	34.45	0	500	10.72	1.50	2.09	0.07
6	60	25	1.00	-9.74	34.45	0	500	-10.72	1.50	2.09	0.07
6	60	-25	0.50	7.66	42.11	0	500	14.73	1.68	1.92	0.03
6	60	25	0.50	-7.66	42.11	0	500	-14.73	1.68	1.92	0.03
6	60	-50	1.50	22.62	28.69	0	500	8.63	1.69	1.80	0.03

Table 5 – selected values for the inverted H

The behavior of the longitudinal trap width is somewhat different in this case. In the normal H, the trap width is small at high (absolute) values of I_y and increases as zero is approached. In the inverted H, the width is relatively high at the highest currents, and then, as

I_y is adjusted towards zero, reaches a minimum and then starts increasing (as can be seen in Figure 71 for h=1mm; presumably, we do not see the drop in frequency for the lower heights because the jumps between values of I_y are too large).

5.5 Configuration 4 – The X-trap

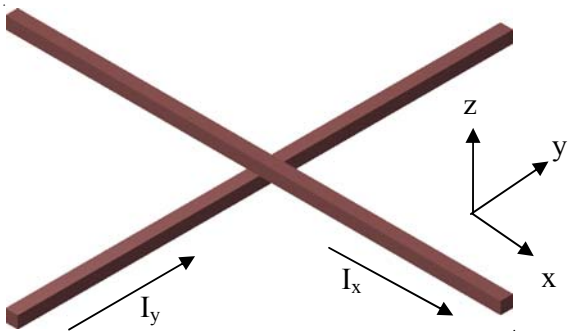

Figure 72 – The X-wire trap

The X-trap is a simple structure, composed of two perpendicular wires, one of which – the crosspiece[45] - is above (closer to the chip) the other.

In the case of the X-wire, deep traps tend to be obtained for intermediate absolute values of I_y. Similarly, at those intermediate values, the traps will be narrowest. It appears that the optimum height is at $I_x=I_y$. For such currents, the traps are quite narrow – narrower than for any of the other systems we examine here.

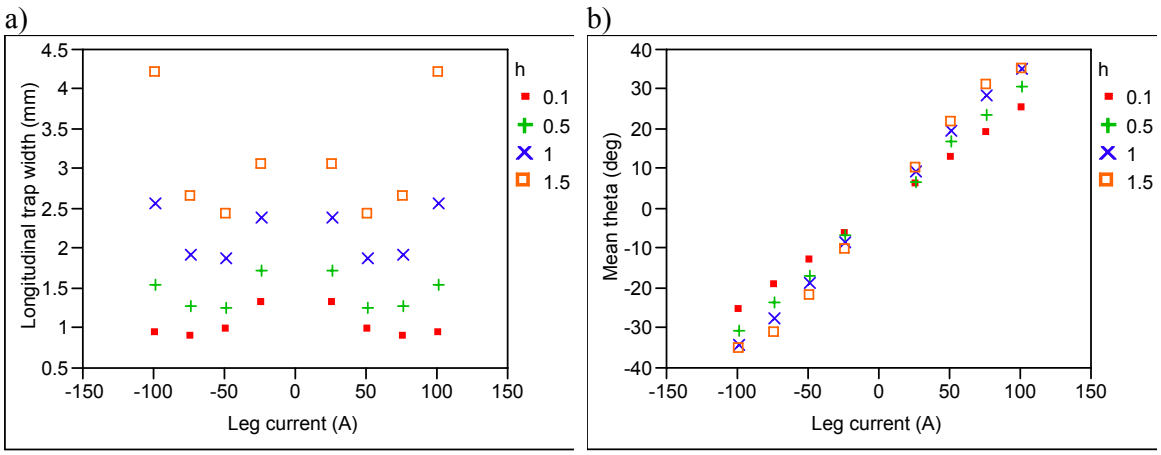

Figure 73 – Trap width (measured at 150 μK) and angle of rotation for the X-trap

For weak current in the leg, the X-trap tends to be highly elongated (if either of the currents becomes zero, the wire becomes a side guide). In the vicinity of the optimum point,

[45] The X-wire doesn't have a crosspiece in the sense that the Z- and H-wires do; here, "crosspiece" is defined as the wire parallel to the x axis and "leg" is the wire parallel to the y axis. I will continue to use the notation of $I_{\parallel}$ for the current in the (single) leg for consistency.

the trap has the ellipsoid shape typical of most of the traps. As the current increases past the optimum, however, the trap begins curving drastically towards the surface.

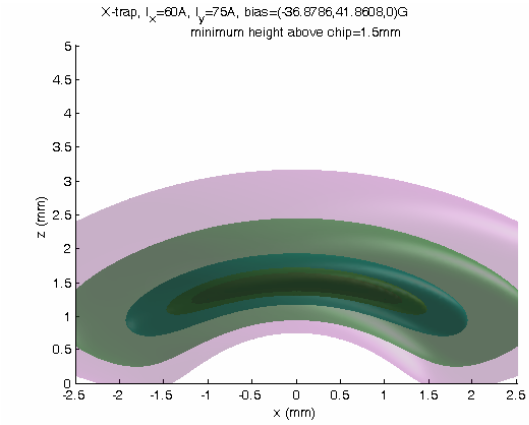

Figure 74 – X-trap at high current

I_x (A)	I_y (A)	h (±0.02)	Bias field (±0.1G)			Trap Depth (μK)	$\bar{\theta}$ (º)	Error in $\bar{\theta}$	Trap width (mm)	Error in width (mm)
			B_{0x}	B_{0y}	B_{0z}					
30	-25	0.5	18.65	36.99	0.00	1000	-14.68	1.71	1.93	0.03
30	25	0.5	-18.65	36.99	0.00	1000	14.68	1.71	1.93	0.03
45	-50	0.5	36.30	55.48	0.00	1000	-20.49	2.25	1.45	0.03
45	50	0.5	-36.30	55.48	0.00	1000	20.49	2.25	1.45	0.03
45	-25	0.5	18.65	55.48	0.00	1000	-9.93	1.80	1.77	0.03
45	25	0.5	-18.65	55.48	0.00	1000	9.93	1.80	1.77	0.03
45	-50	1	29.67	40.43	0.00	1000	-24.91	1.48	2.11	0.07
45	50	1	-29.67	40.43	0.00	1000	24.91	1.48	2.11	0.07
45	-50	1.5	24.94	31.40	0.00	1000	-27.39	1.12	2.81	0.07
45	50	1.5	-24.94	31.40	0.00	1000	27.39	1.12	2.81	0.07
60	-50	0.5	36.30	73.97	0.00	1500	-16.92	2.61	1.25	0.03
60	50	0.5	-36.30	73.97	0.00	1500	16.92	2.61	1.25	0.03
60	-75	0.5	53.95	73.97	0.00	1000	-23.66	2.75	1.27	0.03
60	75	0.5	-53.95	73.97	0.00	1000	23.66	2.75	1.27	0.03
60	-25	0.5	18.65	73.97	0.00	1000	-6.52	1.90	1.73	0.03
60	25	0.5	-18.65	73.97	0.00	1000	6.52	1.90	1.73	0.03
60	-50	1	29.71	54.24	0.00	1500	-19.02	1.68	1.86	0.03
60	50	1	-29.71	54.24	0.00	1500	19.02	1.68	1.86	0.03
60	-75	1	43.92	53.74	0.00	1500	-28.05	1.66	1.90	0.03
60	75	1	-43.92	53.74	0.00	1500	28.05	1.66	1.90	0.03
60	-50	1.5	24.98	42.11	0.00	1000	-21.61	1.30	2.44	0.07
60	50	1.5	-24.98	42.11	0.00	1000	21.61	1.30	2.44	0.07
60	-75	1.5	36.88	41.86	0.00	1500	-31.06	1.21	2.67	0.07
60	75	1.5	-36.88	41.86	0.00	1500	31.06	1.21	2.67	0.`07

Table 6 – some selected parameter values for the X-trap

5.6 Configuration 5 – Inverted X-trap

The final system we will examine here is similar to the X-trap; except that here, the crosspiece is under the leg rather than over it.

Figure 75 – The inverted X-trap

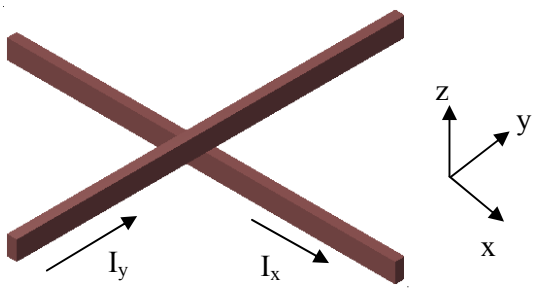

Of all the traps examined in this chapter, the inverted X-trap was the most troublesome to simulate. The algorithm we used to calculate the requisite bias fields was incapable of deriving results for most of the current configurations, leaving us with a paucity of data to analyze. What little is available, however, shows an interesting possibility – this is the only trap of those examined which indicated the possibility of forming of a deep (~1000 μK) trap at a height of 0.1mm above the chip, in both compressed and elongated formations. Should this prove to be viable, this would allow both trapping of atoms very close to the chip surface as well as the possibility to transport them at low heights, from one area of the chip to another. It should also be remembered that the X- and inverted X-traps are identical structures except that they are rotated at 90º relative to one another – which means that an X-trap can be converted into an inverted X-trap simply by changing the bias fields.

5.7 Discussion and conclusions

In the sequence of the experiment, the IP magnetic trap is used to catch the atoms after they have been cooled by optical molasses, and then to compress them (and, afterwards, to hold them during evaporative cooling). Therefore, our chosen trap configuration must be able to encompass the volume of the optical molasses and to be compressed while retaining its depth in order to create a cloud density sufficient for evaporative cooling (the cloud needs to be dense enough to thermalize), and eventually move closer to the chip in order to load the traps formed by the currents on the chip itself.

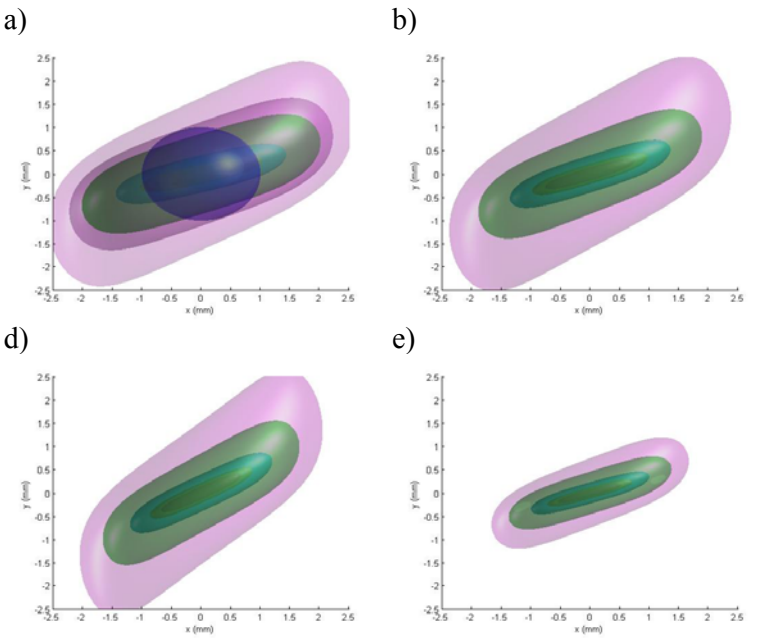

Figure 76 – Loading sequence for a Z-trap. In (a-d) the potential minimum is at 1mm over the chip, while in (e) it is 0.5mm over the chip. See text for further details.

Figure 76 shows a possible sequence for loading and compressing the trap (the colors indicate the temperatures as in Figure 69 - black→67 μK, red→150 μK, yellow→250 μK, cyan→500 μK, green→1 mK, magenta→1.5 mK; in addition, the dark purple surface in (a) represents a temperature of 1.2 mK). Initially, the trap is generated with a current of 60A in the crosspiece and -25A in the legs. This gives a deep trap with a relatively large extent at a height of 1mm above the chip (a), large enough to encompass the cloud left by the molasses (represented in the figure by a blue sphere) which, as noted before, is at a temperature of 40 μK. As the current in the legs is slowly increased (b-d), the trap becomes smaller, compressing the atom cloud. Finally, when a current of -100A is reached in the legs, the bias field in the x and y axes is increased, lowering the trap to 0.5mm above the chip and compressing it considerably, while maintaining its depth.

As mentioned above, the IP field must compress the field sufficiently to enable evaporative cooling. This usually means a longitudinal frequency on the order of tens of Hz and a transverse frequency of several hundred Hz. This translates into a longitudinal extent (as per Table 2) of approximately 1.8 mm or less, and a transverse extent of approximately 0.1mm (in both cases at the 150 μK energy).

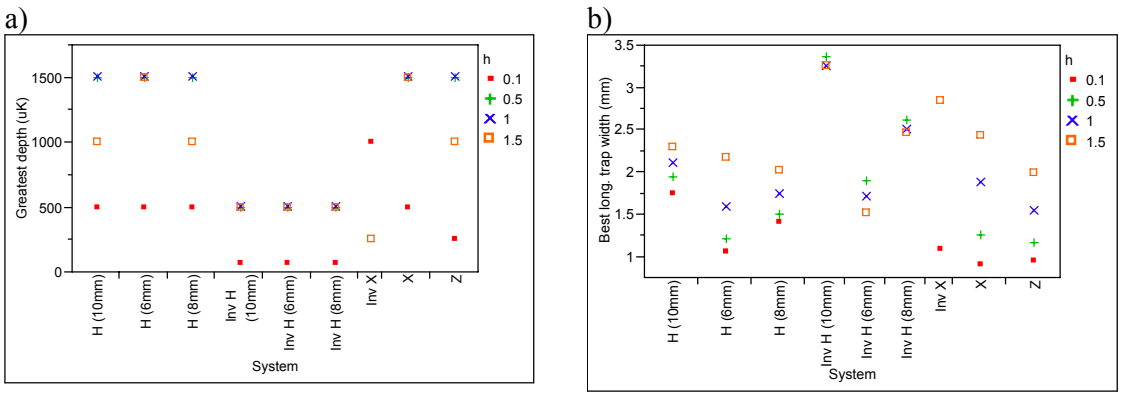

Figure 77 – Best trap depths and longitudinal trap widths (at 150 μK) for each system. "Inv" refers to the inverted versions.

Figure 77 shows the best attainable longitudinal trap widths and depths for each system. We are interested in a trap at a height of 0.5mm over the chip; as can be seen from (a), the inverted H-wires do not generate trap depths of over 500 μK at that height (we do not have a result at all for the inverted X at that height). Looking in (b) at the other systems, the Z-trap gives the best (smallest) width at that height, followed by the 6mm H- and X-traps (corresponding to frequencies of approximately 43-46 Hz).

System		Z-trap (4mm long) with legs	X-trap	H-trap (6mm separation)
I_x (A)		60	60	45
I_y (A)		-100	-50	±100
Bias Field (G)	B_{0x}	-16.83	-36.3	∓46.22
	B_{0y}	46.55	73.97	55.48
	B_{0z}	0	0	0
Longitudinal frequency (Hz)		46.59	43.43	44.82
Transverse frequency (Hz)		371.13	432.07	283.9
Z-transverse frequency (Hz)		367.48	471.55	346.02
Trap depth (μK)		1469	1941	1714

Table 7 – Selected frequencies for three cases

Table 8 includes frequencies for the longitudinal, transverse, and Z-transverse (the latter two are the transverse frequencies in the xy plane and the z axis, respectively)[46] for the best three cases from Figure 77b, at a height of 0.5mm over the chip. The frequencies were

[46] The transverse and Z-transverse frequencies were calculated with a variant of the MEP technique used for the longitudinal frequency and described in section 4.6.2, based on finding the maximum energy path in the vicinity of the minimum.

calculated by fits at 150 μK above the minimum energy. Due to the fact that the traps are anharmonic, there is a significant error (~20%) in the frequency, but these figures may be seen as indicative. It can be seen that, on the whole, the X-trap gives the best frequencies, followed by the Z- and the H-traps, though the Z-trap gives the best longitudinal frequency.

The next mission for the magnetic trap is to move atoms to closer to the chip, where they can be loaded into traps generated by wires on the chip itself.

a) b) c)

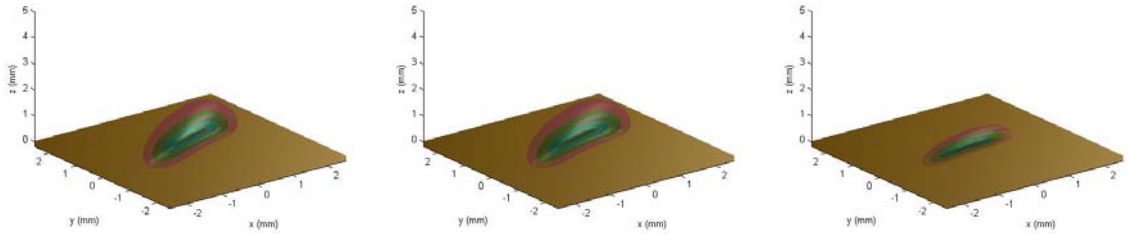

Figure 78 – Loading with a magnetic trap (using the Z-wire). The gold surface represents the surface of the chip. In a-b, the potential minimum is 0.5mm over the chip, while in c it is 0.1mm over the chip.

Figure 78 shows one such loading sequence. The atoms start in a deep, compressed trap such as that in Figure 76e. By increasing the bias field, the trap is lowered in the z axis towards the chip. Eventually, its outer layers (higher energies) will hit the chip. However, the trap will still be deep enough to retain the cooler atoms; if the atom ensemble was cold to begin with, most of the atoms will survive the move.

As noted above, the X-trap is the most competitive with the Z-trap (while the H-trap gives the best frequencies at 0.5mm above the chip, it is considerably less effective at 0.1mm). Under certain conditions, it can give a tighter trap than the Z. As well, the X-trap opens the potential possibilities of the inverted X. However, the X-trap has significant drawbacks. While it can achieve tighter traps than the Z, it generally encounters a trade-off between depth and trap width (i.e. frequency and volume), while the Z can achieve traps which are both deep and narrow (as in Figure 76e).

Another drawback of the X-trap is that it generally requires considerably stronger bias fields than the Z-trap (by a factor of 2, in some cases). These can be difficult to generate.

In the end, the question of which trap is preferable is determined by the requirements of the user. For traps suitable for compressed confinement, the Z-trap (with the addition of legs) is preferable. However, if trap volume (and hence increased atom number) is the overriding concern, an H-trap is often preferable especially if deep traps are required at large distances from the chip. In the case of the experiments currently in our lab, the Z-trap, based on the data

in this work, appears to be the best choice because stronger compression is more important for achieving the highest number densities – the starting point for BEC – in the trap.

One possibility to reconcile these various capabilities is to create a system which can function as several different traps. One such possible system is shown in Figure 79 – depending on where the current is connected, it can serve as either a Z (with legs that are not shown) or an X. Another possibility is an H with an extra two legs, one to either side – there are indications [53] this can considerably improve the H's trapping ability.

Figure 79 – Combined Z and X-trap (proposed)

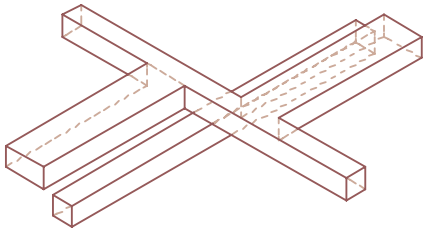

6 Summary and Conclusions

This thesis describes three aspects of interactions of magnetic fields with ultracold atoms, and their use in trapping and cooling such atoms. First, I discuss principles for the design and construction of the system currently in use in our laboratory. Implementing the magnetic micro-traps required for our atom chip experiments necessitated developing expertise for component design, assembly, and atom chip mounting and bonding. Familiarity with atom chip fabrication and experimentation was also gained.

The second aim of this work was to accurately simulate the magnetic fields of the micro-trap that we have constructed, and to enable the evaluation and characterization of alternative designs. Accurate simulations of the field are critical in order to achieve good traps, while inaccurate simulations can be very costly, both financially and in terms of lost time and effort. Achieving the requisite accuracy entails developing sufficiently precise numerical techniques and algorithms to overcome the limitations inherent in the finite availability of computational time and memory. While similar limitations have been overcome by many other laboratories studying ultracold atoms, our simulations were also designed to allow optimization of the magnetic trap parameters during the experiments in real time. This required significantly faster computational methods, which we have now implemented without compromising the accuracy of their results.

Two “families” of techniques for simulations have been developed. The first is based on analytical equations for the various types of magnetic traps. The second applies numerical techniques for modeling a greater variety of traps, since the analytical analyses are often limited to general considerations for idealized cases.

There is still much work to be done on these techniques. We are currently working on developing a set of algorithms (and from them, computer programs) for characterizing the important parameters of a given trap, i.e., its size, frequencies, depth, shape, etc. Systematic analysis of such trap parameters is being used both to design improved traps, and to improve the experimental sequences used for manipulating the ultracold atoms. In addition, we are adding the simulation of optical forces to improve the operation of the MOT and optical molasses stages, thus enabling simulation of the entire experiment.

Finally, these simulation techniques have been applied to characterize and compare several variants of magnetic micro-traps. Since such variants require different mechanical construction, the choice of trap is very important: a trap optimized for some experiments may not be optimum for others (e.g., in terms of trap frequency or depth). The results of this analysis indicate that the best overall results are generated by the conventional Z-trap,

modified by adding a pair of parallel wires. This trap is quite versatile, allowing control over trap frequencies that range high enough for use in evaporative cooling, the last remaining step for achieving Bose-Einstein condensation. The modified Z-trap also allows the trap minimum to be moved very close to the chip, allowing efficient loading of the magnetic traps generated by wires on the atom chip itself. The simulations also show that some of the other traps should perform better in specific circumstances, suggesting that it may be worthwhile to examine a combined trap, e.g., as shown in Figure 79.

Appendix A Coil-less Trapping

The trapping schemes described in this chapters all require an external, homogeneous (in an ideal case) bias field to generate the trap. In the systems described in Chapter 3, that bias field is generated by a pair of coils placed on either side of the vacuum chamber on each axis. However, these have disadvantages similar to those of the coil-generated traps described in sections 2.1.1 and 2.1.2 – The worst of which is that due to their bulk they restrict optical access to the vacuum chamber - making it more difficult to, e.g., place lasers for cooling or imaging. In addition, they are bulky, and suffer from large heat dissipation and rise times.

In this addendum, I will briefly describe a proposed mount design to generate traps without the use of external coils for the bias fields. While coils may still be required to compensate for unwanted external fields, those coils are both less bulky and can be placed at a large distance from the vacuum chamber, as the fields required are small (they may also simply be replaced by passively screening external fields with mu-metal).

A.1 Basic Concept

The concept behind the coil-less MOT is to use several parallel copper rods beneath the copper structures to generate a field which is roughly homogenous in the region where the MOT is desired. While a single wire has a circular magnetic field profile, adding additional parallel wires "flattens out" the field (a broad plate would also do so, but would allow only limited adjustment of the field, since the current through the plate is uniform). Figure 80 shows a schematic of the positioning of the arches relative to the U-wire and the atom chip.

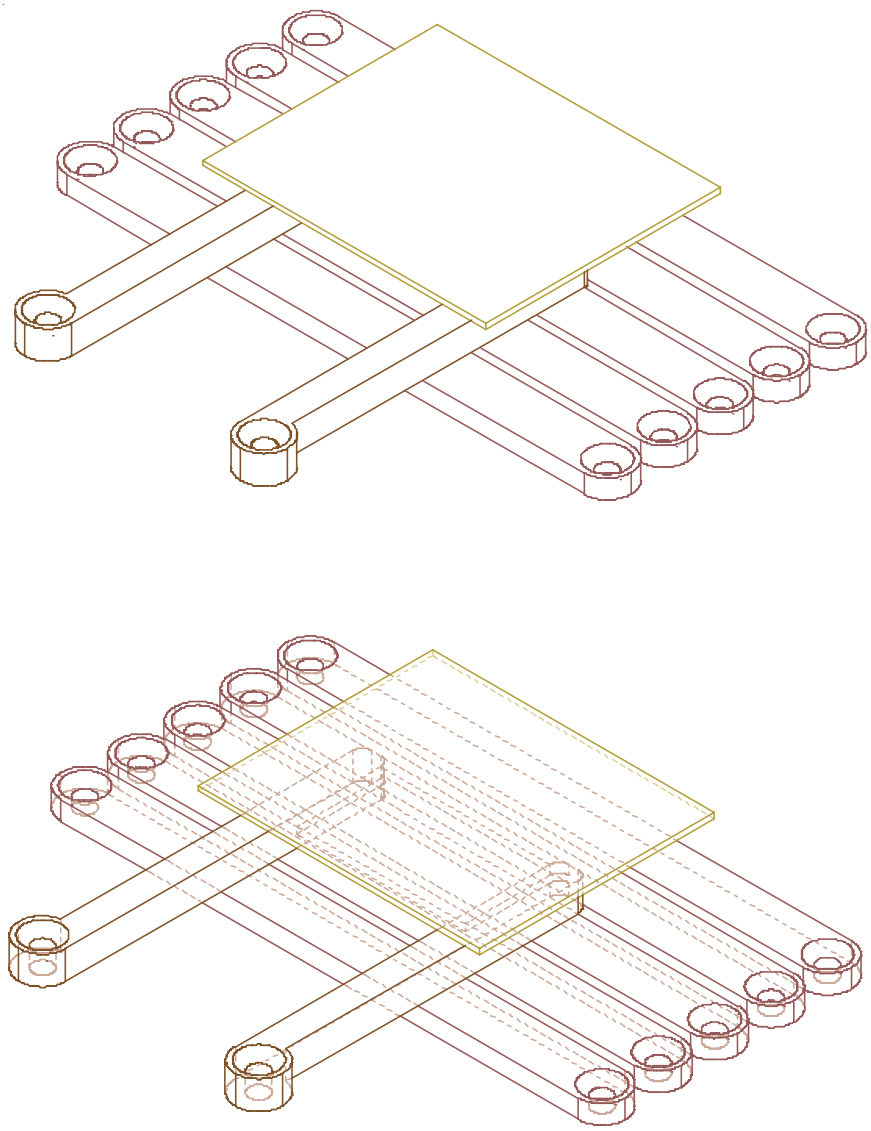

Figure 80 – Schematics of the arches, U-wire and chip for the coil-less mount design. The leads of the wires are not shown, but extend downwards from the wire termini.

Figure 81 shows the fields generated by a system with five arches for various currents. As can be seen, it is possible to get a field which is homogenous in the vicinity of a given point. Generally, as the distance from the arches increases, the field intensity grows more homogenous, but its magnitude decreases, as does the homogeneity of the field direction. Thus, a "middle" point – not too far yet not too near the arches – is preferable.

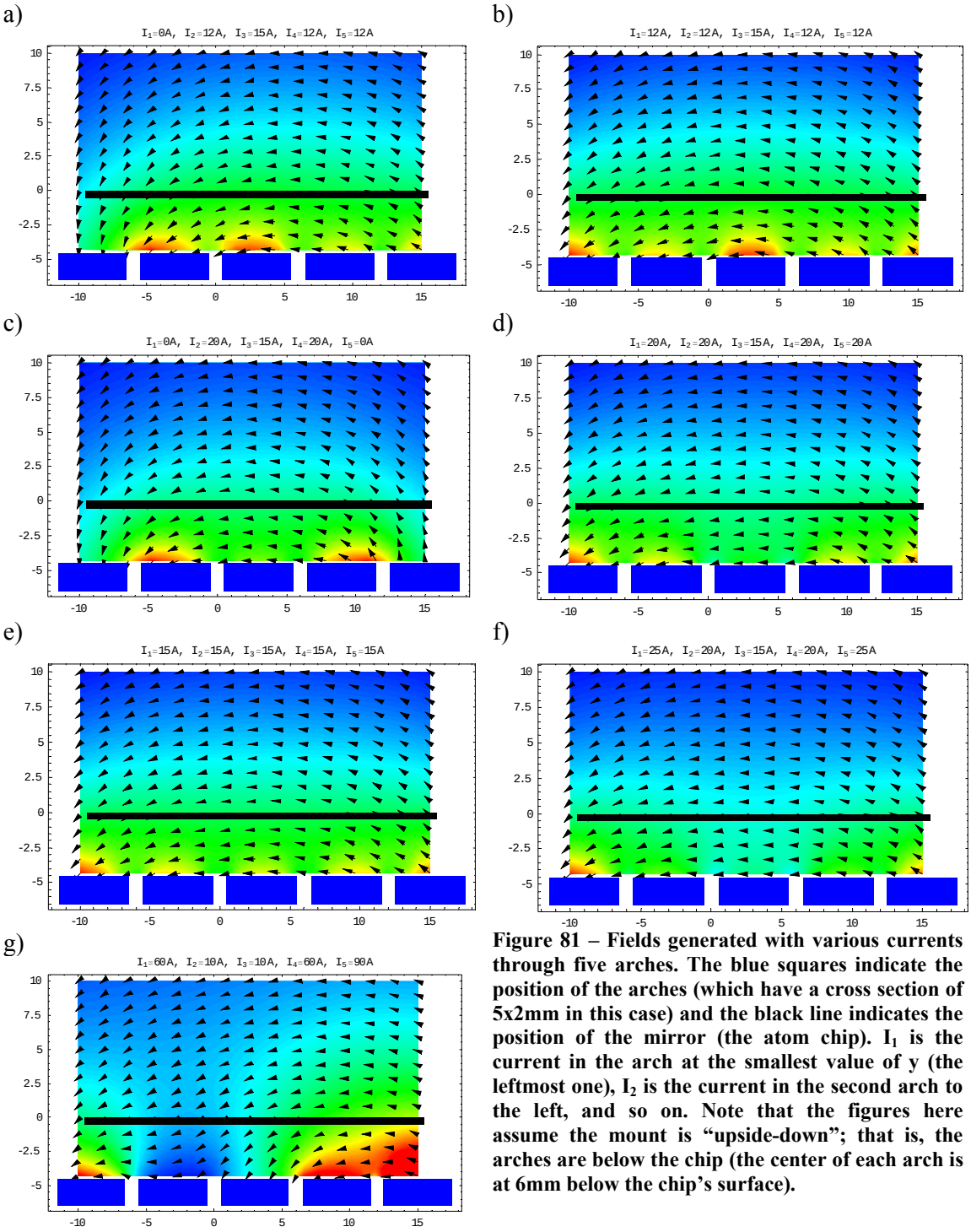

Figure 81 – Fields generated with various currents through five arches. The blue squares indicate the position of the arches (which have a cross section of 5x2mm in this case) and the black line indicates the position of the mirror (the atom chip). I_1 is the current in the arch at the smallest value of y (the leftmost one), I_2 is the current in the second arch to the left, and so on. Note that the figures here assume the mount is "upside-down"; that is, the arches are below the chip (the center of each arch is at 6mm below the chip's surface).

A.2 Implementation of a MOT – combination with a U-wire

With a locally homogeneous field generated by the arches, it is possible to create a quadrupole trap with the use of a U-wire. For the purpose of comparison, the U-wire in the calculations here is the same as for Mount 1, described previously.

For comparison, two criteria should be considered – trap depth, and good alignment with the field directions of an ideal quadrupole field. I will show here that the arch configuration is comparable to a "standard" mount in these respects.

As a standard for comparison, I will take the case for a U-wire with a current I_U=55A and a bias field (B_{0x},B_{0y},B_{0z})=(0,-12.3,3)G.

a) b)

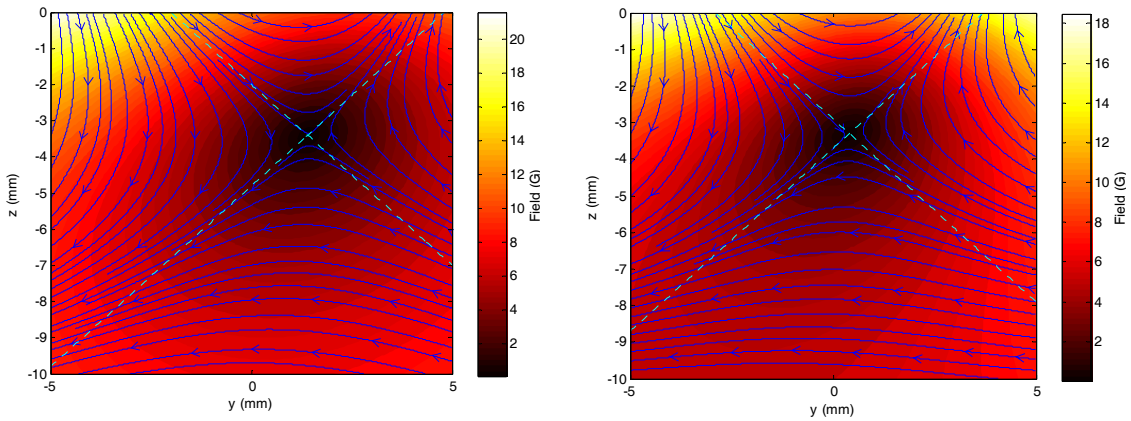

Figure 82 – Fields of the Mount 1 U-wire (a) and the same U-wire with the bias field generated by arches rather than external coils (b). The bias field in the first case is (B_{0x},B_{0y},B_{oz})=(0,-12.5,3)G, while the currents in the arches (listing the arches in order of their y coordinates) are (-50,-20,0,-60,-60). The current in the U-wire is 55A in both cases. Note that this graph shows the system as it is inside the chamber, thus the arches and the mirror are above the trapping region (the mirror surface is at z=0).

Table 8 shows the parameters for several different current configurations (using the same terminology as in Figure 41). As can be seen, the traps with arch-generated bias fields are comparable in their parameters to those with externally-generated bias fields. The field gradients are also sufficient in all cases for purely magnetic trapping, though the drawback of doing so with a zero minimum has been discussed.

As can be seen from Table 8, the position of the minimum is dependent on the currents, and thus the minimum can be moved on the y and z axes by varying the currents through one or more arches, though care must be taken to retain the necessary trapping parameters.

Bias field generated by	External coils	Arches	Arches	Arches
I_U	55A	55A	55A	55A
Bias field (B_{0x},B_{0y},B_{oz}) or current configuration (I_1, I_2, I_3, I_4, I_5)	(0,-12.5,3)G	(-50, -20, 0, -60, -60)	(-60, 0, -10, -80, -50)	(-90, 0, 0, -60, -100)
UR deviation	11.88º	13.47º	8.71º	9.82º
UL deviation	4.94º	4.19º	5.9º	6.97º
LR deviation	13.58º	12.88º	10.81º	9.2º
LL deviation	5.23º	5.05º	8.71º	11.19º
Mean deviation	8.91º	8.9º	8.53º	9.29º
Trap depth	511.66μK	376.48μK	405.75μK	515.17μK
Trap center (y_0,z_0)	(1.4,-3.4)mm	(0.4,-3.3)mm	(-0.6, -3.3)mm	(0.1, -3)mm

Table 8 – Comparison of trap types

A.3 Discussion

The advantages of the coil-less MOT have been described above. There are three main difficulties with it:

1) The arches, in the configuration described above, do not generate a homogenous bias field in the x direction. This prevents, for example, adjusting the trap depth with an x-bias field. One way to overcome this is to add another set of arches perpendicular to the existing set, creating a field in the x direction, though this is difficult to put in practice (although, depending on the configuration of the experiment, a few bars - the legs of an H-trap, if it's present, for example - may be placed).
2) It is far more difficult to calculate the currents needed to obtain a trap in a specific location than it is to calculate the bias field needed.
3) A considerable amount of current is needed for this scheme, as each arch may conceivably need to carry up to 100A. We are currently investigating the development of a device that would allow use of a single 100A current source to supply different currents to each of the arches.

Currently, the coil-less mount exists only in simulations. We are currently designing such a system for experimental use.

Appendix B Specific equations for the magnetic fields of current-carrying wires

As noted in Section 2.1, a current I generates a magnetic field in accordance with the Biot-Savart Law, which, in states

$$d\vec{B} = \frac{\mu_0}{4\pi}\frac{dI \times \vec{r}}{|\vec{r}|^3} \tag{B.1}$$

where μ_0 is the permeability of vacuum and $\vec{r}$ is the vector from the current element to the test point. Integration of $d\vec{B}$ over the current path will yield the magnetic field generated by the current flow.

However, while simple in concept, in practice such integration can be mathematically difficult. This appendix will summarize the solution of the Biot-Savart equation for several wire configurations. These equations formed the basis of the magnetic simulations and equations described in this thesis.

In the more complex cases, the derivation of the solution will also be described (or alternatively a detailed reference will be provided). The solution is usually given for a wire oriented in a specific fashion; changing orientation can generally be done through substitution of variables or using a suitable transformation matrix.

B.1 One-dimensional wires

B.1.1 Straight wire

One of the simplest solutions of the Biot-Savart Law is the case of a straight one-dimensional wire. If the wire, whose length is 2a, is lying on the x axis in such a way that it is bisected by the origin, the magnetic field is given (in Cartesian coordinates) by

$$\vec{B} = \frac{\mu_0 I}{4\pi\left(y^2+z^2\right)}\left(\frac{a-x}{\sqrt{(a-x)^2+y^2+z^2}}+\frac{a+x}{\sqrt{(a+x)^2+y^2+z^2}}\right)\left(y\hat{z}-z\hat{y}\right) \tag{B.1.1}$$

In the case of a half-infinite wire (stretching from the origin to $x\to\infty$), the field is

$$\vec{B} = \frac{\mu_0 I}{4\pi\left(y^2+z^2\right)}\left(-z\left(1+\frac{x}{\sqrt{x^2+y^2+z^2}}\right)\hat{y}+y\left(1+\frac{x}{\sqrt{x^2+y^2+z^2}}\right)\hat{z}\right) \tag{B.1.2}$$

Finally, in the case of an infinitely long wire ($a\to\infty$), the magnetic field is

$$\vec{B} = \frac{\mu_0 I}{2\pi\left(y^2+z^2\right)}\left(y\hat{z}-z\hat{y}\right) \tag{B.1.3}$$

B.1.2 Wire loop

A more complicated situation is the case where the wire is bent in the shape of a circular loop. While the calculation of the field along the centerline axis of the loop is a fairly trivial problem commonly encountered in basic physics classes, the calculation of the field elsewhere is a more complicated problem, which requires the use of elliptical integrals [56, 57]. For a circle of radius R lying in the xy plane and centered on the origin the field (in cylindrical coordinates) is

$$\begin{aligned} B_\rho &= \frac{\mu_0 I}{2\pi\rho}\sqrt{\frac{m}{4R\cdot\rho}}\left(\frac{2-m}{2-2m}E(m)-K(m)\right) \\ B_z &= \frac{\mu_0 I}{2\pi\rho}\sqrt{\frac{m}{4R\cdot\rho}}\left(\rho\cdot K(m)+\frac{R\cdot m-(2-m)\rho}{2-2m}E(m)\right) \end{aligned} \tag{B.1.4}$$

where

$$m \equiv \frac{4R\cdot\rho}{z^2+(R+\rho)^2}$$

K(m) is the complete elliptical integral of the first kind while E(m) is the complete elliptical integral of the second kind.

B.2 Three-dimensional wires

More complex is the case of current flowing through a wire which has a non-infinitesimal cross-section. The wire is assumed to lie on the x axis, with a uniform current density flowing in the positive x direction. For an infinite-length one-dimensional wire, the field is given by becomes (in the Cartesian coordinate system)

$$\vec{B}(I,y,z) = \frac{\mu_0 I}{2\pi}\frac{y}{y^2+z^2}\hat{z} - \frac{\mu_0 I}{2\pi}\frac{z}{y^2+z^2}\hat{y} \tag{B.2.1}$$

with (y,z) being the point at which the field is being evaluated, since

$$\begin{aligned} r &= \sqrt{(y-y_0)^2+(z-z_0)^2} \\ \sin\theta &= \frac{z-z_0}{r} \\ \cos\theta &= \frac{y-y_0}{r} \end{aligned} \tag{B.2.2}$$

A thick wire can be seen as a bundle of one-dimensional wires, each of which is carrying a current $JdS=Jdy_0dz_0$, with y_0 and z_0 indicating the coordinates of a specific wire in the "bundle". Therefore, equation (B.2.1) becomes (see Figure 83)

$$d\vec{B}(I,y,z)=\frac{\mu_0 J}{2\pi}\left(\frac{y-y_0}{(y-y_0)^2+(z-z_0)^2}\hat{z}-\frac{\mu_0 j}{2\pi}\frac{z-z_0}{(y-y_0)^2+(z-z_0)^2}\hat{y}\right)dS \quad \text{(B.2.3)}$$

In the case of a one-dimensional wire with a length $2L_x$, equation (2.1.15) becomes

$$\vec{B}(I,x,y,z)=B_y(I,x,y,z)\hat{y}+B_z(I,x,y,z)\hat{z}$$

$$B_y(I,x,y,z)=\frac{\mu_0 Iz}{4\pi}\left(\frac{x-L_x}{(y^2+z^2)\sqrt{(x-L_x)^2+y^2+z^2}}-\frac{x+L_x}{(y^2+z^2)\sqrt{(x+L_x)^2+y^2+z^2}}\right) \quad \text{(B.2.4)}$$

$$B_z(I,x,y,z)=\frac{\mu_0 Iy}{4\pi}\left(\frac{x+L_x}{(y^2+z^2)\sqrt{(x+L_x)^2+y^2+z^2}}-\frac{x-L_x}{(y^2+z^2)\sqrt{(x-L_x)^2+y^2+z^2}}\right)$$

and the field for a given wire in a "bundle" is expressed the same as in equation (B.2.3). In both cases, the field is obtained by

$$\vec{B}=\int_S \vec{B}'dS \quad \text{(B.2.5)}$$

B.2.1 Wires with a rectangular cross-section

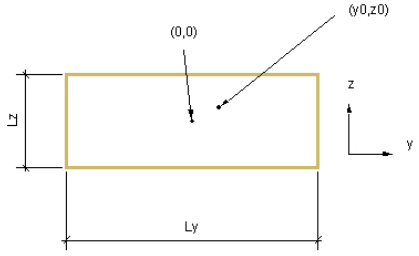

Figure 83 – Wire with a rectangular cross-section.

In this case, the wires have a rectangular cross-section with a length of L_y on the y axis and a length of L_z on the z axis. The current density is

$$J=\frac{I}{L_y L_z}$$

The integration limits are

$$-\frac{L_y}{2}<y_0<\frac{L_y}{2}$$

$$-\frac{L_z}{2}<z_0<\frac{L_z}{2}$$

Let us first examine the case where the infinitely-long wire approximation applies. The following designations will be used for convenience

$$Y_{\pm} \equiv L_y \pm 2y$$

$$Z_{\pm} \equiv L_z \pm 2z$$

Equations (B.2.3) and (B.2.5) result in

$$\begin{aligned}
B_y(y,z,L_y,L_z) &= -\frac{\mu_0 J}{2\pi}\int_{-L_z/2}^{L_z/2} dz_0 \int_{-L_y/2}^{L_y/2} \frac{z-z_0}{(y-y_0)^2+(z-z_0)^2}\,dy_0 = \\
&= -\frac{\mu_0 I}{2\pi L_y L_z}\int_{-L_z/2}^{L_z/2} dz_0 \int_{-L_y/2}^{L_y/2} \frac{z-z_0}{(y-y_0)^2+(z-z_0)^2}\,dy_0 = \\
&= \frac{\mu_0 I}{2\pi L_y L_z}\int_{-L_z/2}^{L_z/2}\left(\tan^{-1}\frac{Y_+}{2z_0-2z}+\tan^{-1}\frac{Y_-}{2z_0-2z}\right)dz_0 = \\
&= \frac{\mu_0 I}{8\pi L_y L_z}\left(\begin{array}{l} 2Z_-\left(\tan^{-1}\dfrac{Y_-}{Z_-}+\tan^{-1}\dfrac{Y_+}{Z_-}\right)-2Z_+\left(\tan^{-1}\dfrac{Y_-}{Z_+}+\tan^{-1}\dfrac{Y_+}{Z_+}\right) \\ +Y_-\ln\dfrac{Y_-^2+Z_-^2}{Y_-^2+Z_+^2}+Y_+\ln\dfrac{Y_+^2+Z_-^2}{Y_+^2+Z_+^2}\end{array}\right)
\end{aligned} \tag{B.2.6}$$

$$\begin{aligned}
B_z(y,z,L_y,L_z) &= \frac{\mu_0 J}{2\pi}\int_{-L_y/2}^{L_y/2} dy_0 \int_{-L_z/2}^{L_z/2} \frac{y-y_0}{(y-y_0)^2+(z-z_0)^2}\,dz_0 = \\
&= \frac{\mu_0 I}{2\pi L_y L_z}\int_{-L_y/2}^{L_y/2} dy_0 \int_{-L_z/2}^{L_z/2} \frac{y-y_0}{(y-y_0)^2+(z-z_0)^2}\,dz_0 = \\
&= -\frac{\mu_0 I}{2\pi L_y L_z}\int_{-L_y/2}^{L_y/2}\left(\tan^{-1}\frac{Z_-}{2z_0-2z}+\tan^{-1}\frac{Z_+}{2z_0-2z}\right)dy_0 = \\
&= \frac{\mu_0 I}{8\pi L_y L_z}\left(\begin{array}{l} 2Y_+\left(\tan^{-1}\dfrac{Z_-}{Y_+}+\tan^{-1}\dfrac{Z_+}{Y_+}\right)-2Y_-\left(\tan^{-1}\dfrac{Z_-}{Y_-}+\tan^{-1}\dfrac{Z_+}{Y_-}\right) \\ -Z_-\ln\dfrac{Y_-^2+Z_-^2}{Y_+^2+Z_-^2}-Z_+\ln\dfrac{Y_-^2+Z_+^2}{Y_+^2+Z_+^2}\end{array}\right)
\end{aligned} \tag{B.2.7}$$

In the case of a wire of finite length $2L_x$, the computation is significantly more complex and results in

$$B_y\left(x,y,z,L_x,L_y,L_z,I\right)=$$

$$=\frac{\mu_0 J}{4\pi}\int_{-L_y/2}^{L_y/2}dy_0\int_{-L_z/2}^{L_z/2}\frac{z-z_0}{(y-y_0)^2+(z-z_0)^2}\left(\frac{x-L_x}{\sqrt{(x-L_x)^2+(y-y_0)^2+(z-z_0)^2}}-\frac{x+L_x}{\left(y^2+z^2\right)\sqrt{(x+L_x)^2+(y-y_0)^2+(z-z_0)^2}}\right)dz_0=$$

$$=\frac{\mu_0 I}{4\pi L_y L_z}\int_{-L_y/2}^{L_y/2}\sum_{i,j=0}^{1}(-1)^j\coth^{-1}\left(\frac{2\left(L_x+(-1)^i x\right)}{\sqrt{4\left(L_x+(-1)^i x\right)^2+4\left(y-y_0\right)^2+\left(L_z+(-1)^j z\right)^2}}\right)=$$

$$=\frac{\mu_0 I}{16\pi L_y L_z}\left(\begin{array}{l}2\sum_{i,j,k=0}^{1}(-1)^{k+1}\left(L_z+2(-1)^k z\right)\tan^{-1}\left(\frac{2\left(L_x+(-1)^i x\right)\left(L_y+2(-1)^j y\right)}{\left(L_z+2(-1)^k z\right)\sqrt{4\left(L_x+(-1)^i x\right)^2+\left(L_y+2(-1)^j y\right)^2+\left(L_z+2(-1)^k z\right)^2}}\right)+\\ +\sum_{i,j,k,m=0}^{1}(-1)^{i+k+m}\left(L_y+2(-1)^j y\right)\ln\left(\frac{2+(-1)^{i+m}\sqrt{4\left(L_x+(-1)^i x\right)^2+\left(L_y+2(-1)^j y\right)^2+\left(L_z+2(-1)^k z\right)^2}}{L_x+(-1)^i x}\right)+\\ +4\sum_{i,j,k=0}^{1}(-1)^{j+k}\left(L_x+(-1)^i x\right)\ln\left((-1)^j\left(L_y+2(-1)^j y\right)+\sqrt{4\left(L_x+(-1)^i x\right)^2+\left(L_y+2(-1)^j y\right)^2+\left(L_z+2(-1)^k z\right)^2}\right)\end{array}\right)\quad\text{(B.2.8)}$$

$$B_z\left(x,y,z,L_x,L_y,L_z,I\right)=$$

$$=\frac{\mu_0 J}{4\pi}\int_{-L_z/2}^{L_z/2}dz_0\int_{-L_y/2}^{L_y/2}\frac{y-y_0}{(y-y_0)^2+(z-z_0)^2}\left(\frac{x+L_x}{\sqrt{(x+L_x)^2+(y-y_0)^2+(z-z_0)^2}}-\frac{x-L_x}{\sqrt{(x-L_x)^2+(y-y_0)^2+(z-z_0)^2}}\right)dy_0=$$

$$=\frac{\mu_0 I}{4\pi L_y L_z}\int_{-Lz/2}^{L_z/2}\sum_{i,j=0}^{1}(-1)^{j+1}\coth^{-1}\left(\frac{2\left(L_x+(-1)^i x\right)}{\sqrt{4\left(L_x+(-1)^i x\right)^2+\left(L_y+2(-1)^j y\right)^2+4\left(z-z_0\right)^2}}\right)dz_0=$$

$$=\frac{\mu_0 I}{16\pi L_y L_z}\left(\begin{array}{l}2\sum_{i,j,k=0}^{1}(-1)^{j}\left(L_y+2(-1)^j y\right)\tan^{-1}\left(\frac{2\left(L_x+(-1)^i x\right)\left(L_z+2(-1)^k z\right)}{\left(L_y+2(-1)^j y\right)\sqrt{4\left(L_x+(-1)^i x\right)^2+\left(L_y+2(-1)^j y\right)^2+\left(L_z+2(-1)^k z\right)^2}}\right)+\\ +\sum_{i,j,k,m=0}^{1}(-1)^{j+m+1}\left(L_z+2(-1)^k z\right)\ln\left(\frac{2+(-1)^m\sqrt{4\left(L_x+(-1)^i x\right)^2+\left(L_y+2(-1)^j y\right)^2+\left(L_z+2(-1)^k z\right)^2}}{L_x+(-1)^i x}\right)+\\ +4\sum_{i,j,k=0}^{1}(-1)^{j+k+1}\left(L_x+(-1)^i x\right)\ln\left((-1)^k\left(L_z+2(-1)^k z\right)+\sqrt{4\left(L_x+(-1)^i x\right)^2+\left(L_y+2(-1)^j y\right)^2+\left(L_z+2(-1)^k z\right)^2}\right)\end{array}\right)\quad\text{(B.2.9)}$$

B.2.2 Wires with a circular cross section

For a wire with a circular cross section of radius R, rather than using the technique described in the previous section, it is much simpler to calculate the current using Ampere's Law[47]

$$\oint \vec{B} d\vec{l} = \mu_0 I \tag{B.2.10}$$

Expressed in terms of equation (B.2.1), the resulting field is

$$\vec{B}(I, y_0, z_0, r) = \begin{cases} \vec{B}\left(I \cdot \frac{r}{R^2}, y_0, z_0\right) & r < R \\ \vec{B}(I, y_0, z_0) & r > R \end{cases} \tag{B.2.11}$$

[47] Again, this is a common problem set in undergraduate physics courses, and can be found in the appropriate textbooks

Appendix C Properties of Rubidium

The atom cloud used in the experiments described in this work is composed of ^{87}Rb atoms. Table 9 and Figure 84 show some of its properties and the energy levels relevant to the experiment, respectively.

Property			Symbol	Value
Name			^{87}Rb	Rubidium 87
Atomic Mass			m	86,909 u (1.443×10^{-25} Kg)
Atomic Number				37
Nuclear Spin				3/2
Magnetic Moment				2.75 μ_p
Doppler temperature			T_D	141 μK
Spectroscopy	D-1 Line	Transition wavelength	λ_0 (=c/ν)	794.978 nm
		Natural Lifetime	τ	27.7 ns
		Natural Linewidth	γ/2π (=1/2πτ)	5.74 MHz
		Saturation Intensity	I_s	1.49 mW/cm^2
	D-2 Line	Transition wavelength	λ_0 (=c/ν)	780.241 nm
		Natural Lifetime	τ	26.24 ns
		Natural Linewidth	γ/2π (=1/2πτ)	6.065 MHz
		Saturation Intensity	I_s	1.69 mW/cm^2

Table 9 – Some properties of ^{87}Rb [58]

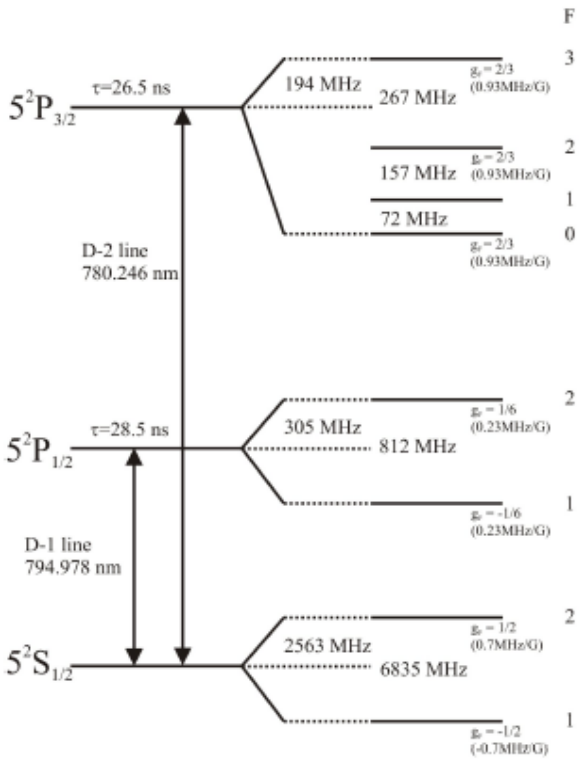

Figure 84 – Hyperfine energy levels[48] of ^{87}Rb. [14]

[48] It should be noted that while the sublevels here are all denoted as "F", the sublevels of the excited states are denoted with F' in the text.

In the MOT experiment, the F=2→F'=3 in the $5^2S_{1/2}\rightarrow 5^2P_{3/2}$ transition is used for cooling and trapping. As noted in section 2.3, on occasion (approximately once every 1,000 cycles) the atom decays to the "wrong" ground state – the F=1 state, in this case - and thus cannot be subsequently reexcited by the cooling laser. To deal with that contingency a second laser (known as the "repumper") is used to excite atoms from the F=1 ground state to the F'=2 hyperfine level of the $5^2P_{1/2}$ level, allowing them to decay back to the F=2 sublevel.

The natural distribution of rubidium isotopes is 72.17% being ^{85}Rb and 27.83% being ^{87}Rb. However, the difference in the two isotopes' spectral lines is sufficient to allow working with only one isotope.

Appendix D Mount 1 Schematics

This section contains the detailed schematics for the H- and U-wires of the mount described in section 3.2. All specifications are in millimeters. Screw holes use standard metric notations (M4, M6, etc.).

D.1 H-wire crosspiece

Part Name: H-Wire (crosspiece)
Units: mm
Material: copper
Qty: 1
Notes: Polish contacts (bottom of circular portion)

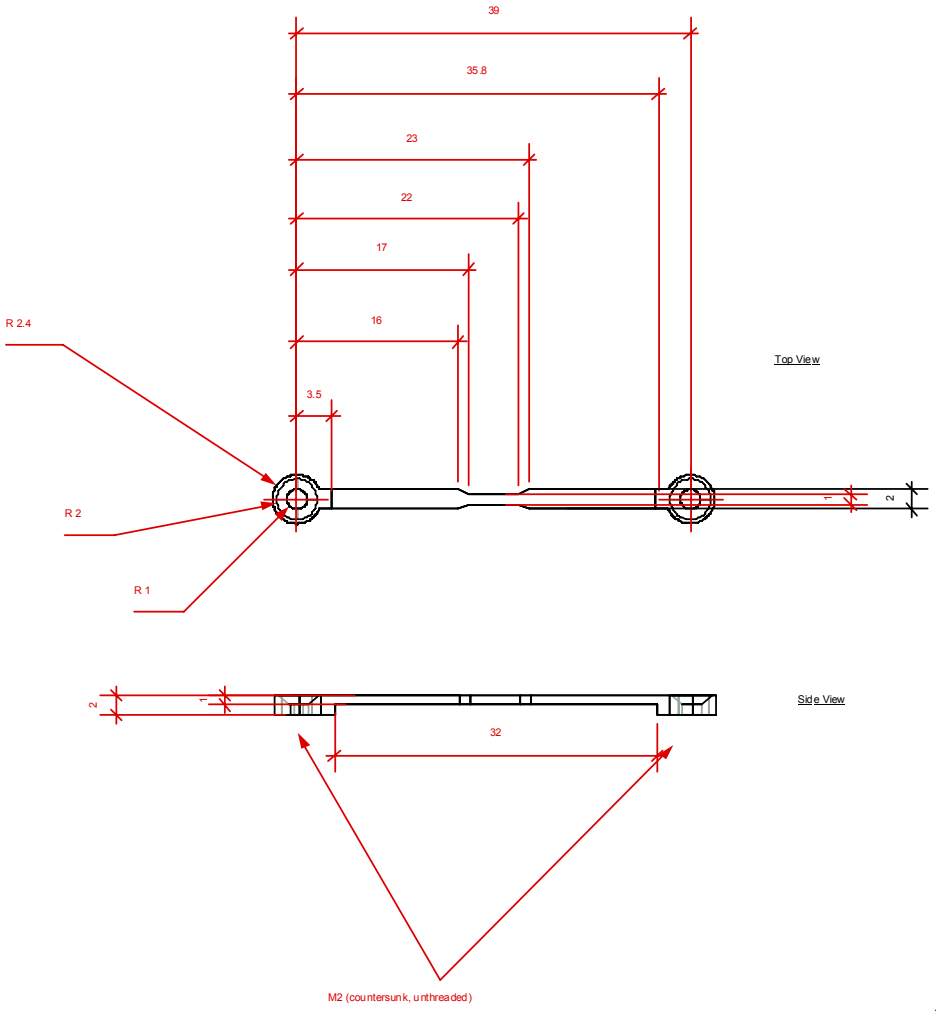

D.2 H-wire "legs"

Only one of the two legs is shown here; the other is a mirror image of it (mirrored along the long axis).

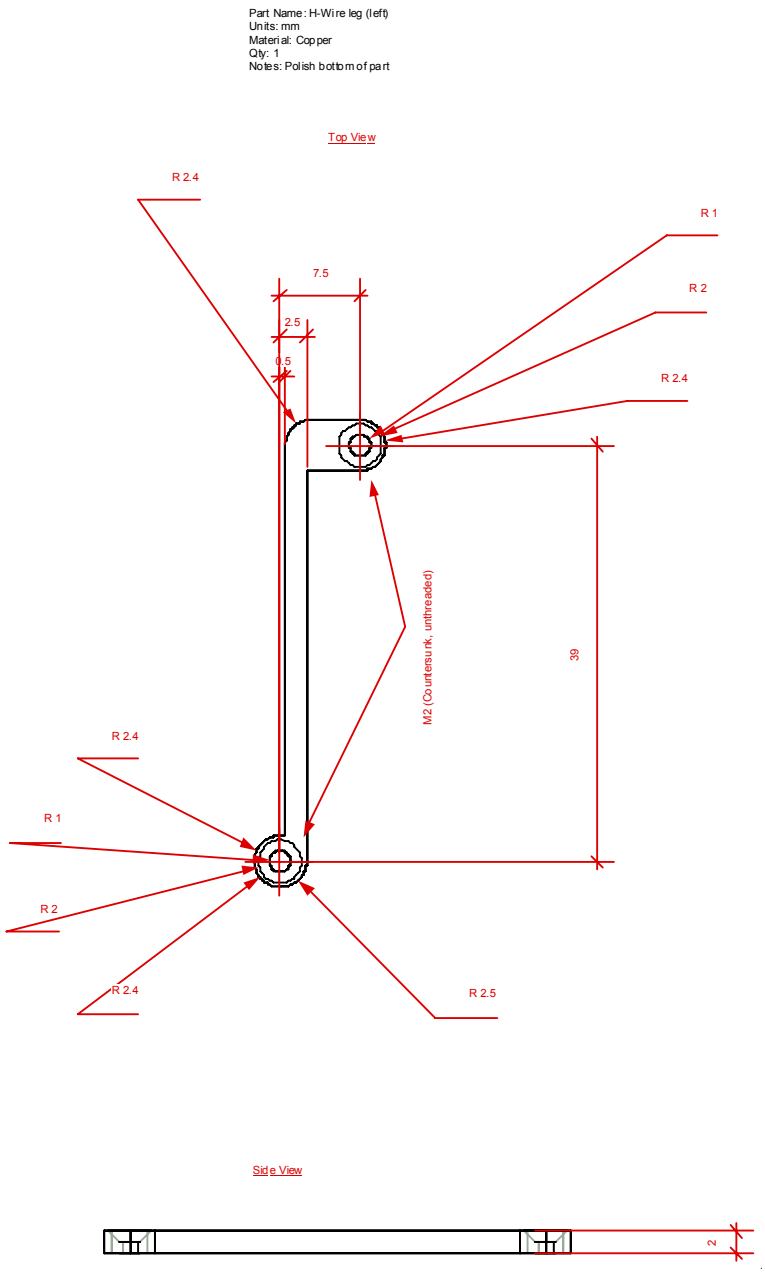

D.3 U-wire

Part Name: U-Wire
Units: mm
Material: Copper
Qty: 1
Notes: Polish bottom

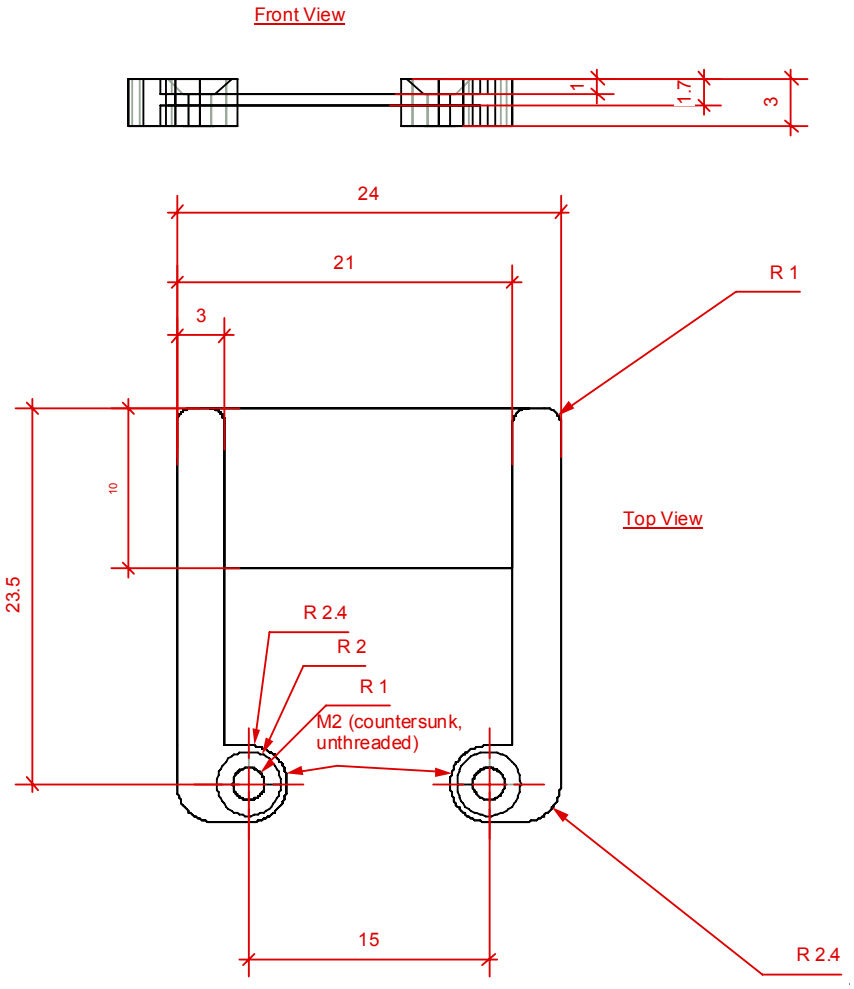

D.4 Ceramic Block

It should be noted that since the chip is glued on top of the block, air may be trapped in the M3 screws' channels or head. To prevent this, we filed a shallow groove from the top of each screw hole to the channel of the H-wire legs or the U-wire, as appropriate. These grooves are not shown in these schematics, but can be seen in Figure 52.

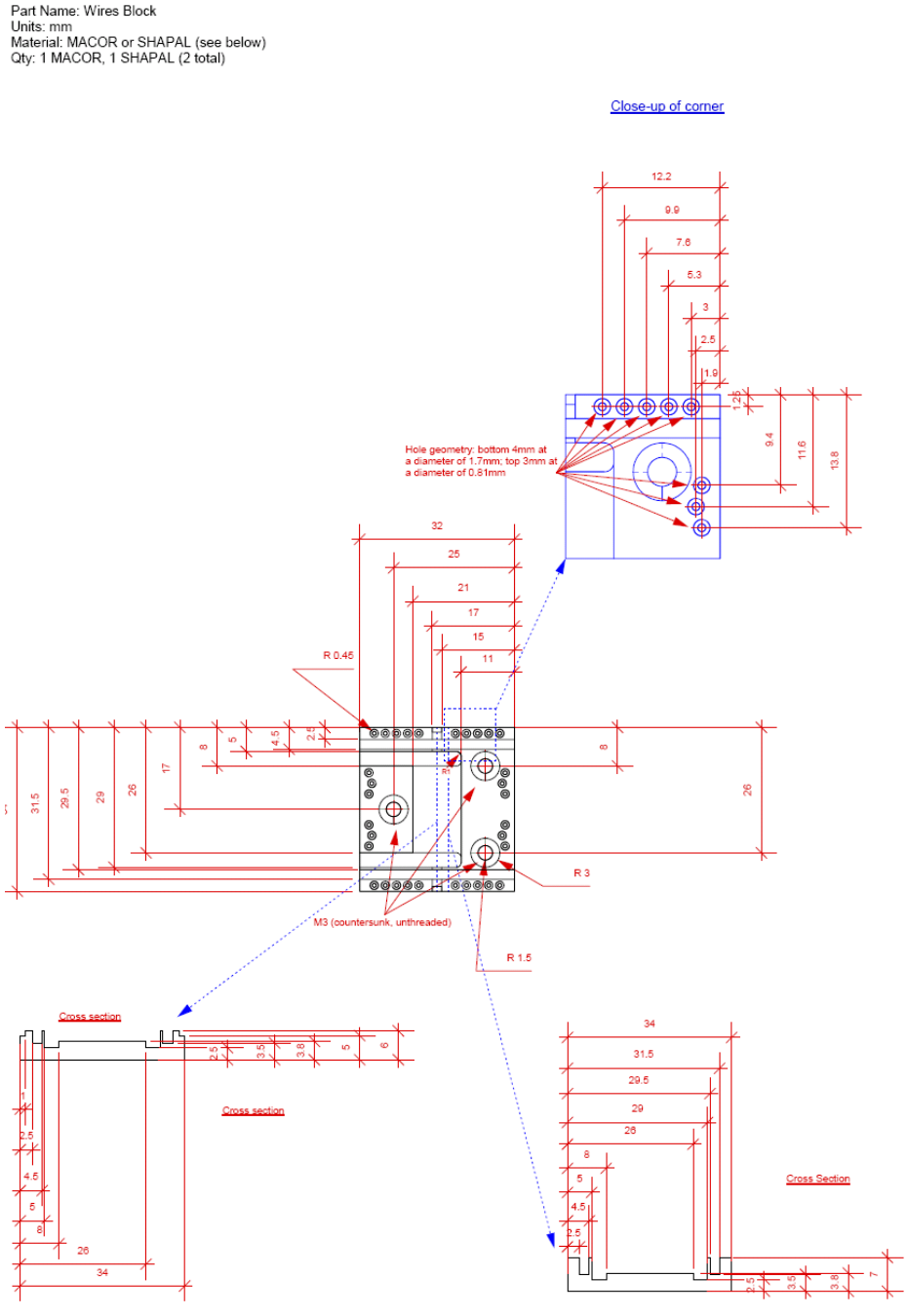

Appendix E Wires on the Atom Chip

a)

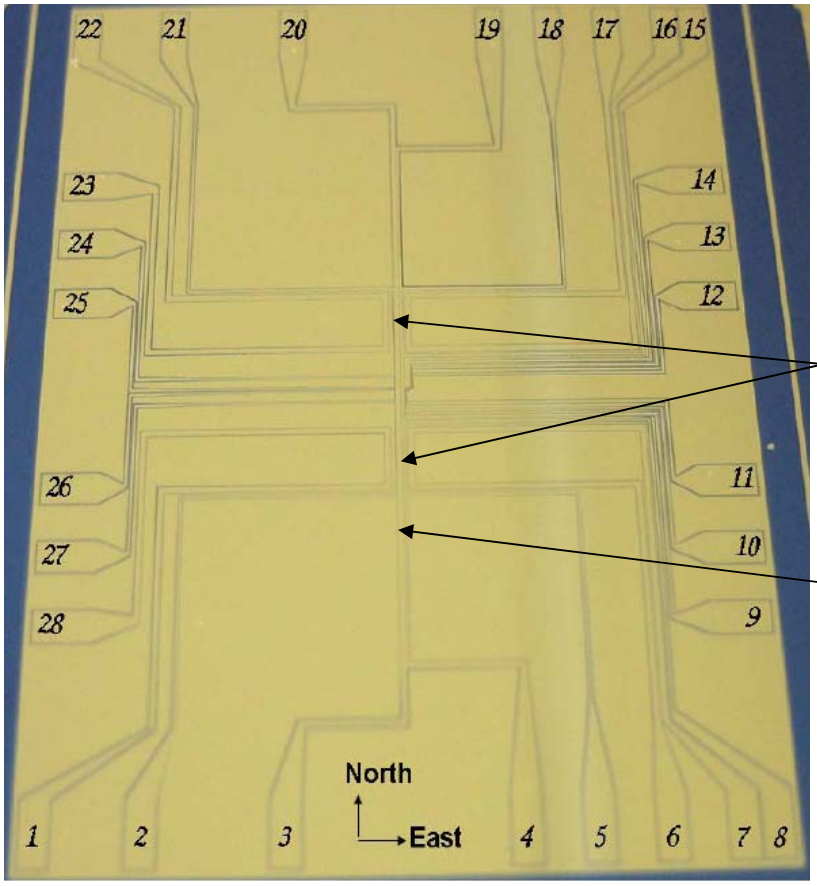

b)

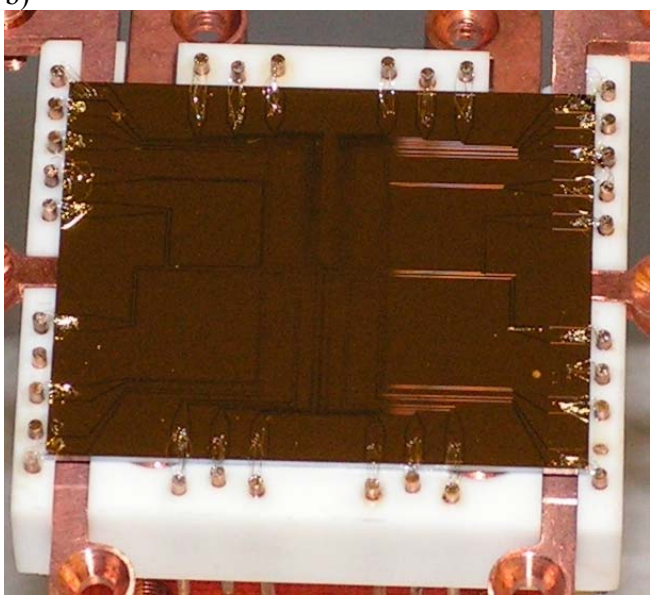

Figure 85 – Photos of the chip wires (a) and the chip after bonding (b)

Appendix F Software

This section will describe some of the programs used to create the more important simulations, equations, and plots in this work (only a representative sample of the programs is included here; some of the longer, more complicated ones were not included). The primary applications used for these calculations were MatLab 7.2, Mathematica 5.2, and Comsol Multiphysics 3.2b.

In the case of Mathematica programs, it should be noted that some of the cells described below were consolidated for clarity; in practice, if running one of them repeatedly, it is often more convenient to split it into multiple cells to avoid having to rerun a section which calculates the basic equations each time.

F.1 The Z-trap

These programs calculate various parameters for the Z-trap. With minor modifications, they can be used for the U- and H-traps as well.

F.1.1 Calculating the Z-wire trap's equation (1-D wire)

This Mathematica notebook clears all the definitions from memory and calculates the equation for the Z-trap field (without bias) as described in Chapter 2.1.3.

```
Clear["Global`*"]

P = {x, y, z};
s1 = {-a, t, 0};
s2 = {t, 0, 0};
s3 = {a, t, 0};

r1 = P - s1;
r2 = P - s2;
r3 = P - s3;

B1 = (μ × curr)/(4 π) Integrate[∂t s1 × r1/(r1.r1)^(3/2), {t, -∞, 0}, GenerateConditions → False];
B2 = (μ × curr)/(4 π) Integrate[∂t s2 × r2/(r2.r2)^(3/2), {t, -a, a}, GenerateConditions → False];
B3 = (μ × curr)/(4 π) Integrate[∂t s3 × r3/(r3.r3)^(3/2), {t, 0, ∞}, GenerateConditions → False];

B = B1 + B2 + B3
```

F.1.2 Y-axis bias field

This Mathematica cell calculates the y-axis bias field required for a minimum at $(0,0,z_0)$. The cell described in F.1.1 must be run before this.

```
Ba = B + {0, By, 0};
BMag = √(Ba.Ba);
Dv = ∂z BMag /. x → 0 /. y → 0;
T = Solve[Dv == 0, {By}][[1, 1, 2]] /. z → z0;
```

F.1.3 Rotation of the Z-trap's field

This cell will calculate the rotation of the field caused by the Z-trap from alignment with the crosspiece, and will output several graphs. I0 indicates the desired current, z1 the height of the minimum, and a0 half the length of the crosspiece. These values are used in generating the graphs. The variable Th will contain the result. The function described in F.1.2 must be run prior to this cell.

```
(*Twist of field*)
I0 = 5;
a0 = 4;
z1 = 3;
xmin = -5;
xmax = 5;
ymin = -5;
ymax = 5;

Bb = Ba /. By → T;
BMag0 = √(Bb.Bb) /. z → z0;
H = FullSimplify[{{∂x,x BMag0, ∂y,x BMag0}, {∂x,y BMag0, ∂y,y BMag0}} /. x → 0 /. y → 0, Assumptions → {μ > 0, a > 0}] // MatrixForm
T2 = Eigensystem[H[[1]] /. μ → 4π /. curr → I0 /. x → 0 /. y → 0];
(*Calculate slopes of lines*)
Ca = -T2[[2]][[1]][[1]] / T2[[2]][[1]][[2]];
Cb = -T2[[2]][[2]][[1]] / T2[[2]][[2]][[2]];
(*Calculate second directional deriatives along the lines to determine which is which*)
Da = 1/(1+Ca²) ∂x,x BMag0 + 2Ca/(1+Ca²) ∂x,y BMag0 + Ca²/(1+Ca²) ∂y,y BMag0;
Db = 1/(1+Cb²) ∂x,x BMag0 + 2Cb/(1+Cb²) ∂x,y BMag0 + Cb²/(1+Cb²) ∂y,y BMag0;
If[(Da /. x → 0 /. y → 0 /. z0 → z1 /. a → a0 /. μ → 4π /. curr → I0) < (Db /. x → 0 /. y → 0 /. z0 → z1 /. a → a0 /. μ → 4π /. curr → I0), Cm = Ca, Cm = Cb];
Th = ArcTan[Cb];

Plot3D[180/π Th /. μ → 4π /. curr → I0 /. z → z0 /. x → 0 /. y → 0, {a, 0.0001, 10}, {z0, 0.000001, 5}, Axes → True, ColorFunction → Hue,
 AxesLabel → {"a (mm)", "z0 (mm)", "θT^Z (°)"}, PlotLabel -> "(a)", Mesh → False, PlotPoints → 100]
DisplayTogetherArray[Plot[180/π Th /. μ → 4π /. curr → I0 /. z → z0 /. z0 → z1 /. x → 0 /. y → 0, {a, 0, 10}, PlotRange → All, AxesLabel → {"a (mm)", "θT^Z (°)"},
   PlotLabel → StringJoin[{"(b)\nz0=", ToString[z1], "mm"}]],
  Plot[180/π Th /. μ → 4π /. curr → I0 /. z → z0 /. a → a0 /. x → 0 /. y → 0, {z0, 0, 5}, PlotRange → All, AxesLabel → {"z0 (mm)", "θT^Z (°)"},
   PlotLabel → StringJoin[{"(c)\na=", ToString[a0], "mm"}]]];
```

F.1.4 Calculating the Z-trap frequencies

This function calculates the transverse and longitudinal frequencies for a Z-trap, and creates plots over varying values of a, z_0, and I. The cell in F.1.2 must be run prior to running this cell.

```
(*Frequency of trap*)
I0 = 5;
a0 = 4;
z1 = 1.5;
xmin = -5;
xmax = 5;
ymin = -5;
ymax = 5;
z0min = 0.5;
z0max = 5;
amin = 0;
amax = 10;
Imin = 1;
Imax = 100;

muB = 9.268×10^-22;
m = 1.4228×10^-25;

Bb = Ba /. By→ T;
BMagz0 = √ Bb.Bb /. z→ z0;
H = FullSimplify[{{∂x,x BMagz0, ∂y,x BMagz0}, {∂x,y BMagz0, ∂y,y BMagz0}} /. x→ 0 /. y→ 0, Assumptions→ {μ > 0, a > 0}] // MatrixForm;
T2 = Eigensystem[H[[1]] /. μ→ 4 π /. curr→ I0 /. x→ 0 /. y→ 0];
(*Calculate slopes of lines*)
Ca = -T2[[2]][[1]][[1]] / T2[[2]][[1]][[2]];
Cb = -T2[[2]][[2]][[1]] / T2[[2]][[2]][[2]];
(*Calculate second directional deriatives along the lines*)
Da = 1/(1+Ca^2) ∂x,x BMagz0 + 2 Ca/(1+Ca^2) ∂x,y BMagz0 + Ca^2/(1+Ca^2) ∂y,y BMagz0;
Db = 1/(1+Cb^2) ∂x,x BMagz0 + 2 Cb/(1+Cb^2) ∂x,y BMagz0 + Cb^2/(1+Cb^2) ∂y,y BMagz0;
If[(Da /. x→ 0 /. y→ 0 /. z0→ z1 /. a→ a0 /. μ→ 4 π /. curr→ I0) < (Db /. x→ 0 /. y→ 0 /. z0→ z1 /. a→ a0 /. μ→ 4 π /. curr→ I0), Dmin = Da; Dmax = Db, Dmin = Db; Dmax = Da];
FLong = √(muB/m) Dmin;
FTrans = √(muB/m) Dmax;
Fz = √(muB/m) ∂z,z BMag /. By→ T;
DisplayTogetherArray[DisplayTogether[Plot[FLong /. μ→ 4 π /. curr→ I0 /. z→ z0 /. z0→ z1 /. x→ 0 /. y→ 0, {a, amin, amax}, PlotRange→ All],
  Plot[FTrans /. μ→ 4 π /. curr→ I0 /. z→ z0 /. z0→ z1 /. x→ 0 /. y→ 0, {a, amin, amax}, PlotRange→ All, PlotStyle→ RGBColor[0, 0, 1]],
  Plot[Fz /. μ→ 4 π /. curr→ I0 /. z→ z0 /. z0→ z1 /. x→ 0 /. y→ 0, {a, amin, amax}, PlotRange→ All, PlotStyle→ RGBColor[0, 1, 0]],
  AxesLabel→ {"a (mm)", "ω (2π×Hz)"}, PlotLabel→ StringJoin[{"(a)\nz0=", ToString[z1], "mm, I=", ToString[I0], "A"}]],
 DisplayTogether[Plot[FLong /. μ→ 4 π /. curr→ I0 /. z→ z0 /. a→ a0 /. x→ 0 /. y→ 0, {z0, z0min, z0max}, PlotRange→ All],
  Plot[FTrans /. μ→ 4 π /. curr→ I0 /. z→ z0 /. a→ a0 /. x→ 0 /. y→ 0, {z0, z0min, z0max}, PlotRange→ All, PlotStyle→ RGBColor[0, 0, 1]],
  Plot[Fz /. μ→ 4 π /. curr→ I0 /. z→ z0 /. a→ a0 /. x→ 0 /. y→ 0, {z0, z0min, z0max}, PlotRange→ All, PlotStyle→ RGBColor[0, 1, 0]],
  AxesLabel→ {"z0 (mm)", "ω (2π×Hz)"}, PlotLabel→ StringJoin[{"(b)\na=", ToString[a0], "mm, I=", ToString[I0], "A"}]],
 DisplayTogether[Plot[FLong /. μ→ 4 π /. z→ z0 /. a→ a0 /. x→ 0 /. y→ 0 /. z0→ z1, {curr, Imin, Imax}, PlotRange→ All],
  Plot[FTrans /. μ→ 4 π /. z→ z0 /. a→ a0 /. x→ 0 /. y→ 0 /. z0→ z1, {curr, Imin, Imax}, PlotRange→ All, PlotStyle→ RGBColor[0, 0, 1]],
  Plot[Fz /. μ→ 4 π /. a→ a0 /. z→ z0 /. z0→ z1 /. x→ 0 /. y→ 0, {curr, Imin, Imax}, PlotRange→ All, PlotStyle→ RGBColor[0, 1, 0]],
  AxesLabel→ {"I (A)", "ω (2π×Hz)"}, PlotLabel→ StringJoin[{"(c)\nz0=", ToString[z1], "mm, a=", ToString[a0], "mm"}]]]
```

F.1.5 Depth of the Z-trap

This will calculate the depth of a trap (in Gauss) at height z_0.

```
(*Depth of trap*)
BMag2 = BMag /. By → T;
BMInf = Limit[BMag2, z → ∞];
BMInf - FullSimplify[BMag2 /. z → z0 /. x → 0 /. y → 0, Assumptions → {a > 0, μ > 0}]
```

F.2 Magnetic field simulations

The following two MatLab functions are used in conjunction with Magsim as described in Chapter 4.

```
function [Bi,absBi]=biasAdd(B,bias)
%adds a [Bx,By,Bz]  bias field to field B (which is a 3xmxnxk
array), and
%returns the modified field Bi and the field's absolute size absBi
bias=repmat(bias',[1,size(B,2),size(B,3),size(B,4)]);
Bi=B+bias;
absBi=squeeze(sqrt(Bi(1,:,:,:).^2+Bi(2,:,:,:).^2+Bi(3,:,:,:).^2));
```

```
function [B,absB]=sumelements(mag,J,bias);
% magnetic field of a sum of magnetic fields.
mag is a cell array of
% structures for each element. J is a vector of
currents for each
% element.
if nargin<3,
    bias=[0 0 0];
end;
B=mag{1}.B*J(1);
for j=2:length(mag),
    if J(j) ~= 0,
        B=B+mag{j}.B*J(j);
    end;
end;
if nargin<3,
    absB=sqrt(squeeze(sum(B.^2)));
else
    [B,absB]=biasAdd(B,bias);
end;
```

The results are arrays giving the fields generated for a given current configuration, which can then be used for a variety of calculations.

F.3 Calculating angle deviations

Another MatLab function was used to calculate the deviations of a field from the directions of an ideal quadrupole, as discussed in section 2.3.2. This function accepts a current for the U-wire (IU) and for a side guide (ISG) and the coordinates (y0, z0) where the minimum is desired. The width of the U-wire (2xl) is supplied in the body of the function. The function then calculates the requisite bias fields for the side guide and U-wire, calculates the deviation in each quadrant, and finds the mean value by means of integration, returning the deviations for both wire configurations.

```
function varargout=WireFieldAngles(ISG,IU,y0,z0)
%Calculate the deviation in field angles of wires from an ideal quadrupole
    r=5;
    res=0.01;
     mu=4*pi;
     IQuad=1;
     b=40;
    a1=1;
    a2=-1;
    l=5;
    x=0;

    SGB=BSG(y0,z0,ISG,[0,0,0],mu);%Calculate side guide field at (y0,z0),
no bias
    UB=UField(0,y0,z0,l,IU,[0,0,0],mu);
    SGBias=[0,-SGB(2),-SGB(3)];%Calculate bias field for minimum at (y0,z0)
    UBias=[0,-UB(2),-UB(3)];
    a=a1;
    yr=r*cos(atan(a));
    yres=res*cos(atan(a));
    yur=y0:yres:(y0+yr);
    DSGur=OTHSG(yur);
    DUur=OTHU(yur);
    yll=y0:-yres:(y0-yr);
    DSGll=OTHSG(yll);
    DUll=OTHU(yll);
    a=a2;
    yr=r*cos(atan(a));
    yres=res*cos(atan(a));
    yul=y0:-yres:(y0-yr);
    DSGul=OTHSG(yul);
    DUul=OTHU(yul);
```

(continued…)

```
    ylr=y0:yres:(y0+yr);
    DSGlr=OTHSG(ylr);
    DUlr=OTHU(ylr);
    varargout{1}=DSGur;
    varargout{2}=DSGul;
    varargout{3}=DSGll;
    varargout{4}=DSGlr;
    varargout{5}=DUur;
    varargout{6}=DUul;
    varargout{7}=DUll;
    varargout{8}=DUlr;
    varargout{9}=0:res:r;
    function dev=OTHSG(y)
    %calculate the deviation at a given point
        z=a.*(y-y0)+z0;
        SGB=BSG(y,z,ISG,SGBias,mu);%Calculate side guide field in
space
        QB=BQuad(y,z,IQuad,mu,y0,z0,b);%Calculate quadrupole field
        thSG=TH(atan2(SGB(:,3),SGB(:,2)));
        thQ=TH(atan2(QB(:,3),QB(:,2)));
        dev=180.*Deviation(thSG,thQ)./pi;
    end
    function dev=OTHU(y)
        %calculate the deviation at a given point
        z=a.*(y-y0)+z0;
        U=UField(repmat(x,1,length(y)),y,z,l,IU,UBias,mu); %Calculate
U-wire field in space
        QB=BQuad(y,z,IQuad,mu,y0,z0,b);%Calculate quadrupole field
        thU=TH(atan2(U(:,3),U(:,2)));
        thQ=TH(atan2(QB(:,3),QB(:,2)));
        dev=180.*Deviation(thU,thQ)./pi;
    end
end

function B=BSG(y,z,I,Bias,mu)
%Return field of a side guide at point (y,z) with current I and bias
field Bias,
%located at (0,0,0)
    Bx=repmat(Bias(1),1,length(y));
    By=repmat(Bias(2),1,length(y));
    Bz=repmat(Bias(3),1,length(y));
    B=zeros(length(y),3);
    B(:,1)=Bx';
    B(:,2)=(By-(I.*z.*mu)./(2*pi*(y.^2+z.^2)))';
    B(:,3)=(Bz+(I.*y.*mu)./(2*pi.*(y.^2+z.^2)))';
end
function B=BQuad(y,z,I,mu,y0,z0,b)
%Return field  at (y,z) of a 4-wire quadrupole with current I, whose
center
%is at (y0,z0) and the wires are seperated from the center by b
    B=zeros(length(y),3);
    B(:,2)=(I*mu)/(2*pi)*((b-z+z0)./((y-y0).^2+(b-z+z0).^2)-(b+z-
z0)./((y-y0).^2+(b+z-z0).^2)-(z0-z)./((b+y-y0).^2+(z-z0).^2)-(z0-
z)./((b-y+y0).^2+(z-z0).^2))';
    B(:,3)=(I*mu)/(2*pi)*((b-y+y0)./((z-z0).^2+(b-y+y0).^2)-(b+y-
y0)./((z-z0).^2+(b+y-y0).^2)+(y-y0)./((b+z-z0).^2+(y-y0).^2)+(y-
y0)./((b-z+z0).^2+(z-z0).^2))';
end
```

(continued…)

```
function B=UField(x,y,z,a,I,Bias,mu)
%Return field of a side guide at point (y,z) with current I and bias
field Bias,
%located at (0,0,0)
    Bx=repmat(Bias(1),1,length(y));
    By=repmat(Bias(2),1,length(y));
    Bz=repmat(Bias(3),1,length(y));
    B=zeros(length(y),3);
    a=repmat(a,1,length(y));

B(:,1)=(Bx+(I*mu/(4*pi)).*(z./((a+x).^2+z.^2+y.*(y+sqrt((a+x).^2+y.^2+z.
^2)))-z./((a-x).^2+z.^2+y.*(y+sqrt((a-x).^2+y.^2+z.^2)))))';
    B(:,2)=(By-(I*mu/(4*pi)).*(z.*((a-x)./sqrt((a-
x).^2+y.^2+z.^2)+(a+x)./sqrt((a+x).^2+y.^2+z.^2))./(y.^2+z.^2)))';
    B(:,3)=(Bz+(I*mu/(4*pi))*(y.*((a-x)./sqrt((a-
x).^2+y.^2+z.^2)+(a+x)./sqrt((a+x).^2+y.^2+z.^2))./(y.^2+z.^2)-(a-
x)./((a-x).^2+z.^2+y.*(y+sqrt((a-x).^2+y.^2+z.^2)))-
(a+x)./((a+x).^2+z.^2+y.*(y+sqrt((a+x).^2+y.^2+z.^2)))))';
end

function theta360=TH(theta180)
%Convert angle from a range of -pi:pi (given by atan2)  to a range of 0-
2pi
    theta360=theta180+(1-sign(theta180)).*pi;
end
function theta=Deviation(theta1,theta2)
%compute deviation between angles theta1 and theta2 (when both are from
%0-2pi)
    theta=acos(cos(theta1-theta2));
end
```

References

1. Raab, E.L., et al., *Trapping of Neutral Sodium Atoms with Radiation Pressure.* Physical Review Letters, 1987. **59**(23): p. 2631-2634.
2. Anderson, M.H., et al., *Observation of Bose-Einstein Condensation in a Dilute Atomic Vapor.* Science, 1995. **269**: p. 198-201.
3. Davis, K.B., M.-O. Mewes, and W. Ketterle, *An Analytical Model for Evaporative Cooling of Atoms.* Applied Physics B, 1995. **60**: p. 155-159.
4. Folman, R. and J. Schmiedmayer, *Bose–Einstein condensates: Mastering the language of atoms* Nature, 2001. **413**(6855): p. 466-467.
5. Becker, C., *Eine neuartige magneto-optische Falle für Atomchip-Experimente*, in *Institute of Physics*. 2002, University of Heidelberg.
6. Krüger, P., *Coherent Matter Waves Near Surfaces*, in *Combined Faculty for the Natural Sciences and for Mathematics*. 2004, Ruperto-Carola University: Heidelberg.
7. Hofferberth, S., *Experiments with ultracold atoms and Bose-Einstein condensates in microtraps near surfaces*, in *Faculty of Physics and Astronomy*. 2004, University of Heidelberg.
8. Wildermuth, S., et al., *Optimized Magneto-Optical Trap for Experiments With Ultracold Atoms Near Surfaces.* Physical Review A, 2004. **69**: p. 030901.
9. Kasper, A., et al., *A Bose-Einstein Condensate in a Microtrap.* Journal of Optics B: Quantum and Semiclassical Optics, 2003. **5**(2): p. S143.
10. Schneider, S., et al., *Bose-Einstein Condensation in a simple microtrap.* Physical Review A, 2003. **67**: p. 023612.
11. Metcalf, H.J. and P. van der Straten, *Laser Cooling and Trapping of Atoms.* Journal of the Optical Society of America B, 2003. **20**(5): p. 887-908.
12. Folman, R., et al., *Microscopic Atom Optics: From Wires to an Atom Chip.* Advances in Atomic, Molecular, and Optical Physics, 2002. **48**: p. 263-356.
13. Bergeman, T.H., et al., *Quantized Motion of Atoms in a Quadrupole Magnetostatic Trap.* Journal of the Optical Society of America B, 1989. **6**(11): p. 2249-2256.
14. Haupt, S., *Setup of a new Experiment with ultracold ^{87}Rb Atoms: Towards Quantum Information Processing on an Atom Chip*. 2003, University of Heidelberg.
15. Kopfermann, H., *Nuclear Moments*: Academic Press Inc. 1958, New York.
16. Wing, W.H., *On Neutral Particle Trapping in Quasistatic Electromagnetic Fields.* Progress in Quantum Electronics, 1984. **8**: p. 181-199.
17. Ashkin, A. and J.P. Gordon, *Stability of Radiation-Pressure Traps: An Optical Earnshaw Theorem.* Optics Letters, 1983. **8**(10): p. 511-513.
18. Denschlag, J., D. Cassettari, and J. Schmiedmayer, *Guiding Neutral Atoms with a Wire.* Physical Review Letters, 1999. **82**(10): p. 2014-2017.
19. Bergeman, T.H., G. Erez, and H.J. Metcalf, *Magnetostatic Trapping Fields for Neutral Atoms.* Physical Review A, 1987. **35**(4): p. 1535-1546.
20. Petrich, W., et al., *Stable, Tightly Confining Magnetic Trap for Evaporative Cooling of Neutral Atoms.* Physical Review Letters, 1995. **74**(17): p. 3352-3355.
21. Ketterle, W. and N.J. van Druten, *Evaporative Cooling of Trapped Atoms.* Advances in Atomic, Molecular and Optical Physics, 1996. **37**: p. 181.
22. Minogin, V.G., J.A. Richmond, and G.I. Opat, *Time-orbiting-potential quadrupole magnetic trap for cold atoms.* Physical Review A, 1998. **58**(4): p. 3138-3145.
23. Davis, K.B., et al., *Bose-Einstein Condensation in a Gas of Sodium Atoms.* Physical Review Letters, 1995. **75**(22): p. 3969-3973.
24. Naik, D.S. and C. Raman, *Optically Plugged Quadrupole Trap for Bose-Einstein Condensates.* Physical Review A, 2005. **71**: p. 033617.
25. Pritchard, D.E., *Cooling Neutral Atoms in a Magnetic Trap for Precision Spectroscopy.* Physical Review Letters, 1983. **51**(15): p. 1336-1339.

26. Gott, Y.V., M.S. Ioffe, and V.G. Telkovsky, *Some new results on confining of plasmas in a magnetic trap.* Nuclear Fusion Proceedings of the Conference on Plasma Physics and Controlled Nuclear Fusion 1961 (IAEA), 1962: p. 1045.
27. Haase, A., et al., *Trapping Neutral Atoms with a Wire.* Physical Review A, 2003. **64**(4): p. 043405.
28. Brugger, K., et al., *Two-wire guides and traps with vertical bias fields on atom chips.* Physical Review A, 2005. **72**: p. 023607.
29. Reichel, J., *Microchip Traps and Bose-Einstein Condensation.* Applied Physics B, 2002. **74**(6): p. 469-487.
30. Wildermuth, S., *One-dimensional Bose-Einstein condensates in micro-traps*, in *Faculty of Natural Sciences and Mathematics*. 2005, Ruperto-Carola University: Heidelberg.
31. Dekker, N.H., et al., *Guiding Neutral Atoms on a Chip.* Physical Review Letters, 2000. **84**(6): p. 1124-1127.
32. Luo, X., et al., *Atom fiber for omnidirectional guiding of cold neutral atoms.* Optics Letters, 2004. **29**(18): p. 2145-2147.
33. Sackett, C.A., *Limits on Weak Magnetic Confinement of Neutral Atoms.* Physical Review A, 2006. **73**: p. 013626.
34. Brzozowski, T.M., et al., *Time-of-flight measurement of the temperature of cold atoms for short trap-probe beam distances.* Journal of Optics B: Quantum and Semiclassical Optics, 2002. **4**: p. 62-66.
35. Molenaar, P.A., et al., *Diagnostic technique for Zeeman-compensated atomic beam slowing: Technique and results.* Physical Review A, 1997. **55**(1): p. 605.
36. Lett, P.D., et al., *Observation of Atoms Laser Cooled Below the Doppler Limit.* Physical Review Letters, 1988. **61**(2): p. 169-172.
37. Metcalf, H.J. and P. van der Straten, *Laser Cooling and Trapping*: Springer. 1999.
38. Metcalf, H.J. and W.D. Phillips, *Laser Deceleration of an Atomic Beam.* Physical Review Letters, 1982. **48**(9): p. 596-599.
39. Joffe, M.A., et al., *Transverse cooling and deflection of an atomic beam inside a Zeeman slower.* Journal of the Optical Society of America B, 1993. **10**(12): p. 2257-2262.
40. Grimm, R., M. Weidemüller, and Y.B. Ovchinnikov, *Optical dipole traps for neutral atoms.* Advances in Atomic, Molecular, and Optical Physics, 2000. **42**: p. 95-170.
41. Anderson, D.Z., et al., *Atom Optics on a Chip*, in *MEMS 2003*. 2003: Kyoto, Japan.
42. Smith, H. and C.J. Pethick, *Bose-Einstein Condensation in Dilute Gases*: Cambridge University Press. 2002.
43. Cowan, J., *Doppler Cooling of Atoms and the Magneto-Optic Trap*, Davidson College.
44. Phillips, W.D., *Nobel Lecture: Laser cooling and trapping of neutral atoms.* Reviews of Modern Physics, 1998. **70**(3): p. 721-741.
45. Ketterle, W., et al., *High Densities of Cold Atoms in a Dark Spontaneous-Force Optical Trap.* Physical Review Letters, 1993. **70**(15): p. 2253-2256.
46. Wallace, C.D., et al., *Measurements of Temperature and Spring Constant in a Magnetic-Optical Trap.* Journal of the Optical Society of America B, 1994. **11**(5): p. 703-711.
47. Dalibard, J. and C. Cohen-Tannoudji, *Laser Cooling Below the Doppler Limit by Polarization Gradients: Simple Theoretical Models.* Journal of the Optical Society of America B, 1989. **6**(11): p. 2023-2046.
48. *Additional background material on the Nobel Prize in Physics 1997 (http://www.nobel.se/physics/laureates/1997/back.html)*
49. Reichel, J., W. Hänsel, and T.W. Hänsch, *Atomic Micromanipulation with Magnetic Surface Traps.* Physical Review Letters, 1999. **83**(17): p. 3398-3401.

50. Folman, R., et al., *Controlling Cold Atoms Using Nanofabricated Surfaces: Atom Chips.* Physical Review Letters, 2000. **84**(20): p. 4749-4752.
51. Brugger, K., et al., *Nanofabricated atom optics: atom chips.* Journal of Modern Optics, 2000. **47**(14/15): p. 2789-2809.
52. Lee, K.I., et al., *Single-Beam Atom Trap in a Pyramidal and Conical Hollow Mirror.* Optics Letters, 1996. **21**(15): p. 1177-1179.
53. Jones, M.P.A., *Bose-Einstein Condensation on an Atom Chip*. 2002, University of Sussex.
54. *The Weiss Family Laboratory for Nano-scale Systems (http://w3-new.bgu.ac.il/nanofabrication/)*
55. Groth, S., et al., *Atom Chips: Fabrication and Thermal Properties.* Applied Physics Letters, 2004. **85**(14): p. 2980-2982.
56. Grivich, M.I. and D.P. Jackson, *The Magnetic Field of Current-Carrying Polygons: An Application of Vector Field Rotations.* American Journal of Physics, 2000. **68**(5): p. 469-474.
57. Good, R.H., *Elliptic Integrals, The Forgotten Functions.* European Journal of Physics, 2001. **22**: p. 119-126.
58. Steck, D.A., *Rubidium 87 D Line Data*. 2003, Los Alamos National Laboratory.
59. Ashkin, A., *Acceleration and Trapping of Particles By Radiation Pressure.* Physical Review Letters, 1970. **24**(4): p. 156-159.
60. Vanhaecke, N., et al., *Accumulation of Cold Cesium Molecules via Photoassociation in a Mixed Atomics and Molecular Trap.* Physical Review Letters, 2002. **89**(6): p. 63001.
61. Lesanovsky, I., et al., *Adiabatic radio-frequency potentials for the coherent manipulation of matter waves.* Physical Review A, 2006. **73**: p. 033619.
62. Cornell, E.A. and C.E. Wieman, *The Bose-Einstein Condensate*, in *Scientific American*. 1998.
63. Ernst, U., et al., *Bose-Einstein Condensation in a Pure Ioffe-Pritchard Field Configuration.* Europhysics Letters, 1998. **41**(1): p. 1-6.
64. Ott, H., et al., *Bose-Einstein Condensation in a Surface Microtrap.* Physical Review Letters, 2001. **87**(23): p. 230401.
65. Bagnato, V., D.E. Pritchard, and D. Kleppner, *Bose-Einstein Condensation in an External Potential.* Physical Review A, 1987. **35**(10): p. 4354-4359.
66. Hänsel, W., et al., *Bose-Einstein Condensation on a Microelectronic Chip.* Nature, 2001. **413**(6855): p. 498-501.
67. Salomon, C., et al., *Channeling Atoms in a Standing Laser Wave.* Physical Review Letters, 1987. **59**(15): p. 1659-1662.
68. Jackson, J.D., *Classical Electrodynamics*: John Wiley & Sons. 3rd ed. 1998.
69. Gustafsson, E., *Design study of a Magneto-Optical Trap for laser cooling of rubidium atoms*. 2004, Lund University.
70. Petra, S.J.H., *Development of frequency stabilised laser diodes for building a Magneto-Optical Trap*. 1998, University of Amsterdam.
71. Zhang, W., Z. Xu, and L. You, *Effective Size of a Trapped Bose Gas.* Physical Review A, 2005. **72**: p. 053627.
72. Hess, H.F., *Evaporative Cooling of Magnetically Trapped and Compressed Spin-Polarized Hydrogen.* Physical Review B, 1986. **34**(5): p. 3476-3479.
73. Chu, S., et al., *Experimental Observation of Optically Trapped Atoms.* Physical Review Letters, 1986. **57**(3): p. 314-317.
74. Gibble, K.E., S. Kasapi, and S. Chu, *Improved Magneto-Optic Trapping in a Vapor Cell.* Optics Letters, 1992. **17**(7): p. 526-528.
75. Shin, Y., et al., *Interference of Bose-Einstein condensates split with an atom chip.* Physical Review A, 2005. **72**: p. 021604.

76. Maruyama, R., et al., *Investigation of sub-Doppler cooling in an ytterbium magneto-optical trap.* Physical Review A, 2003. **68**: p. 011403.
77. Luiten, O.J., M.W. Reynolds, and J.T.M. Walraven, *Kinetic Theory of the Evaporative Cooling of a Trapped Gas.* Physical Review A, 1996. **53**(1): p. 381-389.
78. Steane, A.M. and C.J. Foot, *Laser Cooling Below the Doppler Limit in a Magneto-Optical Trap.* Europhysics Letters, 1991. **14**(3): p. 231-236.
79. Demtröder, W., *Laser Spectroscopy*: Springer. 2nd ed. 1996.
80. Davis, C.C., *Lasers and Electro-Optics: Fundamentals and Engineering*: Cambridge University Press. 1996.
81. Pritchard, D.E., E.L. Raab, and V.S. Bagnato, *Light Traps Using Spontaneous Forces.* Physical Review Letters, 1986. **57**(3): p. 310-313.
82. Davidson, N., et al., *Long Atomic Coherence Times in an Optical Dipole Trap.* Physical Review Letters, 1995. **74**(8): p. 1311-1314.
83. Miranda, J.A., *Magnetic Field Calculations for Arbitrarily Shaped Planar Wires.* American Journal of Physics, 2000. **68**(3): p. 254-258.
84. Sy, W.N.-C., *Magnetic Field Due to Helical Currents on a Torus.* Journal of Physics A: Mathematical and General, 1981. **14**(8): p. 2095-2112.
85. Metcalf, H.J., *Magnetic Trapping of Decelerated Neutral Atoms.* Progress in Quantum Electronics, 1984. **8**: p. 169-175.
86. Sheehy, B., et al., *Magnetic-field-induced laser cooling below the Doppler limit.* Physical Review Letters, 1990. **64**(8): p. 858-861.
87. Feenstra, L., L.M. Andersson, and J. Schmiedmayer, *Microtraps and Atom Chips: Toolboxes for Cold Atom Physics.* General Relativity and Gravitation, 2004. **36**(10): p. 2317-2329.
88. Jackson, R.H., *Off-Axis Expansion Solution of Laplace's Equation: Application to Accurate and Rapid Calculation of Coil Magnetic Fields.* IEEE Transactions on Electron Devices, 1999. **46**(5): p. 1050-1062.
89. Townsend, C.G., et al., *Phase-Space Density in the Magneto-Optical Trap.* Physical Review A, 1995. **52**(2): p. 1423-1440.
90. Horak, P., et al., *Possibility of Single-Atom Detection on a Chip.* Physical Review A, 2003. **67**: p. 043806.
91. Sukumar, C.V. and D.M. Brink, *Spin-flip transitions in a magnetic trap.* Physical Review A, 1997. **56**(3): p. 2451.
92. Gerritsma, R. and R.J.C. Spreeuw, *Topological constraints on magnetostatic traps.* Physical Review A, 2006. **74**: p. 043405.
93. Krüger, P., et al., *Trapping and Manipulating Neutral Atoms with Electrostatic Fields.* Physical Review Letters, 2003. **91**(23): p. 233201.
94. Hinds, E.A., C. Vale, J,, and M.G. Boshier, *Two-Wire Waveguide and Interferometer for Cold Atoms.* Physical Review Letters, 2001. **86**(8): p. 1462-1465.
95. Monroe, C., et al., *Very Cold Trapped Atoms in a Vapor Cell.* Physical Review Letters, 1990. **65**(13): p. 1571-1574.
96. Tollett, J.J., et al., *Permanent Magnet Trap for Cold Atoms.* Physical Review A, 1995. **51**(1): p. R22-R25.
97. Sinclair, C.D.J., et al., *Bose-Einstein Condensation on a Permanent-Magnet Atom Chip.* Physical Review A, 2005. **72**: p. 031603(R).
98. Shevchenko, A., et al., *Trapping atoms on a transparent permanent-magnet atom chip.* Physical Review A, 2006. **73**: p. 051401.
99. *CRC Handbook of Chemistry and Physics*, ed. R.C. Weast: CRC Press. 57th ed. 1976.
100. Grabowski, A. and T. Pfau, *A lattice of magneto-optical and magnetic traps for cold atoms.* European Physical Journal D, 2003. **22**: p. 347-354.
101. Du, S., *Atom-chip Bose-Einstein condensation in a portable vacuum cell*. 2005, University of Colorado.

הדמיות מגנטיות ללכידה וקירור של אטומים ניטרליים

הוגש לפקולטה למדעי הטבע באוניברסיטת בן גוריון בנגב לשם קבלת תואר "מגיסטר" על ידי
אייל פלמינגר בשנת 2006

תקציר

האינטראקציות של אוסף של אטומים ניטרליים עם אור רזוננתי, שדות מגנטיים או שניהם יחדיו יכולים לשמש על מנת ללכוד את האוסף ולהביאם לטמפרטורות אולטרא-קרות, ומספר רב של ניסויים פותחו על מנת לעשות כן. אנו ביצענו מחקר תיאורטי של מספר צורות של מלכודות *ממוזערות*, ובכך מאפשרים ניסויים עם אטומים אולטרא-קרים על "שבב אטומי" בו השדות המגנטיים הלוכדים מיוצרים על ידי מיקר-מעגלים על שבב מוליך-למחצה. תזה זו מתארת את העקרונות הבסיסיים ומפרטת לגבי שיטות ספציפיות של לכידה מגנטית ומגנטו-אופטית, ומתארת שיטות לחישוב והדמייה של מלכודות כאלו. היא גם מתארת את הפיתוח וההרכבה של מלכודות מגנטיות ממוזערות שכרגע פועלות במעבדתנו. בנוסף, מתוארים מספר תכנונים למלכודות חדשות.

נושא החיבור___הדמיות מגנטיות ללכידה של אטומים ניטרליים_____
חיבור לשם קבלת התואר "מגיסטר"

בפקולטה_____למדעי הטבע_____

מאת___אייל פלמינגר_____

שם המנחה_____ד"ר רון פולמן_____

המחלקה_____לפיסיקה_____

הפקולטה_____למדעי הטבע_____

אוניברסיטת בן-גוריון בנגב

חתימת המחבר_____ תאריך_____

אישור המנחה_____ תאריך_____

אישור יו"ר ועדה מחלקתית_____ תאריך_____

אוניברסיטת בן-גוריון בנגב
הפקולטה למדעי הטבע

המחלקה ל **פיסיקה**

נושא החיבור **הדמיות מגנטיות ללכידה וקירור של אטומים ניטרליים.**

חיבור לשם קבלת תואר "מגיסטר" בפקולטה **למדעי הטבע**

מאת **אייל פלמינגר**

תאריך עברי	תאריך לועזי
ו' בטבת, תשס"ז	**27/12/2006**